

An Experimental Study on the Initial Shear Stiffness in Granular Material under Controlled Multi-Phase Laboratory Conditions

A Master Thesis

Submitted to

The Department of Civil Engineering

in

Bauhaus-University Weimar

in Partial Fulfillment of the Requirements
for the Degree of Master of Science

By

Milad Asslan

Master Program in Natural Hazards Mitigation in Structural Engineering
Weimar, Germany 2009

An Experimental Study on the Initial Shear Stiffness in Granular Material under Controlled Multi-Phase Laboratory Conditions

A Master Thesis By

Milad Asslan

Supervisors:

Prof. Dr.-Ing. habil. **Carsten Könke**
Institute of Structural Mechanics
Bauhaus Universität Weimar

Prof. Dr.-Ing. habil. **Karl Josef Witt**
Chair of geotechnical Engineering
Bauhaus Universität Weimar

Dr.-Ing. **Frank Wuttke**
Chair Soil Mechanics
Bauhaus Universität Weimar

Bauhaus-Universität Weimar
2009

Acknowledgment

This is publication no. GEOTECH-1304 of the R&D-Program GEOTECHNOLOGIEN funded by the German Ministry of Education and Research (BMBF) and German Research Foundation (DFG), Grant 03G0636B. Thanks due to them. Without their grant, this work was not possible.

I would like to acknowledge and extend my heartfelt gratitude to Dr. Frank Wuttke for his valuable suggestions, corrections and his continuous guidance for this work. I am sincerely grateful for his help. I would like also to thank Prof. Witt and Prof. Könke for accepting me as a student and for supervising me in this thesis, I deeply appreciate their time.

To my family, to the memory of my uncle.

Table of Content

1. INTRODUCTION	10
1.1 Motivation.....	11
1.2 Structure of the work.....	11
1.3 Literature review on experimental techniques	12
1.3.1 Technical properties	12
1.3.2 Effective length of samples	13
1.3.3 Near-field evidences.....	14
1.3.4 Different first arrivals.....	17
1.3.5 Comparison between bender elements and resonant column results.....	18
2. SMALL-STRAIN STIFFNESS	20
2.1 Introduction.....	21
2.2 Importance in Geotechnics.....	21
2.3 Determination of G_{\max}	26
2.3.1 In-Situ Tests	26
2.3.2 Laboratory tests.....	36
2.4 Interpretation methods in the bender elements test	36
2.4.1 First deflection method	36
2.4.2 Characteristic peaks	36
2.4.3 Cross-correlation method	37
2.4.4 Auto-correlation method	39
2.5 Summary	40
3. EQUIPMENT	42
4. MATERIAL PROPERTIES AND TESTING PROGRAM.....	47
4.1 Material properties	48
4.2 Testing program and procedure	49
5. EXPERIMENTAL CONSIDERATIONS	51
5.1 Introduction.....	52
5.2 Cell Calibration	52
5.3 Grounding	55
5.4 Out-of-plane directivity.....	56
5.5 waiting time	58
5.6 Waveforms	59
5.7 Frequency.....	60
5.7.1 Effects on Fluctuation	63
5.8 Summary	67
6. STUDY OF NATURAL MATERIAL	68
6.1 Introduction.....	69
6.2 Methodology.....	69
6.3 Influence of confining pressure.....	71
6.4 Influence of uniformity coefficient	77

6.5 Influence of relative density and void ratio.....	78
6.6 Comparing with predicted G_{\max} and resonant column.....	82
6.7 Summary.....	85
7. STUDY OF ARTIFICIAL MATERIAL.	86
7.1 Introduction.....	87
7.2 Experimental data.....	87
7.3 Summary.....	92
8. CONCLUSIONS AND RECOMMENDATIONS.....	93
REFERENCES	95

List of Figures

Figure 1. Effects of cantilever length (TC-29 Report, 2007).	12
Figure 2. Travel time vs. sample length (Viggiani and Atkinson, 1995).	13
Figure 3. R_d is ratio between distance traveled and wavelength; u is particle displacement, and F is amplitude of loading force (Sanches-Salinero et al., 1986).	14
Figure 4. Test data with different R_d (Jovičić et al., 1996).	15
Figure 5. Waveforms with different frequencies (Brignoli et al., 1996).	16
Figure 6. Differences in arrivals, $f = 2.5, 5$, and 10 kHz (Brignoli et al., 1996).	16
Figure 7. Potential arrival points.	17
Figure 8. Shear wave velocity vs. pressure at different arrival points from Figure 7.	17
Figure 9. Comparison between G_{max} results by bender elements and resonant column tests (Dyvik & Madshus, 1985).	18
Figure 10. G_{max} versus effective confining pressure obtained from bender elements, resonant column and torsional shear tests for dry Silica sand (Youn et al., 2008).	19
Figure 11. Stress-strain hysteresis loops $G_2 < G_1$ for $\varepsilon_2 > \varepsilon_1$ (Seed & Idris, 1970)	21
Figure 12. An idealization of the variation of stiffness with strain for soil (Atkinson & Salfors, 1991)	22
Figure 13. Characteristic stiffness-strain behavior of soil with typical strain ranges for laboratory tests and structures (Atkinson and Salfors, 1991) and (Mair, 1993)	22
Figure 14. Buildup of Residual Pore-Water Pressure in Different Sands in Cyclic	23
Figure 15. Inconsistent stress-strain behavior among laboratory and in-situ tests (Tatsuoka et al., 2000).	25
Figure 16. Inconsistent stress-strain behavior between TC with external axial strain measurement on a high-quality sample and field test (Tatsuoka et al., 2000).	25
Figure 17. Wave paths in the seismic reflection test (Karl, 2005).	26
Figure 18. Wave paths in the seismic refraction test (Wuttke, 2005).	27
Figure 19. Typical configuration of source and receivers in a SASW test (Wuttke, 2005).	29
Figure 20. Seismic cross-hole test (Wuttke, 2005).	30
Figure 21. Seismic down-hole test (Krumb & Wuttke, 2009).	31
Figure 22. A modified truck for SCPT test. Left: the penetrometer (Krumb & Wuttke, 2009).	32
Figure 23. Axial and radial deformation transducers.	33
Figure 24. Bender elements installed in top cap and pedestal of a triaxial cell.	35
Figure 25. Characteristic points for interpretation methods.	36
Figure 26. Two arrivals in output signal (Lee & Santamarina, 2005).	37
Figure 27 (Santamarina & Fratta, 2005).	38
Figure 28. a) Typical input and output signal in a bender elements test; b) cross-correlation of the input and output signals; c) detecting travel time by determining the maximum absolute value	39
Figure 29. a) Typical input and output signal in a bender elements test; b) auto-correlation of the input and output signals	40
Figure 30. Auto-correlation in a bender elements test	40
Figure 31. Laboratory system for bender elements test. 1: PC with LabVIEW program; 2: data logger; 3: amplifier; 4: manual air pressure valve; 5: twin-burette volume change indicator; 6: triaxial cell; 7: bender elements; and 8: burette.	44
Figure 32. Laboratory system for bender elements test.	45
Figure 33. Left top: bender element installed in the triaxial cell; left bottom: the base and the cap of the triaxial cell; right: the triaxial cell with a sample built inside.	45
Figure 34. Data logger.	46
Figure 35. Signal amplifier.	46
Figure 36. Grain size distribution for all natural materials.	48
Figure 37. LabView program as used in this study.	50
Figure 38. Calibration of triaxial cell with a steel dummy	53
Figure 39. A steel dummy used to calibrate the triaxial cell.	53

Figure 40. Immediate and creep volume change of the triaxial cell versus time.....	54
Figure 41. Immediate, creep and total volume change of the triaxial cell versus isotropic pressure ...	54
Figure 42. Immediate cell volume change versus pressure for loading and unloading	55
Figure 43. Input and output signal with and without grounding.....	55
Figure 44. Top and base of the triaxial cell. The top piece is rotated by angle θ	56
Figure 45. Input and output signals for different rotation angle θ	57
Figure 46. Amplitude of 1 st and 2 nd peak from Figure 45 versus θ . Amplitudes are normalized to amplitude at 0° of each peak	57
Figure 47. Input and output signals for different waiting times.....	58
Figure 48. Normalized velocity and volume change with time	59
Figure 49. Different waveforms as input signals with their output signals.	60
Figure 50. Different output signals for input signals with frequencies 1 to 15 kHz. Travel time is illustrated here with different interpretation methods	62
Figure 51. Shear wave velocity determined by different interpretation methods versus frequency	63
Figure 52. Normalized shear wave velocity versus frequency for saturated and dry samples. Velocity is normalized to velocity at frequency 1 kHz	64
Figure 53. Normalized shear wave velocity versus frequency at different isotropic pressure. Velocity is normalized to velocity at frequency 1 kHz	65
Figure 54. Normalized shear wave velocity determined by the first deflection method versus frequency for all natural samples. Velocity is normalized to velocity at frequency 1 kHz.....	66
Figure 55. Normalized shear wave velocity determined by the peak-to-peak method versus frequency for all natural samples. Velocity is normalized to velocity at frequency 1 kHz.....	66
Figure 56. Normalized shear wave velocity determined by the cross-correlation method versus frequency for all natural samples. Velocity is normalized to velocity at frequency 1 kHz.....	67
Figure 57. Determining travel time for saturated sample of sand #4 at 100 kPa. a) input signal for 11 kHz with its output; b) cross-correlation for input and output signal and determining the maximum value.	70
Figure 58. Increase of shear modulus G_{max} with confining pressure p for natural materials #1, #2 and #3.	72
Figure 59. Increase of shear modulus G_{max} with confining pressure p for natural materials #4, #5 and #6.	73
Figure 60. Increase of normalized shear modulus G_{max} with confining pressure p for all dry natural samples.....	75
Figure 61. Increase of normalized shear modulus G_{max} with confining pressure p for all saturated natural samples.	75
Figure 62. Void ratio change with confining pressure, p , for all tests. Void ratio is normalized to its initial value at 10 kPa for each test.....	76
Figure 63. Shear wave velocity gradient with confining pressure p	77
Figure 64. Dependence of n on C_u for all tests.....	78
Figure 65. Shear modulus G_{max} versus relative density D_r for each confining pressure step.....	79
Figure 66. Shear modulus G_{max} versus relative density D_r for each test (Same data of Figure 65 but categorized into tests instead of pressures).	80
Figure 67. Shear modulus G_{max} versus void ratio e at each confining pressure for all tests.....	81
Figure 68. Shear wave velocity gradient with void ratio e	81
Figure 69. Comparison between measured G_{max} by BE and predicted G_{max} with Hardin's equation..	83
Figure 70. Comparison between measured G_{max} by BE and predicted G_{max} with a D_r correlation....	83
Figure 71. Comparison between measured G_{max} by BE and predicted G_{max} with modified Hardin's equation.....	83
Figure 72. Comparison between measured G_{max} by BE and measured G_{max} by RC for materials #1, #3 and #4.....	83
Figure 73. Comparison between measured G_{max} by BE with cc method and predictions, RC data and BE with fd method.	84
Figure 74. Artificial material of uniform glass beads. Left 8 mm; and right 3.5 mm.....	87
Figure 75. Sample of glass beads in a triaxial cell.....	88
Figure 76. Shear small-strain modulus G_{max} variation with confining pressure in a logarithmic scale.	91
Figure 77. Shear wave velocity gradient with confining pressure. Each point represents velocity gradient for the previous pressure step.....	91

List of Tables

Table 1. Determination of shear wave velocity from bender element test using different analysis methods.....	18
Table 2. Properties of natural material.	48
Table 3. Physical properties of glass beads.....	49
Table 4. Amplitudes for different rotation angles.....	57
Table 5. State of the art for frequency and waveforms used in bender elements test.	61
Table 6. Sample of calculating shear wave velocity and G_{\max} for saturated sample of sand #4.	70
Table 7. Initial parameters for all tests on natural material.....	71
Table 8. Values of exponent n for all dry and saturated tests.....	76
Table 9. Experimental data for dry sample of glass beads of 8 mm.....	89
Table 10. Experimental data for saturated sample of glass beads of 8 mm.....	89
Table 11. Experimental data for dry sample of glass beads of 3.5 mm.....	89
Table 12. Experimental data for saturated sample of glass beads of 3.5 mm.....	89
Table 13. G_{\max} as a function of p for two particle sizes in dry and saturated condition.	90

Chapter 1

Introduction

1.1 Motivation

The initial shear modulus G_{\max} of soil is an important parameter for a variety of geotechnical design applications. This modulus is typically associated with shear strain levels about $5 \cdot 10^{-3}\%$ and below. The critical role of soil stiffness at small-strains in the design and analysis of geotechnical infrastructure is now widely accepted.

G_{\max} is a key parameter in small-strain dynamic analyses such as those to predict soil behavior or soil-structure interaction during earthquake, explosions, machine or traffic vibration where it is necessary to know how the shear modulus degrades from its small-strain value as the level of shear strain increases. G_{\max} can be equally important for small-strain cyclic situations such as those caused by wind or wave loading and for small-strain static situations as well. G_{\max} may also be used as an indirect indication of various soil parameters, as it, in many cases, correlates well to other soil properties such as density and sample disturbance. In recent years, a technique using bender elements was developed to investigate the small-strain shear modulus G_{\max} .

The objective of this thesis is to study the initial shear stiffness for various sands with different void ratios, densities, grain size distribution under dry and saturated conditions, then to compare empirical equations to predict G_{\max} and results from other testing devices with results of bender elements from this study.

1.2 Structure of the work

This study contains 8 chapters. In chapter 1, literature review of experimental techniques and determining the shear wave velocity is discussed. Chapter 2 presents theoretical background of G_{\max} and in-situ and laboratory methods to determine it, with emphasis on the bender elements test and explanations of interpretation methods. Equipment is explained in chapter 3, with details of the system built to make tests possible and effective by putting a set of hardware and software together to carry out the experiments. Two groups of material properties used in this study and test procedure are presented in chapter 4. In chapter 5, settings regarding collecting measurements and analyzing them are discussed. In this chapter, waveforms, frequency and interpretation method of signal are discussed in details, consequently, essential settings to use in tests and analyzing are settled. In chapter 6, test results of 6 natural materials are presented. Analyzing data and examining different influences are done. In chapter 7, tests on 2 artificial materials are investigated. Finally, final conclusions and recommendations for future work are given in chapter 8.

1.3 Literature review on experimental techniques

(Shirley and Hampton, 1978) first developed bender elements transducers to measure shear-waves in laboratory, using two ceramic piezoelectric elements fixed diametrically in a cylindrical aluminium pot. The dimensions of the bender elements were 1.27 cm in both thickness and width and 2.54 cm in length, this very large thickness allows only a very small displacement (5.6×10^{-7} m). In the next years, many improvements were added to bender elements. In the meanwhile, many technical problems arose. These technical points that are related to this study are discussed in the following sections.

1.3.1 Technical properties

In general, larger the penetration, the voltage signal is clearer but at the same time, it creates larger disturbance to the sample. On the other hand, smaller penetration is better in the sense that they do not cause much disturbance but generated energy may not be sufficient to propagate to the other end of sample or for receiving.

Figure 1 shows the effect of bender elements length on the G_{\max} vs. e relationship for isotropically consolidated specimens at 200 kPa. There is no clear influence of the bender elements length on the data results, thus, there is no need to increase this length since it causes further disturbance in the sample and reduces travel path between bender elements causing larger errors in estimating shear wave velocity (TC-29 Report, 2007).

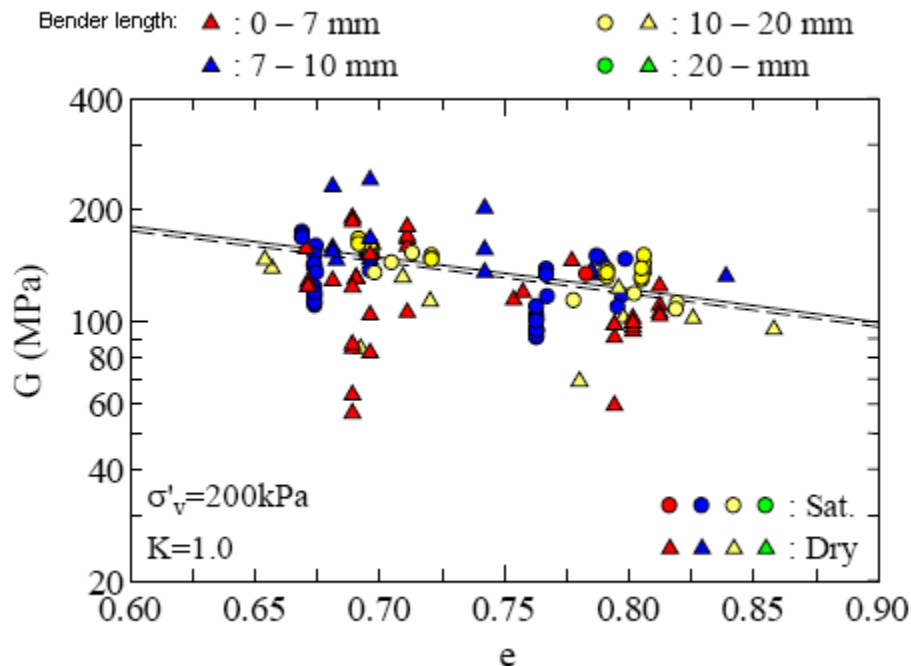


Figure 1. Effects of cantilever length (TC-29 Report, 2007).

(Schultheiss, 1981) recommended using bender elements with an empty cell to make sure that the shear wave is not transferred through the cell frame. He found that effective stress can change bender elements characteristics like resonant frequency.

In its international parallel test on the measurement of G_{\max} using bender elements by evaluating the bender element test results from 23 institutions from 11 countries, Technical committee, TC29 (Stress-strain and Strength Testing of Geomaterials) of International Society of Soil Mechanics and Geotechnical Engineering (ISSMGE) did not find any clear influence of the difference in bender size, its structure, cantilever length and wiring method was recognized (TC-29 Report, 2007).

1.3.2 Effective length of samples

Before starting to go into discussion of determining travel time one should determine the sample length as it is a main parameter to calculate velocity. (Viggiani and Atkinson, 1995) did a series of tests of different lengths and different pressures. Figure 2 show travel time against sample length. The three lines are straight and have intercepted of about 6 mm on the vertical axis that corresponds with the length of both bender elements (each is 3 mm). Therefore, effective distance should be defined as the distance between the tips of the elements, so-called tip-to-tip. This is in agreement with previous experimental work (e.g. Dyvik & Madhus, 1985).

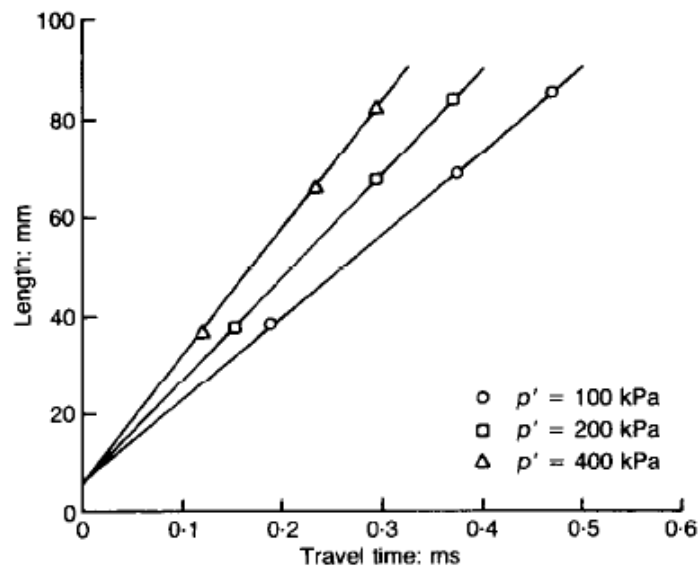


Figure 2. Travel time vs. sample length (Viggiani and Atkinson, 1995).

1.3.3 Near-field evidences

This near-field effect was theoretically analyzed by (Sanchez-Salinero et al., 1986). They showed in their theoretical study that the first deflection of signal may not correspond to the first arrival of the shear wave but to the near-field component. In the near-field, there is a strong coupling between P- and S-wave components. (Sanchez-Salinero et al., 1986) showed the presence of a highly attenuation wave component in the near-field which propagate at P-wave velocity yet with transverse particle motion. That means, the received signal may correspond to shear movement propagates at P-wave velocity, i.e. near-field effect may obscure the S-wave arrival and mask it. This effect becomes significant especially at closer distances between sources and receivers. They developed an analytical solution for the time record at a monitoring point that would result from excitation with a transverse sine pulse of a point source within an infinite isotropic elastic medium. The resulting wave was far from being a simple transversely polarized shear wave propagating in a longitudinal direction. They suggested a criterion, to avoid such an effect. The criterion is regulated by the ratio between the measurement distance, d , and the wavelength λ . Yet, this criterion is not easy to follow due to the dimensional limitations of the testing device

They showed in Figure 3 analytical solution of the motion expressed in term of R_d , which is ratio between distance traveled and wavelength. Comparison between two signals with two different wavelengths with indicates that signals with low R_d value tend to arrive earlier than the ones with higher values of R_d .

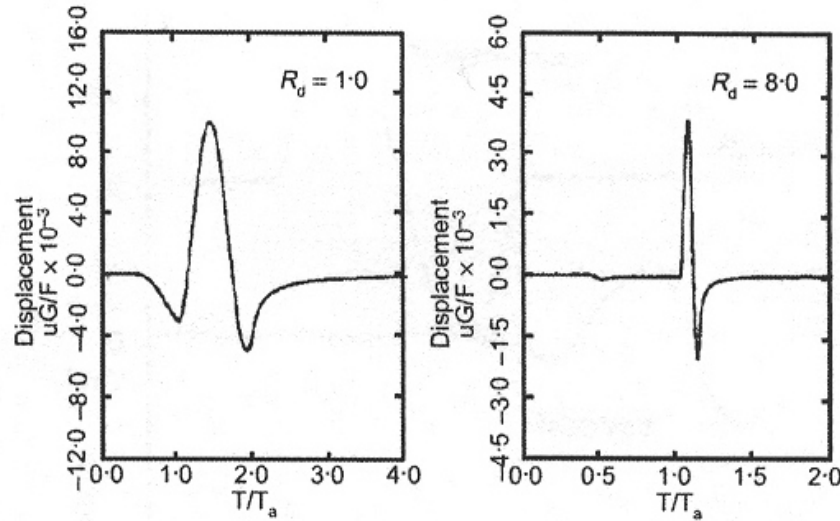


Figure 3. R_d is ratio between distance traveled and wavelength; u is particle displacement, and F is amplitude of loading force (Sanchez-Salinero et al., 1986).

(Jovičić et al., 1996) proved the effect of the near-field. Figure 4 shows two traces with different R_d values of 1.1 and 8.1, which correspond in this case to frequencies of 1.8 kHz and 15 kHz, respectively. The time scale was normalized with respect to the true arrival time of the shear wave T_a as determined by analytical solution. For low values of R_d there is an initial downward deflection of the trace before the shear wave arrives, representing the near-field effect. At high R_d , the near-field effect is almost absent. To avoid it they proposed using a distorted sinus wave as input or alternatively using resonant frequency of the bender elements as input signal. (Brignoli et al., 1996) gave further evidences on the near-field effect. Figure 5 shows some typical waveforms with different frequencies. The input signal is a one-period-sinus. To the right of each record, the input and output frequencies are given, and the ratio d/λ , where d is the effective length, and λ is the wavelength. This figure indicates that for low frequencies, the output signal tends to show previous arrival to that from higher frequencies. Another series of tests were done on dry silty clay supports their previous findings Figure 6. Three frequencies were used; 2.5, 5, and 10 kHz to show clear differences in arrivals.

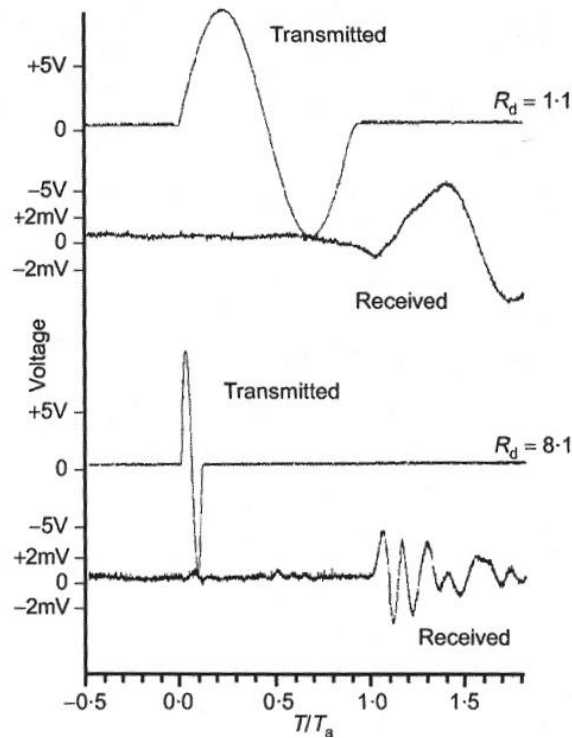


Figure 4. Test data with different R_d (Jovičić et al., 1996).

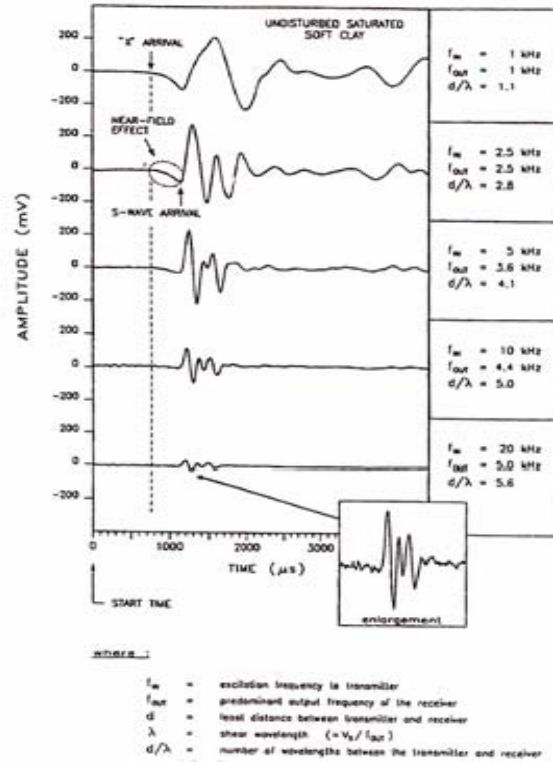


Figure 5. Waveforms with different frequencies (Brignoli et al., 1996).

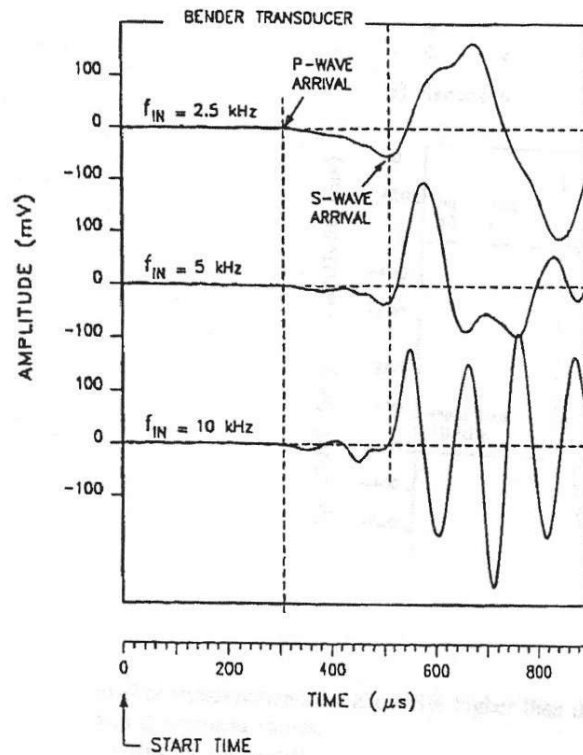


Figure 6. Differences in arrivals, $f = 2.5, 5$, and 10 kHz (Brignoli et al., 1996).

1.3.4 Different first arrivals

(Viggiani and Atkinson, 1995) compared different first arrival of the received signal at different potential points illustrated in Figure 7. Point A is the first deflection; point B in the first inflection; point C is the first zero after inflection; and point D is the second inflection. In their test using sample dimensions 38 mm in diameter and 76 mm in length in a triaxial cell, the travel time measured at point D was twice as the one measured at point A. This gives difference in calculated shear stiffness between these two points as high as 4 times. As a conclusion, they recommended using frequency methods to determine the shear wave velocity. Table 1 shows their results on shear wave velocity from bender element test using different analysis methods at different arrival points that are illustrated in Figure 7. Figure 8 shows results of shear wave velocities at the previous different arrival points.

(Jovićić et al., 1996) proved the effect of the near-field experimentally and proposed using resonant frequency of the bender elements as input signal.

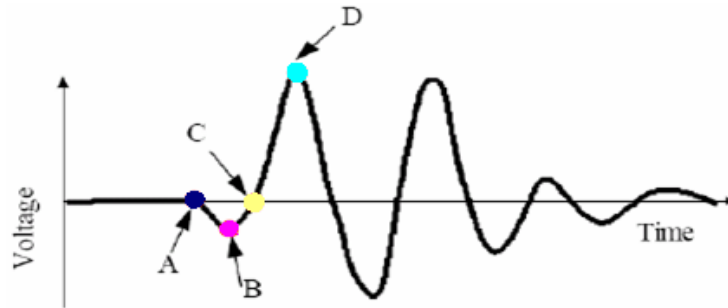


Figure 7. Potential arrival points.

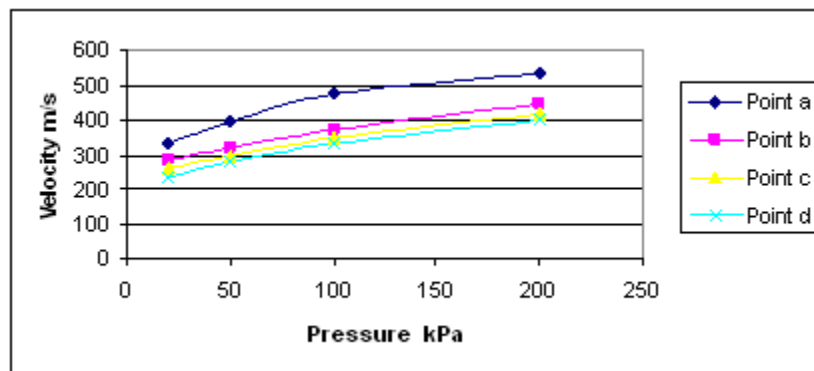


Figure 8. Shear wave velocity vs. pressure at different arrival points from Figure 7.

Table 1. Determination of shear wave velocity from bender element test using different analysis methods. Arrival points are illustrated in Figure 7. modified after (Viggiani and Atkinson, 1995).

Waveform	Analysis method	Arrival point	Travel time ms	Velocity m/s
Square wave	Selected points	A	0.280	250
		B	0.485	144
		D	0.564	124
Single sine wave	Peak to peak	A	0.493	142
		B	0.520	135
	Cross correlation	D	0.533	133
		0.524		134
	Cross-power spectrum	0.530		132

1.3.5 Comparison between bender elements and resonant column results

(Dyvik & Madshus, 1985) first installed bender elements in a resonant column device in order to measure in both tests simultaneously on five different clays. They found that G_{\max} results from 10 to 150 MPa by both techniques were in excellent agreement (Figure 9).

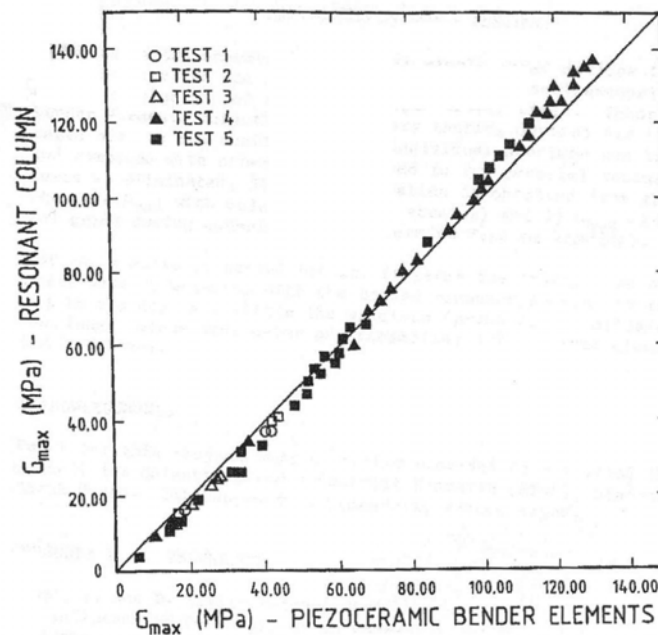


Figure 9. Comparison between G_{\max} results by bender elements and resonant column tests (Dyvik & Madshus, 1985).

(Brignoli et al., 1996) compared shear wave velocity for three soils using bender elements, shear plate and resonant column. By analyzing results in all three materials, they found that bender elements and resonant column compare well.

(Youn et al., 2008) compared shear wave velocity obtained from bender elements, resonant column, and torsional shear on two sands in dry and saturated condition at various relative densities and effective confining pressures. In dry condition, values of shear wave velocity from bender elements and resonant column are in good agreement. In saturated condition, values of shear wave velocity determined with bender elements are greater than those of resonant column. Figure 10 shows variations in G_{max} with effective confining pressure obtained from bender elements (peak-to-peak method), resonant column and torsional shear tests for dry Silica sand. The G_{max} values from these three methods at confining pressures of 50, 100, and 200 kPa show a maximum difference of about 3% relative to the mean value of each confining pressure stage.

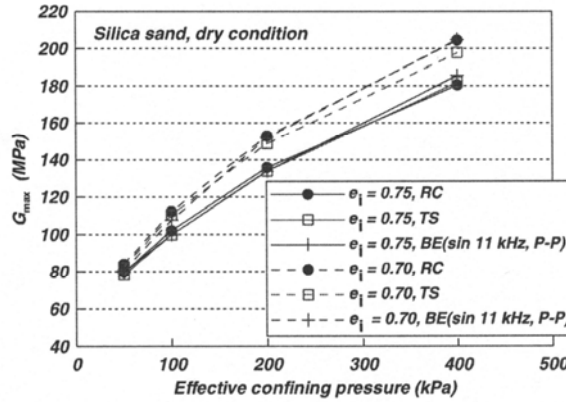


Figure 10. G_{max} versus effective confining pressure obtained from bender elements, resonant column and torsional shear tests for dry Silica sand (Youn et al., 2008).

First deflection method is typically used to detect shear wave velocity in BE test, which is very subjective and strongly dependent on input frequency used as described in details in chapter 5.

Chapter 2

Small-Strain Stiffness

2.1 Introduction

This chapter presents theoretical background of G_{max} and its importance in geotechnics besides in-situ and laboratory methods to determine it, with emphasis on the bender elements test and explanations of interpretation methods. Advantages and disadvantages of these methods are discussed.

2.2 Importance in Geotechnics

The shear modulus is usually expressed as the secant modulus by the extreme points on the hysteresis loop (Seed & Idriss, 1970) (Figure 11). The first loading curve, sometimes called the backbone curve, connects the load inversion points of oscillation periods with different levels of shear strain and has a hyperbolic shape. The slope in the origin point to this curve corresponds to the shear modulus G_{max} or G_0 . The stress-strain relationship in the very small-strain is considered a line; therefore, G_{max} is the shear modulus in the small-strain range, usually assumed at values below the linear elastic threshold strain of about $5 \times 10^{-3} \%$.

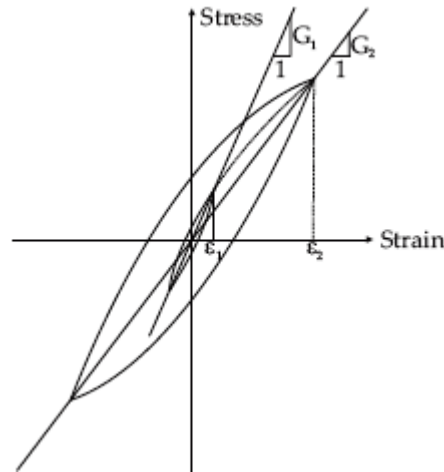


Figure 11. Stress-strain hysteresis loops $G_2 < G_1$ for $\epsilon_2 > \epsilon_1$ (Seed & Idriss, 1970)

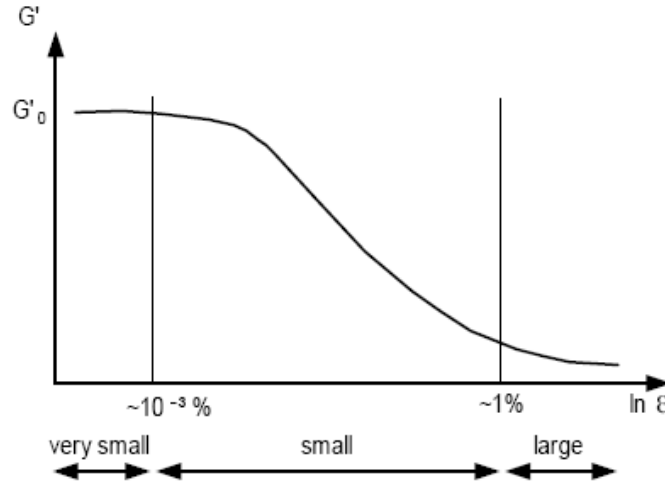


Figure 12. An idealization of the variation of stiffness with strain (Atkinson & Sallfors, 1991)

Figure 12 shows the reduction of stiffness with increment of strain (Atkinson, Sallfors, 1991). It is worthy to say, it is in general expected that G_{\max} does not change in the low-strain range.

Figure 13 illustrates typical strain ranges for structures and typical laboratory tests to measure different strains. Vibrations caused by seismic in situ tests, traffic, construction works, weak earthquakes or even blastings usually have shear strain amplitudes below $5 \cdot 10^{-3} \%$.

(Yamashita et al., 2001) analyzed results of tests from nineteen laboratories done on sand, clay and soft rock. Monotonic tests (triaxial and torsional) and cyclic tests (triaxial, torsional and resonant column) were performed in this international parallel program. They found that stiffness at strains between 10^{-5} and 10^{-3} was similar between monotonic and cyclic tests.

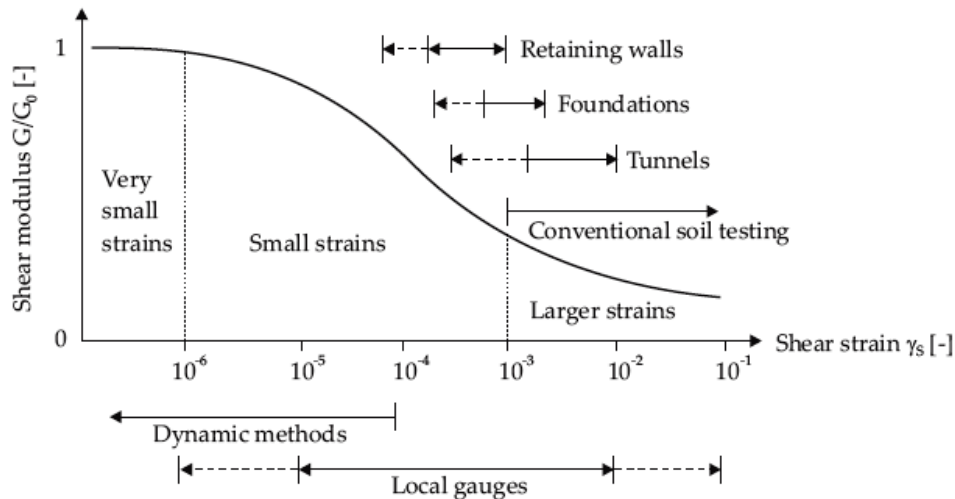


Figure 13. Characteristic stiffness-strain behavior of soil with typical strain ranges for laboratory tests and structures (Atkinson and Sallfors, 1991) and (Mair, 1993)

There are two types of cyclic threshold shear strain, they are the linear cyclic threshold shear strain, γ_{tl} , and the volumetric cyclic threshold shear strain, γ_{tv} , with $\gamma_{tv} > \gamma_{tl}$. These strains represent boundaries between fundamentally different categories of cyclic soil behavior. For cyclic strains below γ_{tl} , soil behaves essentially as a linearly elastic material. Between γ_{tl} and γ_{tv} , soil becomes markedly nonlinear but remains largely elastic because permanent changes of its microstructure still do not occur or are negligible. Above γ_{tv} , soil becomes increasingly nonlinear and inelastic, with significant permanent microstructural changes taking place under cyclic loading. That is, γ_{tv} = the threshold separating cyclic strains that cause or do not cause significant permanent changes of soil microstructure. (Vucetic, 1994) identified these two thresholds for different types of soils. He showed how the value of the threshold shear strain depends on soil type. Figure 13 shows that for many different sands γ_{tv} is essentially $10^{-2}\%$, regardless of confining stress, density, and specimen fabric. Cyclic triaxial strain-controlled test results obtained for a gravel by (Hynes- Griffin, 1988) showed that γ_{tv} in gravels is affected by initial effective mean normal stress, $\bar{\sigma}_0$ and OCR in the same way, i.e., it increases somewhat with $\bar{\sigma}_0$ and OCR. However, γ_{tv} values obtained by (Hynes-Griffin, 1988) for gravel are generally smaller than for sands, ranging between $0.5 \cdot 10^{-2}\%$ and $2 \cdot 10^{-2}\%$.

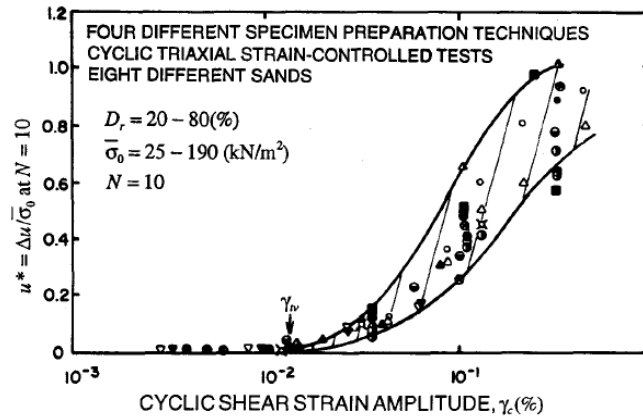


Figure 14. Buildup of Residual Pore-Water Pressure in Different Sands in Cyclic Triaxial Strain-Controlled Tests (Vucetic, 1994).

Based on different researches and on his study, (Vucetic, 1994) concluded that for every soil a cyclic shear strain amplitude can be found below which: (1) There is essentially no permanent microstructural change; (2) residual cyclic pore-water pressure essentially does not develop if the soil is fully saturated and cyclically sheared in undrained conditions; and (3) the permanent volume change is negligible if the soils is dry, partially saturated, or fully saturated with drainage allowed. If during cyclic shearing this threshold cyclic shear strain is exceeded: (1) The microstructure is altered irreversibly; (2) the soil stiffness changes permanently; (3) in fully saturated soils loaded in undrained conditions a permanent cyclic pore-water pressure develops; and (4) in dry, partially saturated, or fully saturated soils with drainage allowed, a permanent volume change accumulates.

(Santos & Gomes Correia, 2001) investigated the shear modulus degradation based on a key parameter defined by them and called reference threshold shear stain, $\gamma_{0.7}$. This parameter is defined as the shear strain for a stiffness degradation factor of $G/G_{\max}=0.7$, in which G_{\max} is the very small-strain shear modulus and G is the secant shear modulus. Their approach was the following: to characterize the non-linear secant stiffness of soils, two parameters are needed: G_{\max} that defines the rigidity of soil at very small strain; and the reference threshold shear stain, $\gamma_{0.7}$ that characterizes the degree of non-linearity at medium-strain levels.

(Burland, 1989) described soil behavior at very small strain region. He found that soil exhibits high stiffness at small-strain and non-linear stress-strain response. By studying constructions of practical project, he showed the significant effect of small-strain behavior on soil-structure interaction, stress distribution in soil mass and displacement profiles around loaded areas and excavation. He also compared laboratory test using LVDTs with in-situ tests at small-strain levels. He found that, if the strains are measured locally to a high accuracy, tests on high-quality samples at the appropriate confining pressure give remarkably accurate and consistent measurements of the in-situ small-strain stiffness.

(Clayton & Heymann, 2001) the behavior at very small strains of three widely different natural materials: Bothkennar clay, Londonclay, and a high-porosity Chalk. They used LVDTs to measure small-strain in laboratory. They found that Stiffness measured in the triaxial apparatus at very small strain levels were similar to stiffness obtained using field geophysical techniques. They also found that at very small-strain levels the observed stress-strain behavior appeared to be linear for all three materials.

(Tatsuoka et al., 2000) achieved a development of a more unified view for static and dynamic behavior and laboratory and field testing. Figure 15 illustrates a typical example of inconsistency in stress-strain relationship between field tests (PLT: plate load test, PMT: pressuremeter test) and a conventional triaxial compression test (TC). Such low stiffness values obtained from conventional laboratory stress-strain tests were often considered due to serious effects of sample disturbance. Although this effect is still important, it may not be the exclusive cause. It is common to obtain different stiffness values among conventional laboratory stress-strain tests and among conventional in-situ tests also. Therefore, the link between laboratory stress-strain tests and in-situ tests is missing, in particular among practicing engineers. It is also considered that elastic stiffness from in-situ wave velocity is irrelevant when predicting ground deformation and structural displacements at static loads. It was common to obtain elastic deformation property by performing dynamic tests such as resonant column and wave propagation tests. Later (Shibuya et al., 1992) and (Tatsuoka et al., 1995), among others, showed that the strain rate dependency of the stiffness at small-strain in cyclic torsional shear was very low. (Woods, 1991) and (Tatsouka & Shibuya, 1991) pointed out that it is not necessary to distinguish between dynamically and statically measured elastic stiffness values, when measured under the same conditions. From analyzing significant amount of data, (Tatsuoka et al., 2000) found the same conclusion.

Figure 16 illustrates stress-strain relationship in triaxial compression test measured with external axial gauge and field full-scale test on a high-quality sample. It shows that the stiffness in the field is significantly underestimated.

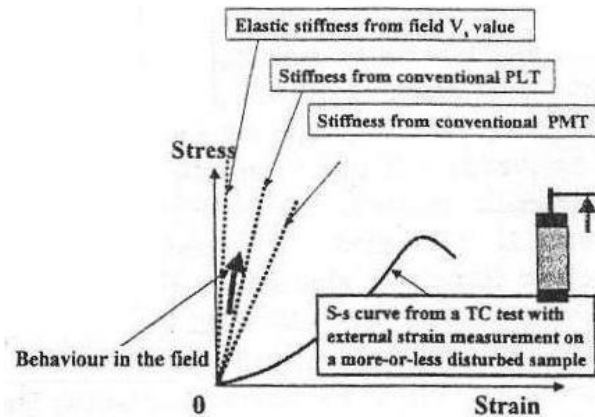


Figure 15. Inconsistent stress-strain behavior among laboratory and in-situ tests (Tatsuoka et al., 2000).

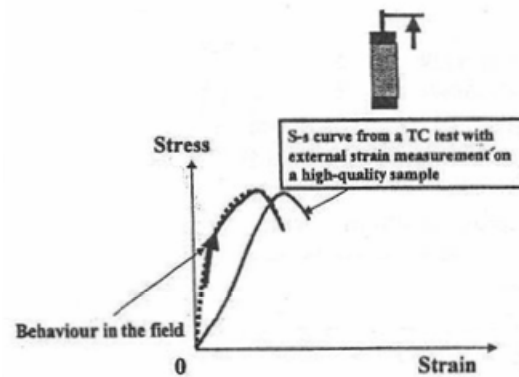


Figure 16. Inconsistent stress-strain behavior between TC with external axial strain measurement on a high-quality sample and field test (Tatsuoka et al., 2000).

2.3 Determination of G_{\max}

In the following sections, an overview of the most common in-situ and laboratory tests to determine the small-strain stiffness of soil is given. Each test is explained with giving the advantages and disadvantages. In low strain tests, deformations can be assumed as elastic.

2.3.1 In-Situ Tests

The objective of the in-situ tests is generally to determine the P-wave and/or S-wave velocity in the field. There are two categories of in-situ seismic tests depending on the strain range; small-strain tests and large-strain tests. The second category contains dilatometer test, pressuremeter test, cone penetration test (CPT) and standard penetration test (SPT) etc. These tests provide soil stiffness parameters in the large-strain range. Only the small-strain tests will be discussed in this chapter.

- *Seismic reflection tests*

The seismic reflection test determines the P- and S-wave velocity and superficial layers thickness using the principle of echo-sounding and radar. (ASTM D7128–05) is a code summarizes the technique, equipment, field procedures, data processing, and interpretation methods for the assessment of shallow subsurface conditions using the seismic-reflection test. The test is performed by producing an impulsive disturbance at the source S and measuring the arrival time at the receiver R as shown in Figure 17.

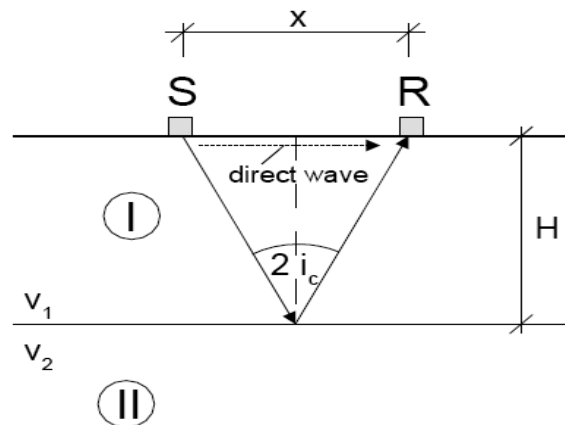


Figure 17. Wave paths in the seismic reflection test (Karl, 2005).

Some of the wave energy follows a direct path from S to R. Another portion of the impulse energy travels downward and strikes the layer boundary. A part of that wave which is reflected back toward the ground surface arrives at the receiver, so the direct wave and the reflected wave can overlap, therefore it is difficult to determine the arrival time of the reflected wave, particularly of cases in which reflected waves arrive while the receiver is still responding to direct waves. Therefore the difference between the two arrivals should be sufficient, thus, layer should be thick. Furthermore, Arrival times from waves reflected at several layer interfaces have to be distinguishable. Field methods for the acquisition of seismic reflection test vary considerably, depending on whether the area is land or marine, on the nature of the geologic problem, and on the accessibility of the area (Sheriff & Geldart, 1995).

- *Seismic refraction test*

The seismic refraction test involves the measurement of travel times of P- or S-waves from an impulse source to a linear array of receiver points along the ground surface at different distances from the source. The seismic refraction test avoids the reflection test problems by considering the first wave arrival to the receiver regardless of wave path. The setup of a seismic refraction test can be found in (ASTM D5777) and can be done as shown in Figure 18.

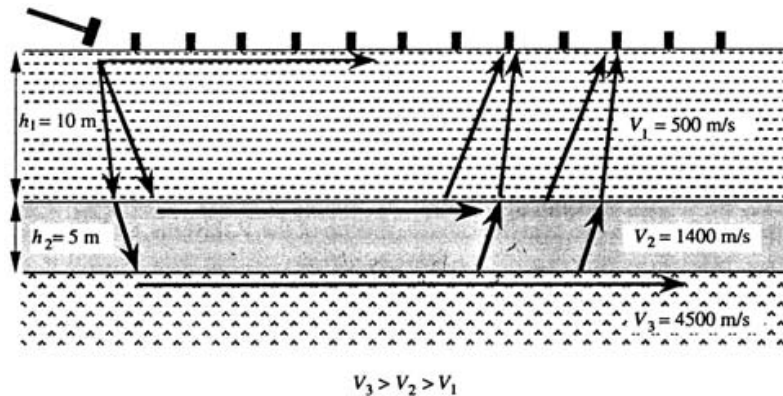


Figure 18. Wave paths in the seismic refraction test (Wuttke, 2005).

The source excitation can be mechanical or explosive. The receivers are usually geophones placed in a linear array. One receiver is located at the source. The output of all receivers is recorded when the impulse load is triggered. The method is also applicable for inclined layer interfaces and multi-layered stratifications, if the wave propagation velocity increases with the layer depth. If it is not the case, the results of seismic refraction test can be misleading. A low-velocity layer underlying a higher-velocity layer will not appear as an individual segment on the travel time-distance diagram. Instead, it will cause the computed depths of the layer boundaries to be greater than the actual

depths. Details of calculating wave velocities for horizontal layering and inclined or irregular layering can be found in (Kramer, 1996).

- *Spectral analysis of surface waves (SASW)*

The SASW-technique uses the characteristics of Rayleigh waves to obtain the stratification of a site. This method was developed by (Nazarian & Stokoe, 1983; Stokoe et al., 1994). Rayleigh waves travel, as surface waves, in the region close to the soil-air interface. Due to the fact that the penetration depth of the Rayleigh waves into the ground is approximately one wavelength, the thickness of the layer package influencing the speed of the wave changes with the wavelength. This leads to a wave velocity that depends on the wavelength respectively the frequency. Such behavior is also called dispersion.

The SASW test is performed by placing two vertical receivers on the ground surface in line with an impulsive or random noise source, as illustrated in Figure 19. The wave arrival in at least two points at some distance from the source is recorded. The output of both receivers is recorded and transformed to the frequency domain using the fast Fourier transform. After transformation, the phase difference, $\phi(f)$, can be calculated for each frequency. The corresponding travel time between receivers can be calculated for each frequency from:

$$\Delta t(f) = \frac{\phi(f)}{2\pi f}$$

Since the distance between receivers, $\Delta t = d_2 - d_1$, is known, the Rayleigh wave phase velocity and wavelength can be calculated as function of frequency:

$$v_R(f) = \frac{\Delta d}{\Delta t(f)}$$

$$\lambda_R(f) = \frac{v_R(f)}{f}$$

With modern electronic instrumentation, these calculations can be performed in the field virtually in real time. The unwrapped phase of this spectrum is used to calculate an experimental dispersion curve of the Rayleigh wave velocity.

The shear wave velocity and shear damping ratio profiles are determined separately. (Lai et al., 2002) presented a procedure to measure and invert surface wave dispersion and attenuation data simultaneously and, thus, account for the close coupling between the two quantities. The methodology also introduced consistency between phase velocity and attenuation measurements by using the same experimental configuration for both. Characteristic statistics, statistical distribution, and measurement uncertainty were

determined for each phase of SASW by (Marosi & Hiltunen, 2004). Using the empirical statistical properties and measurement uncertainty results as validation criteria, an analytically based uncertainty assessment system was developed

SASW test has important advantages over other field tests; they require no boreholes, can be performed quickly, and can detect low velocity layers. SASW testing is particularly useful at sites where drilling and sampling are difficult. On the other hand, this test requires specialized equipment and experienced operator.

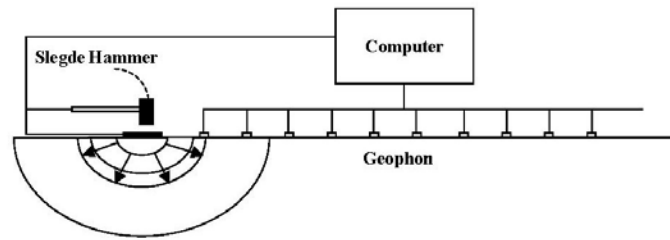


Figure 19. Typical configuration of source and receivers in a SASW test (Wuttke, 2005).

- *Seismic cross-hole test*

The seismic cross-hole test measures the P- and S-wave velocities between boreholes. The procedures are described in (ASTM D4428). The simplest configuration consists of two boreholes. The first one contains the source that can be mechanical or explosive. In the second one, the receiver is installed at the same depth as the source. By testing at various depths, a velocity profile can be obtained. To avoid inaccuracies resulting from trigger time measurements, casing and backfill effect, and site anisotropy, it is preferred to use more than two receivers as in Figure 20. Wave velocity can then be calculated from differences in arrival times. Arrival time can be determined by (first arrival, first peak, first through, etc.) or by cross-correlation technique. In first arrival, travel time is calculated between the start of input signal and the first deflection from zero line in the output signal. Travel time can also be calculated between the first peak in the input signal and the first peak in the output signal for first peak method and similar for first through method. For the cross-correlation technique, travel time is taken as the time shift that produces the peak cross-correlation between signals recorded. This technique is favorable because first deflection, first peak or first through can be difficult to determine, especially with the existence of noise. Typical distances between the boreholes are 5 to 12 m for layered soils and up to 30 m for nearly homogeneous sites. Cross-hole test can yield reliable velocity data to depths of 30-60 m using mechanical impulse sources, and to greater depths with explosive sources (Kramer, 1996).

Cross-hole tomography test is an extension of the conventional cross-hole seismic test. It uses a string of receivers instead of just one, so that multiple ray paths can be recorded

for a single source signal (Pihl et al., 1986). Amplitude attenuation measurements from cross-hole tests involving three or more boreholes was used to compute the material damping ratio of soils (EPRI, 1993).

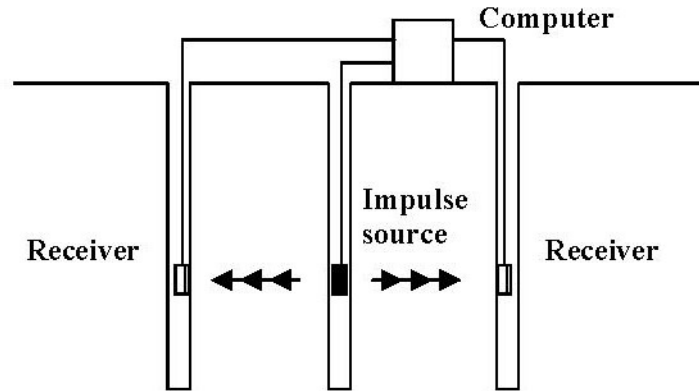


Figure 20. Seismic cross-hole test (Wuttke, 2005).

- *Seismic down-hole and up-hole test*

The down-hole or up-hole test is performed in one borehole. In the down-hole test (Figure 21), the receiver is in the borehole that can be moved to different depths to measure different layers. While the source is located on the surface near the borehole. In the up-hole test, it is vice versa, the source is situated in the borehole, and the receiver is on the surface. ASTM D7400 is the standard test methods for down-hole seismic testing.

Since waves can be more easily generated on the surface than in the borehole, the down-hole test is more practical in use; therefore, it is more commonly used.

The down-hole test detects layers that can be hidden in the seismic refraction surveys. It also requires only one borehole, which is less costly and complicated than seismic cross-hole test. On the other hand, drilling of the borehole, like other tests that need boreholes, can disturb the soils around it. In addition, uncertainties can result from background noise effect, groundwater table effects, etc.

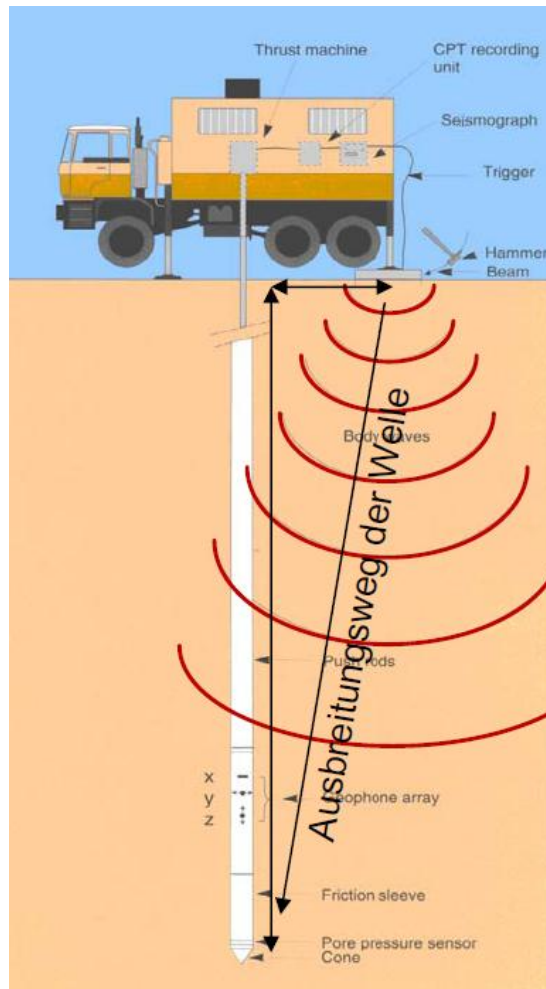


Figure 21. Seismic down-hole test (Krumb & Wuttke, 2009).

- *Seismic cone penetration test*

The seismic cone penetration test (SCPT) (Robertson et al., 1985) can be seen as a special version of a down-hole test with the receivers (geophones or accelerometers) installed in the tip of a cone pushed into the ground by conventional cone penetration equipment, while the source is placed at the surface (Figure 22). An SCPT system includes the following components: (1) an electrical penetrometer, (2) hydraulic pushing system with rods, (3) cable or transmission device, (4) depth recorder, (5) source, and (6) data acquisition unit. The seismic source consists of a steel beam and different types of hammers; a horizontal hammer blow at one end of the beam produces a shear wave dominated pulse and a vertical one blow on top of the beam produces a compression wave dominated pulse. The cone with the receiver is pushed stepwise into the ground. Usual intervals are 0.5 or 1.0 m. At each step the source generates a seismic pulse recorded by the cone receiver. The standard testing method to perform SCPT is ASTM D5778. A variety of cone penetrometer systems is available, ranging from small mini-

pushing units to very large truck and track vehicles. The penetrometers are normally available in two standard sizes: (1) a 35.7-mm diameter version having a corresponding cross-sectional area of 10 cm^2 ; and (2) a 44-mm diameter version. (Kurup, 2006) integrated several sensing techniques with the cone penetrometer technology. These include a camera for visual identification, and various sensors for measuring stresses, pore water pressure, shear wave velocity, electrical conductivity, temperature, oxidation-reduction potential, radioactivity, and hydrocarbon contamination in soils. Since no borehole is necessary, the test is much less expensive than a down-hole test.

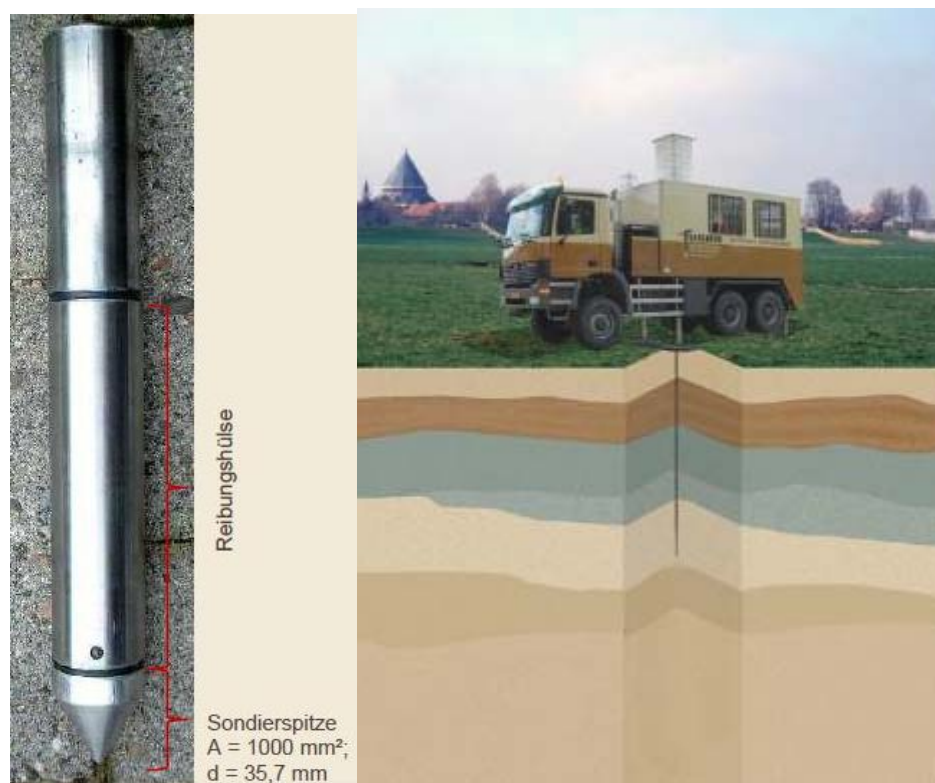


Figure 22. A modified truck for SCPT test. Left: the penetrometer (Krumb & Wuttke, 2009).

2.3.2 Laboratory Tests

A limited number of laboratory tests are performed in the range of small-strain. They include local deformation transducers, resonant column test, piezoelectric bender element test and ultrasonic test.

- *Local deformation transducers*

In triaxial testing device, displacement is usually measured between the top cap and the base pedestal, using a global transducer. The accuracy of such transducer is not enough to measure the small-strain. Furthermore, the sample may have no parallel and smooth ends; therefore, the top cap has probably no perfect full instant contact at the small-strain range. The restraints at the ends of the sample cause non-uniform displacements over the height. Local deformation transducers (LDTs) avoid such problems of imperfect bedding. They are installed typically in a triaxial cell. They can measure deformations axially or radially as shown in Figure 23. Local deformation can measure strain of 5×10^{-5} . Several transducers may be used simultaneously in order to observe the loss of homogeneity of the strain field in the specimen.



Figure 23. Axial and radial deformation transducers.

Local deformation transducers are convenient up to a specific strain limit, after which they could be destroyed. They can disturb the specimen (especially porous rock) due to the penetration of glue inside the pores. They measure displacements between two specific points to deduce strain in the specimen, assuming that deformations in the specimen are homogeneous.

- *Resonant column*

The resonant column test is a well-known technique to determine the dynamic shear modulus, dynamic elasticity modulus and damping ratio. First proposed in 1930s, and then further developed in 1970s, mainly applied for strain levels of 10^{-4} - $10^{-2}\%$. In a triaxial cell, a soil sample is installed and excited torsionally or axially at its top end. The excitation is most commonly harmonic, in a range between 30 and 300 Hz, but also random noise or pulses have been used. There are devices for cylindrical samples and for hollow-cylindrical samples available, the latter minimize the variation of shear strain amplitudes across the sample in the case of torsional excitation. With a built in accelerometer, the acceleration at the top of the sample can be measured.

The principle of a resonant column device is based on a cylinder, which is set into torsional or axially vibration. The excitation is most commonly harmonic in a range between 30 and 300 Hz. The frequency increases until resonance occurs. Under the assumption of a linear elastic material, the shear wave velocity is determined from the wavelength and the resonance frequency in the fundamental mode of vibration. The fundamental frequency is a function of the small-strain stiffness of the soil, the geometry of the specimen and certain characteristics of the resonant column apparatus. The specimen can be free at each end so that its lowest mode of vibration is with one node located at the center of the specimen. This type is called the free-free type. In which the specimen is excited at the bottom and the response is picked up at the top. In fixed-free type, both driver and pickup are located at the top end of the specimen.

- *Bender elements*

The bender element method is a simple technique to obtain the very small-strain elastic shear modulus of a soil G_{max} by measuring the velocity of propagation of a shear wave through a sample. The history of piezoelectricity dates back to 1880 when Pierre and Jacques Curie first discovered the piezoelectric effect in various substances including Rochelle salt and quartz. Piezoelectric materials can generate an electric charge with the application of pressure; conversely, they can change physical dimensions with the application of an electric field (called *converse piezoelectricity*). The word *Piezoelectricity* comes from Greek; *Piezo* means Pressure in Greek, so the term (*Piezoelectricity*) means (*electricity by pressure*).

In material that has piezoelectric properties, ions can be moved more easily along some crystal axes than others. Pressure in certain directions results in a displacement of ions such that opposite faces of the crystal assume opposite charges. When pressure is released, the ions return to original positions.

The first practical application for piezoelectric devices was sonar, first developed during World War I. The use of piezoelectricity in sonar created intense development interest in piezoelectric devices. Over the next few decades, new piezoelectric materials and new applications for those materials were explored and developed.

An advantage of this method is that the computation of G_{\max} is more direct and simple than other methods like the resonant column test or in-situ tests. Bender elements are easy to install into most soil testing apparatus (i.e., triaxial test, shear test, resonant column test and oedometer test) (Figure 24). The bender elements themselves are cheap, small and lightweight, furthermore they are non-destructive.



Figure 24. Bender elements installed in top cap and pedestal of a triaxial cell.

Regarding the disadvantages, this method is based on the idea of one-dimensional wave propagation, therefore a plane wave is assumed to propagate in the medium. In reality, the case is three-dimensional wave propagation from a not-perfect-point source causing the near-field effect. Furthermore, the specimen has its boundaries; therefore, there is reflection and interference of waves. Another hypothetical assumption is considering the material isotropic, uniform and continuum, which disregards travel path and dispersion. Sufficient contact should be between the bender elements and the surrounding soil in order to transmit the mechanical wave from the elements to the soil. If this was not the case, the received signal can be unclear and difficult to be analyzed, especially for soils with large particles. That is why it is better to have minimum penetration in the soil according to the particles diameter.

2.4 Interpretation methods in the bender elements test

Interpretation methods for results from bender elements test is presented here. Further discussion about reliability, uncertainty and limits is shown in chapter 5.

2.4.1 First deflection method

Considering the first deflection as the first arrival of the shear wave was very common in the beginning of the bender elements technique. This method of interpretation assumes plane wave fronts and the absence of any reflected or refracted waves. Travel time is calculated between the start of input signal (point A, Figure 25) and the first deflection from zero line (point C). This method completely ignores the near-field effect and P waves.

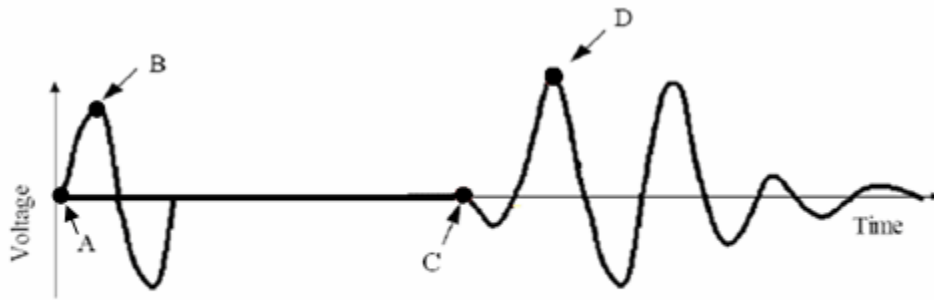


Figure 25. Characteristic points for interpretation methods.

2.4.2 Characteristic peaks

This method assumes the travel time as the time between two Characteristic points in input and output or both in output in the case of the existence of a second arrival. In the first case, the peak of the input signal (point B, Figure 25) and the first peak in the output signal (point D). If two arrivals are received, measuring the time travel between two peaks or two troughs is possible (Figure 26).

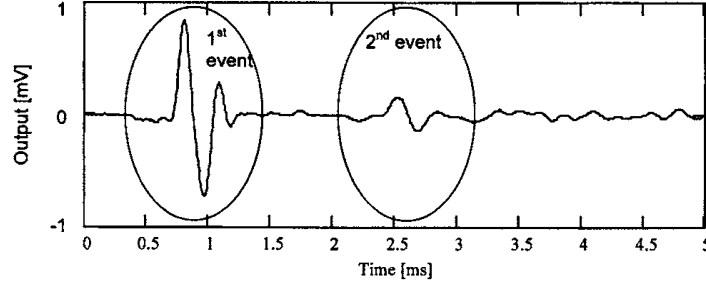


Figure 26. Two arrivals in output signal (Lee & Santamarina, 2005).

2.4.3 Cross-correlation method

Travel time is taken as the time shift that produces the peak cross-correlation between signals recorded, based on the assumption of plane wave fronts and the absence of any reflected or refracted waves. For an impulse, wave that was recorded at two spaced points will reach maximum value for the time shift that equals the travel time of the impulse between two points. It is convenient to calculate cross-correlation in the frequency domain using the Fast Fourier Transform (FFT). Cross-correlation identifies similarity between two signals even if the signal-to-noise ratio is low.

If we have two signals x and z , to run the cross-correlation signal z must time-shift to the left over x in Δt steps. For each time shift $k \cdot \Delta t$, each value of z_{i+k} faces a value of x_i . The summation for all i of multiplication of this two values provides the cross-correlation for the k -shift. The cross-correlation for a discrete signal is:

$$cc_k^{<x,z>} = \sum_i x_i \cdot z_{i+k}$$

Figure 27 plots the cross-correlation for signals x and z . This figure demonstrates that for time shift $k=0$, nonzero x amplitudes face zero z amplitudes at low values of t_i , at high values of t_i , the opposite happens. Therefore, the multiplication is zero, i.e. the cross-correlation for $k=0$ is zero. As signal z time-shifts to left over x , i.e. k increases, the cross-correlation starts to have nonzero values. It increases until it reaches its maximum values then it decreases again as z passes x . As z passes x , right end of x has no values of z to face, therefore imaginary entries to z must be added. If both signals x and z have N value, signal z must be extended to $2N-1$, so k can be shifted past x from $k=0$ to $k=2N-1$. The imaginary entries can be zeros. The peak of the cross-correlation curve is time shift between the two signals. When two signals have reverse polarity, the peak may be a negative value; therefore, a plot of absolute value of the cross-correlation is often preferable.

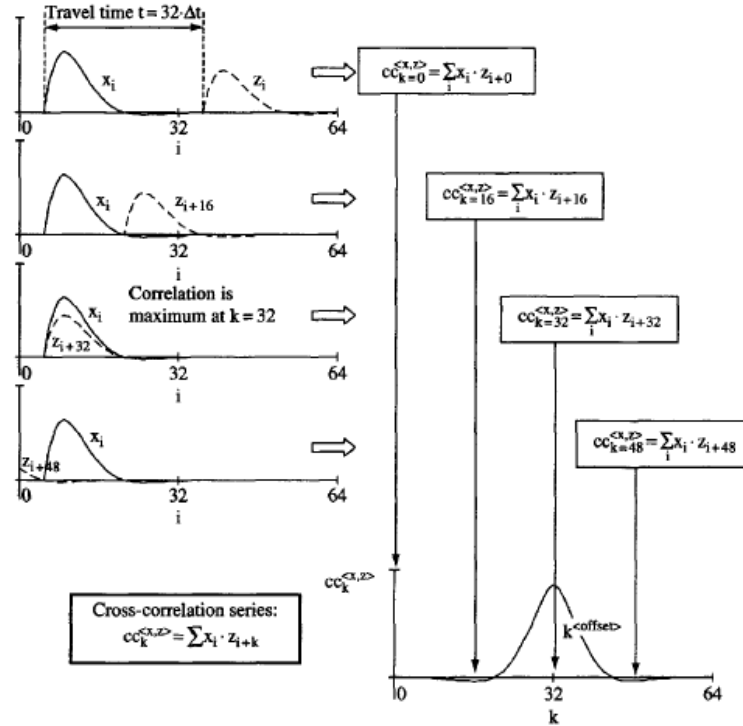


Figure 27 (Santamarina & Fratta, 2005)

Soil is a dispersive medium, for that reason, different frequencies travel with different phase velocities. The figure shows the cross-correlation versus k for a typical Bender elements input and output signal. Figure 28 shows these two signals with their cross-correlation and its maximum peak, which is negative here. This maximum peak corresponds to the path with the most traveling energy. It demonstrates here that time shift between two signals is 1.1 ms which can not be guessed from the original signals a) and does not correspond to the first deflection, first peak or highest peak.

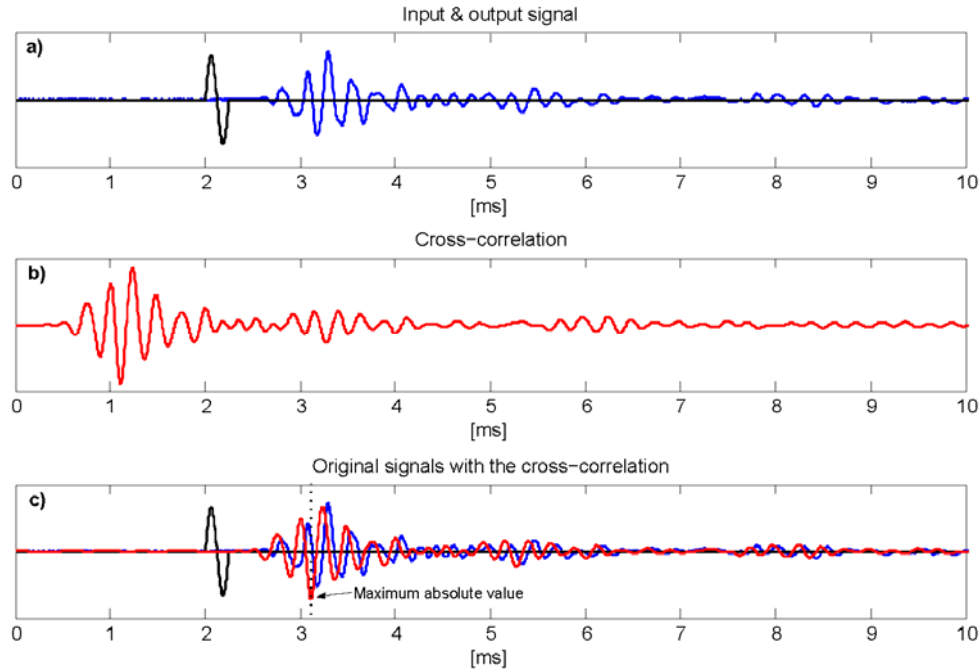


Figure 28. a) Typical input and output signal in a bender elements test; b) cross-correlation of the input and output signals; c) detecting travel time by determining the maximum absolute value

2.4.4 Auto-correlation method

Auto-correlation is a special case of the cross-correlation. It is the cross-correlation of a signal with itself:

$$ac^{<x>} = cc_k^{<x,x>} = \sum_i x_i \cdot x_{i+k}$$

Figure 29a shows the same input and output signal from a typical bender elements test as in Figure 28. An auto-correlation of the output signal is plotted in figure b. It shows the second and the third arrival of signal. The signal travels is excited at the source and transmitted through the soil sample until it is received by the receiver causing the first arrival. It goes back to the source then back again to the receiver causing the second arrival. In the auto-correlation plot, the maximum value occurs at 0-time shift, and the second arrival can be determined at 2.2 ms. This is two travel times. One can calculate one travel time by dividing by 2, which gives 1.1 ms, that is the same value derived from the cross-correlation in Figure 28. Although the third arrival can be detected, however, the highest peak cannot be easily determined, as shown in Figure 30.

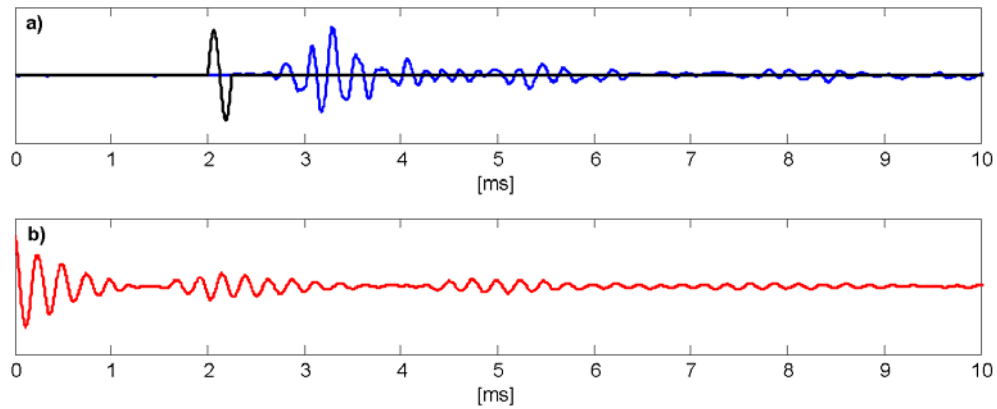


Figure 29. a) Typical input and output signal in a bender elements test; b) auto-correlation of the input and output signals

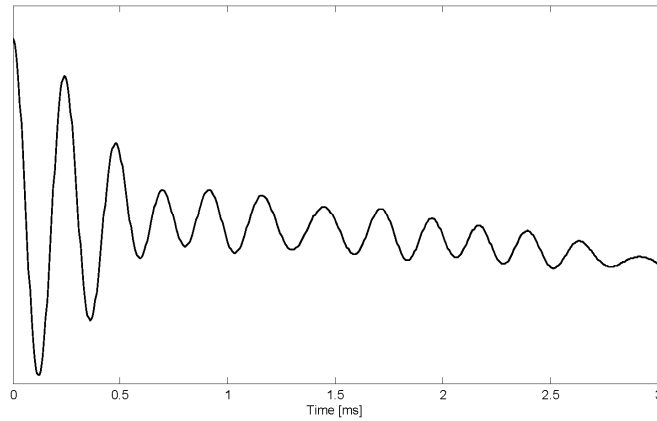


Figure 30. Auto-correlation in a bender elements test

2.5 Summary

In this chapter, a general outline of the small-strain tests in both in-situ and laboratory was given. The in-situ tests do not show the effects of other conditions than the current in-situ condition. They require specialized costly equipment and experienced operator and sometimes boreholes in addition to complicated data interpretation. Some of these tests are limited. There is a variety of sources of errors (i.e. background noise, groundwater table effects). The laboratory tests give the opportunity to measure the small-strain under different conditions, but unfortunately, there is limited number of such tests with a number of disadvantages in each. Bender elements may give a good alternative test to measure G_{max} .

While measuring density and effective length looks easy, determining travel time seems to be problematic due to many reasons like the near-field effect. Although there are many methods in the time and frequency domain to determine the travel time, the first arrival is the basic problem in this test, and it is still under discussion. Since there is no standard for this test, comparison between tests from different laboratories should be carefully done. Bender elements tests measurements showed good agreement with measurements from resonant frequency test. Concepts of interpretation methods are shown. Further discussion about uncertainty and limits of them is given in the next chapters.

Chapter 3

Equipment

A system was built to make tests possible and effective. A set of hardware and software were put together to carry out the experiments. The equipment used in this research contains the following parts:

- Pair of Piezoelectric bender elements installed in a triaxial cell as shown in Figure 33 to produce the shear waves and receive it. The bender elements have the following dimensions: length=14.2 mm, height (penetration)=10 mm, thickness=1.5 mm.
- Triaxial cell modified to adapt the bender elements shown in Figure 33. The bender elements are installed in the base and cap of the cell. The cell is grounded to avoid cross-talk and isolated to minimize noise.
- Twin-burette volume change indicator, which is connected to the manual air pressure valve and to the cell. The pressure can be applied through this burette, while volume change of the cell water can be measured.
- Manual or a digital air pressure controller to control the pressure in the cell.
- Open-system burette connected to the specimen. In the saturation condition, this burette can measure pore water volume change. This provides an extra possibility to measure the volume change during the test for a saturated sample.
- Signal amplifier (M68D3) shown in Figure 35, to amplify and to filter the output signal. This is a special amplifier for dynamic measurement with piezoelectric sensors with 3 amplifier channels and Adjustable low-pass filter and high-pass. In all tests a 50kHz-low-pass filter was used and a 1000x amplification.
- Data logger (NI USB-6251) shown in Figure 34 from National Instruments to record data over time and transfer analog signal (i.e. transducer signal) to digital one and vice versa. It also sends the signal that excites the bender element. The National Instruments USB-6251 is a USB high-speed multifunction data acquisition (DAQ) module optimized for superior accuracy at fast sampling rates with 16 analog inputs (1.25 MS/s sampling rate and 16 bits resolution) and 2 analog outputs (2.8 MS/s sampling rate and 16 bits resolution).
- Personal computer with LabVIEW program installed, in order to control and save the input and output signals. LabVIEW is a platform and development environment for a visual programming language from National Instruments. The advantage of this program is, it allows the signal to be saved for further analysis and offers full control over signal excitation, i.e. to excite different waveforms, frequencies, amplitudes and sampling rates. A LabVIEW program was written which sends a signal to the bender element through the data logger in different waveforms and frequencies, and saves received signal.

The whole testing system is sketched in Figure 31 and photographically shown in Figure 32.

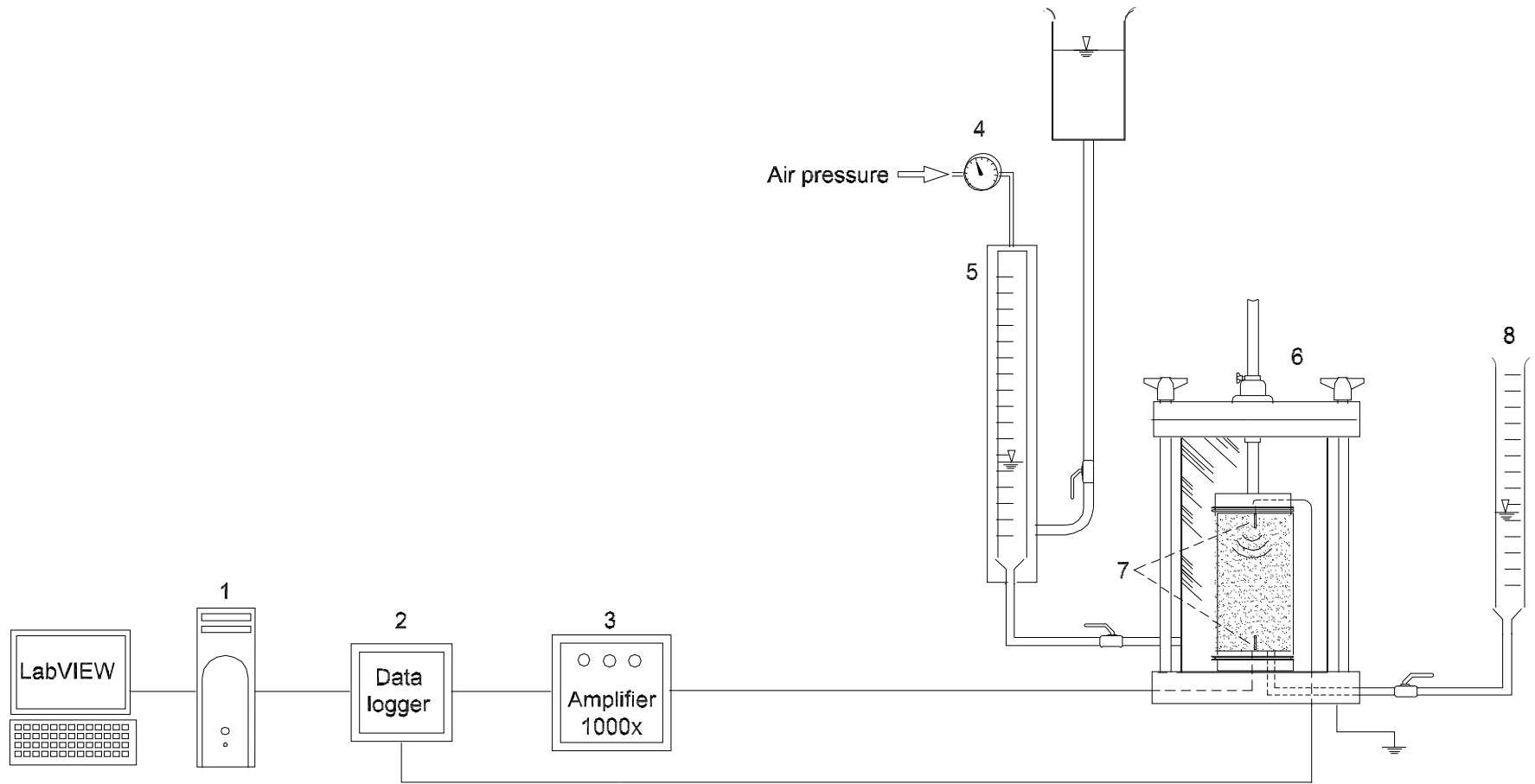


Figure 31. Laboratory system for bender elements test. 1: PC with LabVIEW program; 2: data logger; 3: amplifier; 4: manual air pressure valve; 5: twin-burette volume change indicator; 6: triaxial cell; 7: bender elements; and 8: burette.



Figure 32. Laboratory system for bender elements test.

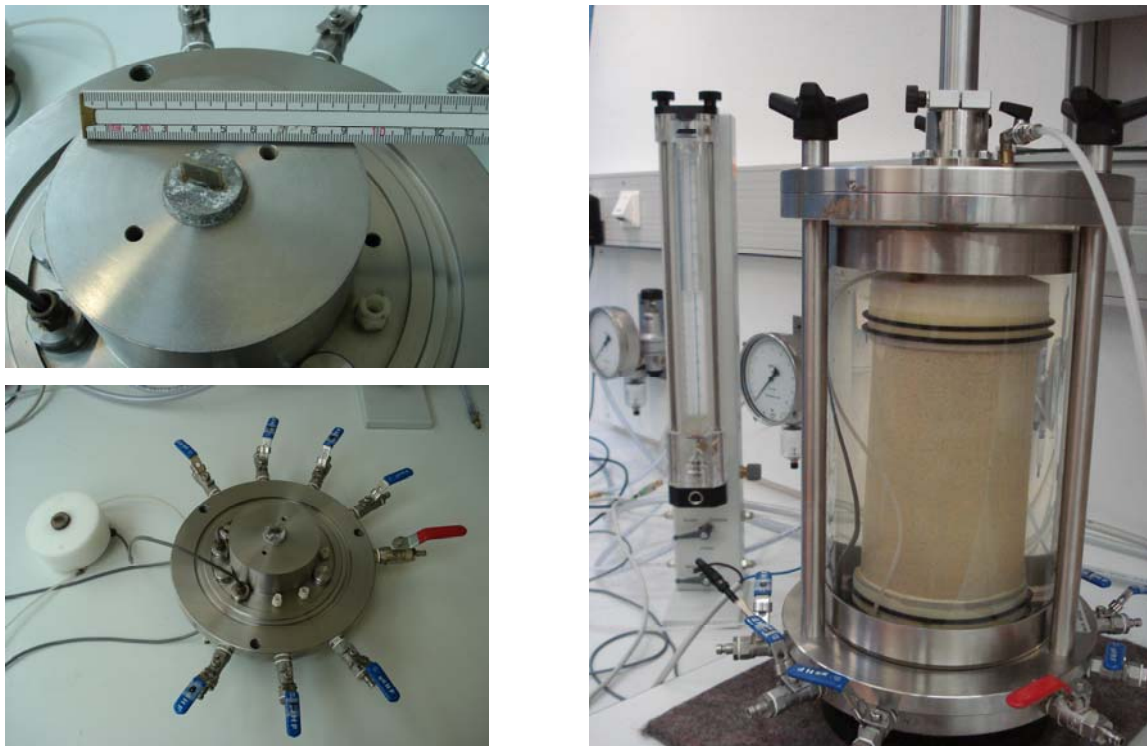


Figure 33. Left top: bender element installed in the triaxial cell; left bottom: the base and the cap of the triaxial cell; right: the triaxial cell with a sample built inside.



Figure 34. Data logger



Figure 35. Signal amplifier

Chapter 4

Material Properties and Testing Program

4.1 Material properties

Material used in this study is divided into two groups; natural material and artificial material. 6 Natural material were used. Their properties were determined and are shown in Table 2. Constants d_{50} and $C_u = d_{60}/d_{10}$ are derived from the grain size distribution shown in Figure 36.

Table 2. Properties of natural material.

Material	d_{50} [mm]	C_u [-]	ρ_{\min} [g/cm ³]	ρ_{\max} [g/cm ³]	e_{\min}	e_{\max}	G_s
S#1	0.2	1.43	1.396	1.658	0,568	0,862	2,60
S#2	0.33	1.81	1.361	1.609	0.647	0.947	2,65
S#3	0.33	5.13	1.623	1.914	0,376	0,622	2,633
S#4	0.38	1,95	1.446	1.699	0,559	0,832	2,65
S#5	0.62	2.46	1.422	1.715	0.542	0.859	2,644
S#6	0,63	3.56	1.576	1.789	0,481	0,682	2,65

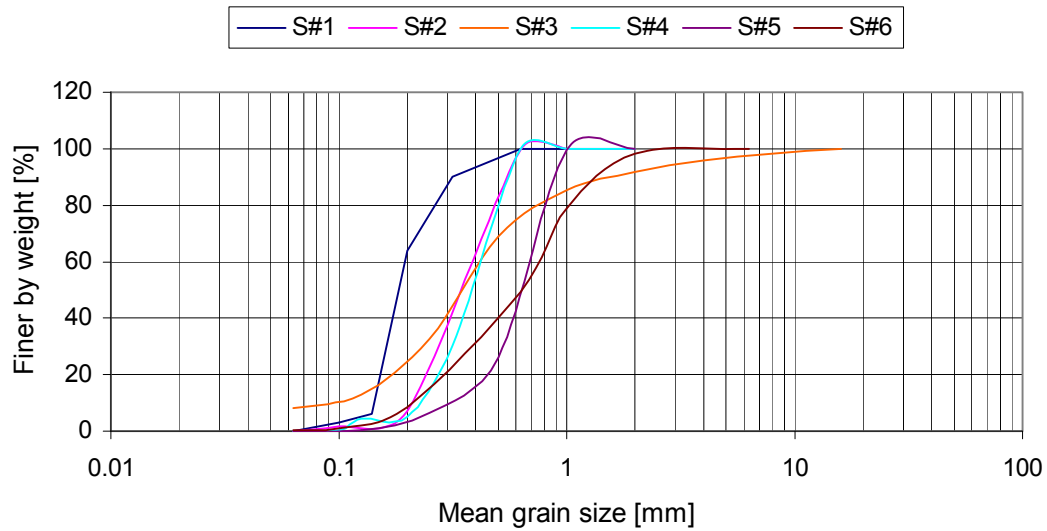


Figure 36. Grain size distribution for all natural materials.

Table 3. Physical properties of glass beads.

Void ratio e	Dry density ρ [g/cm ³]	Specific gravity, G_s	Diameter [mm]
0.684	1.485	2.5	3.5
0.684	1.485	2.5	8

As artificial material uniform round glass beads were used with two different diameters; 8 mm and 3.5 mm. Both materials have the same specific gravity and round shape. This produces the same void ratio and density.

4.2 Testing program and procedure

A triaxial cell is used to perform the tests. Specimen is cylindrical with diameter of 10 cm and height of 20 cm. The largest particle size is less than 1/6 of the specimen diameter.

For dry test, specimen mold is placed around the rubber membrane. The mold is filled with sand in 12 layers; each compacted to specific height corresponding to the wanted density. In case of minimum density (e_{\max}), material is put carefully from minimum height.

For saturated test, the mold is filled with water simultaneously to material filling. The water should be few centimeter above sand level to ensure full saturation. Before removing the mold, 5-10 kPa suction must be applied. This suction can be applied by means of air vacuum pump for dry material or by placing the burette which is connected to the sample water about 50-100 cm beneath the sample level for saturated material. After removing the mold and measuring the sample dimensions, the cell then is filled with water and 10-kPa isotropic pressure is applied. This is considered as zero point for following measurements of volume change.

Following values of isotropic pressure are applied to each sample: 10-25-50-100-200-400 kPa. At each pressure, volume change is measured by a burette, which is connected to the cell water. The cell together with the burette is calibrated in order to calculate the volume change of the specimen. In the case of saturated material, additional volume change measurement can be done by another burette, which is connected to the sample water. From volume change measurements, void ratio at each pressure step can be calculated. For dry and saturated conditions, the specimen is always drained, thus effective pressure equals confining pressure. After applying the pressure at each step, one should wait until the volume is constant, then wave velocity measurements start. The bender elements transmitter is excited by LabVIEW program as described in chapter 3, where the following types of waveforms and frequencies are tried:

- 1-period-sinus with 1- to 15-kHz frequency.
- 1-period-Rectangle with 5-kHz and 10-kHz frequency.
- 1-period-Triangle with 3.3-kHz frequency.
- Ricker 0. order with 5-kHz frequency.

- Seidl-Müller with 14.2 kHz frequency.

In addition to all previous forms with reversed polarization in order to determine the first deflection.

This process is done using LabVIEW program shown in Figure 37 and the data logger. The program was developed in laboratory of Soil Mechanics in Bauhaus-Universität Weimar. For all waveforms and frequencies, input and output time histories are saved on the computer for the purpose of digital signal processing.

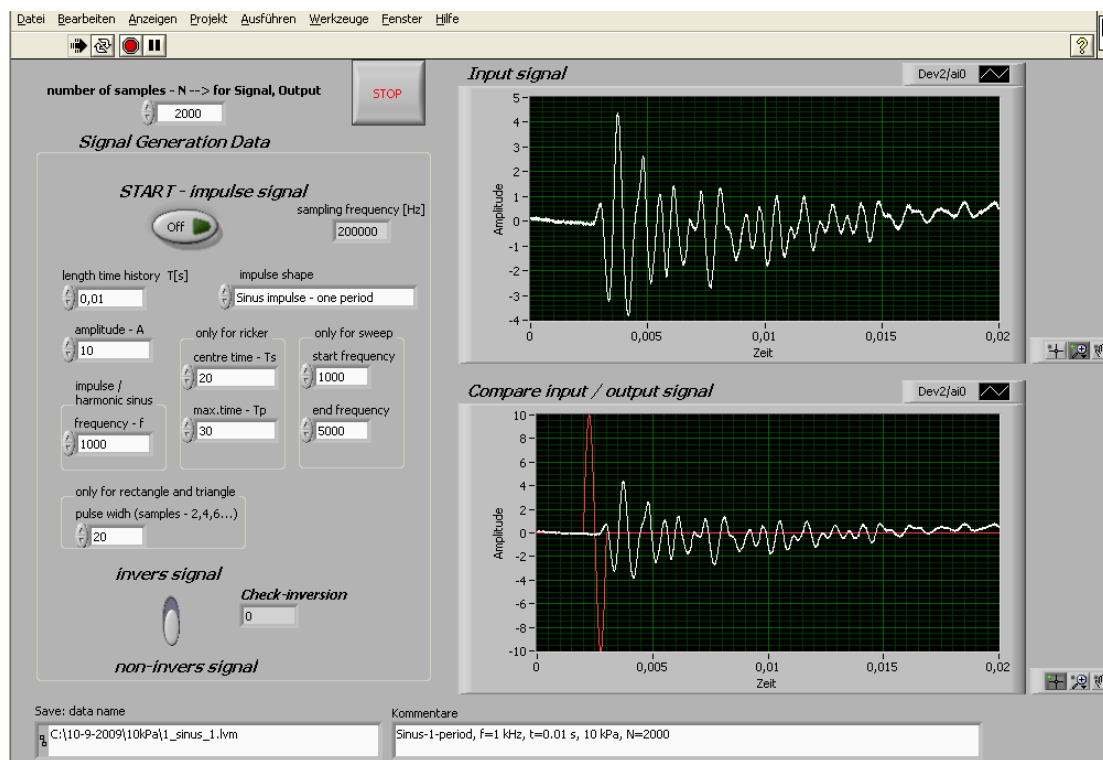


Figure 37. LabView program as used in this study.

Chapter 5

Experimental Considerations

5.1 Introduction

Many settings regarding collecting measurements and analyzing them should be done. The triaxial cell must be calibrated to avoid any errors in measuring volume change and grounded to avoid any cross-talk due to electrical effects. Directivity of bender elements is also studied here and its effect on amplitude and signal shape is determined. After applying each pressure step, sample needs some time to adapt its new volume. In order to estimate waiting time after applying pressure, volume change behavior and its relationship with shear wave velocity is examined. An analysis to determine the optimal waveform and frequency is described in details. Evaluation of interpretation method described in chapter 2 is presented also in this chapter with the intention of choosing the best one to derive shear wave velocity.

5.2 Cell Calibration

When the pressure increases through a test, the cell walls expand. This causes immediate volume change that can affect the volume change measurements of the cell water. Beside pressure, there is time effect also. When pressure is applied on the cell for some time the cell starts to creep. For the previous reasons the cell and other equipment used in the tests (e.g. burette) must be calibrated in order to correct the measurements. Cell walls may absorb water under pressure. This effect is neglected since test time is relative short. This calibration was implemented in all tests calculations in this research.

To perform this calibration the following steps were done following the constructions described by (Head, 1986):

- The equipment used for tests is connected together as in a typical test in this research. This equipment contains: the cell with the bender elements installed inside; a twin-burette volume change indicator; a digital air pressure controller and a stainless steel dummy with high stiffness to replace the actual soil sample. This calibration was carried out in a temperature-controlled room to avoid any water or cell expansion or contraction due to temperature change.
- Filling the cell and all connections completely with fresh de-aired water, making sure that no air bubbles are entrapped.
- Applying pressure on the cell by mean of the air controller. The volume change was measured at each step by means of the twin-burette volume change indicator. The pressure was applied stepwise in 50 kPa steps through the range of 0 to 400 kPa, which is the range of tests carried out in this research.
- At each step, a waiting time of one day was achieved; in order to calibrate the time effect due to the cell creep. After one day, another measurement of the volume change was taken before going forward to the next pressure step.
- Decreasing the cell pressure back to 0 kPa in decrement of 100 kPa and taking reading for immediate volume change.

Figure 40 shows the development of the cell volume change through time. At each cell pressure the volume change jumps immediately then continues to increase in the following day due to the cell creep. At the next day, the reading is taken from which the time effect is calculated, and then the next pressure step is applied. The figure shows that the cell volume change is significant and cannot be neglected. The total cell volume change was as high as 32.2 cm^3 . Therefrom, 23 cm^3 are immediate volume change that happens in the first few minutes and 9.2 cm^3 are due to time effect.

Figure 41 demonstrates that time effect causes almost 40% of the immediate volume change at all pressures. The increasing of is almost linear.

In this figure, immediate volume change due to pressure increase was calculated which is shown in the previous figure then compared with pressure decrease path where just immediate change was allowed with no one-day-waiting time. Figure 42 shows clear elastic behavior of the cell, therefore, no change in the cell behavior is expected due to loading-unloading cycles.



Figure 38. Calibration of triaxial cell with a steel dummy



Figure 39. A steel dummy used to calibrate the triaxial cell

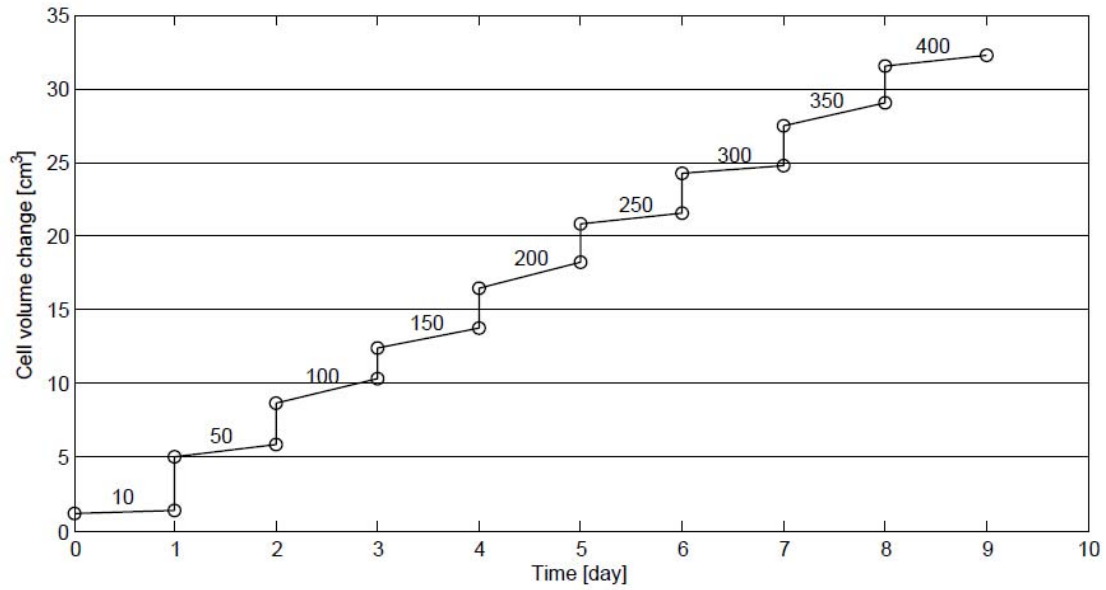


Figure 40. Immediate and creep volume change of the triaxial cell versus time

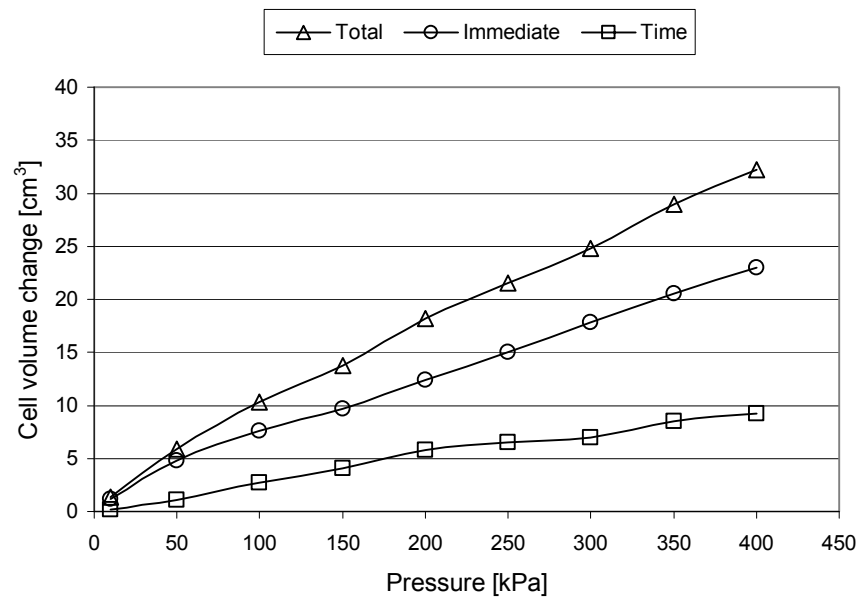


Figure 41. Immediate, creep and total volume change of the triaxial cell versus isotropic pressure

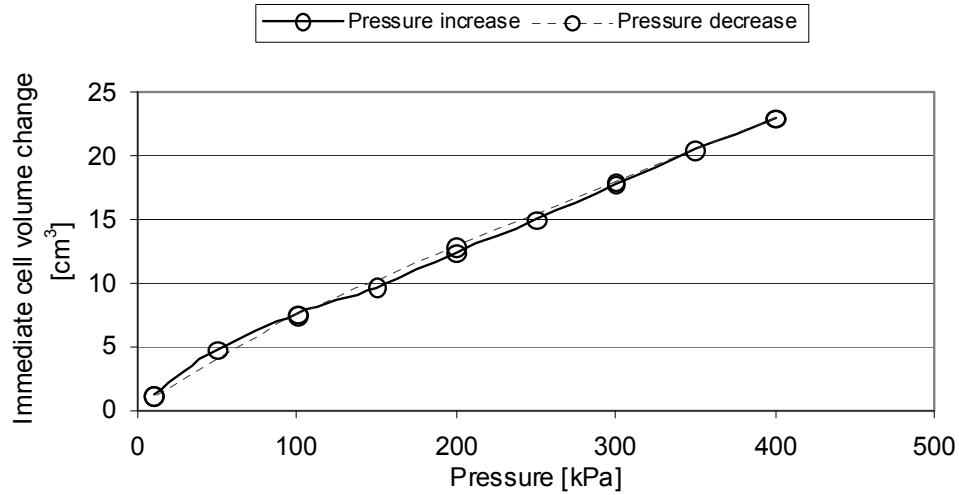


Figure 42. Immediate cell volume change versus pressure for loading and unloading

5.3 Grounding

In order to have a clear output signal with high signal-to-noise ratio, any electrical noise must be avoided. A test was carried out to check the effect of grounding the triaxial cell. A signal was excited with and without grounding and the result is shown in Figure 43. For ungrounded cell, output signal is extremely noisy and very difficult to interpret. Cross-talk between elastic wave and electric wave is obvious at the first arrival of the output signal. This cross-talk is due to electric wave propagation through cell frame which made of metal. When cell is grounded, no such noise is noticed. Therefore, triaxial cell in bender elements test must be grounded.

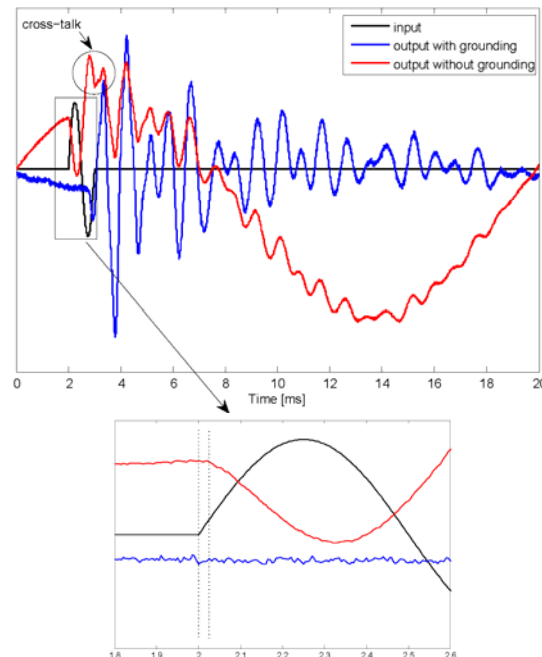


Figure 43. Input and output signal with and without grounding.

5.4 Out-of-plane directivity

In order to study the effect of directivity on the bender elements, a test with different angles between bender elements planes was carried out. The axes of both source and receiver coincide while the upper bender element rotates stepwise about its axis by angle θ as shown in Figure 44. A sinusoidal signal of one period was sent from the source to measure the amplitude change in the output signal due to rotation. To ensure the highest amplitude possible, the sample was constructed in a loose density and the frequency of 2.3 kHz was chosen. Readings were taken at θ values of 0° , 15° , 30° , 45° , 60° , 75° , 90° and results are shown in Table 4.

In Figure 45 and Figure 46, one can notice that for angles between 0° and 30° the amplitude is not significantly different, while but first deflection changes for the same range. for values 15° and 30° , the signal is earlier deflected than for angle 0° . Starting from angle 45° , the output signal amplitude starts to decrease till it is about 4 times smaller for 90° . At values 75° and 90° the amplitude is significantly smaller that at 0° . This test shows that both bender elements planes must be parallel in order to have maximum amplitude possible and to avoid false early arrival.

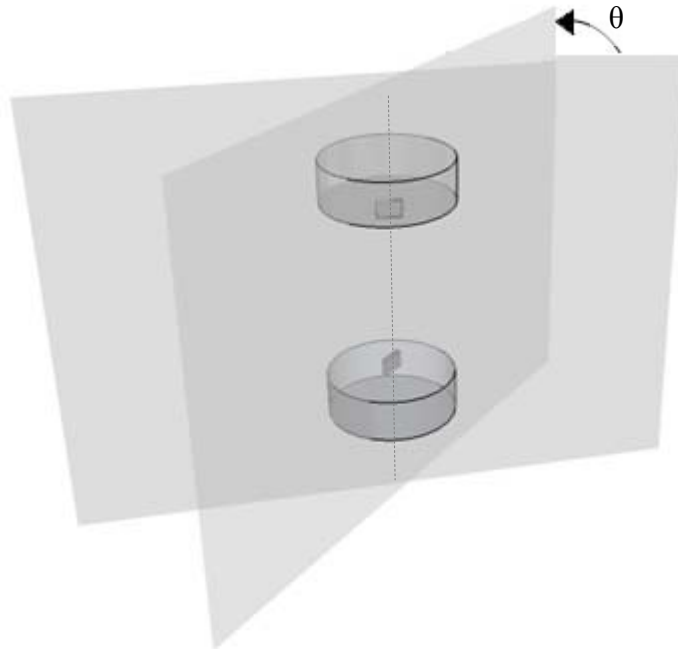


Figure 44. Top and base of the triaxial cell. The top piece is rotated by angle θ .

Table 4. Amplitudes for different rotation angles.

θ	0°	15°	30°	45°	60°	75°	90°
A_θ of 1 st peak [V]	4.26	4.6	3.97	2.98	2.98	0.98	1.01
A_θ of 2 nd peak [V]	4.11	5.53	4.95	4.23	3.61	1.18	1.37

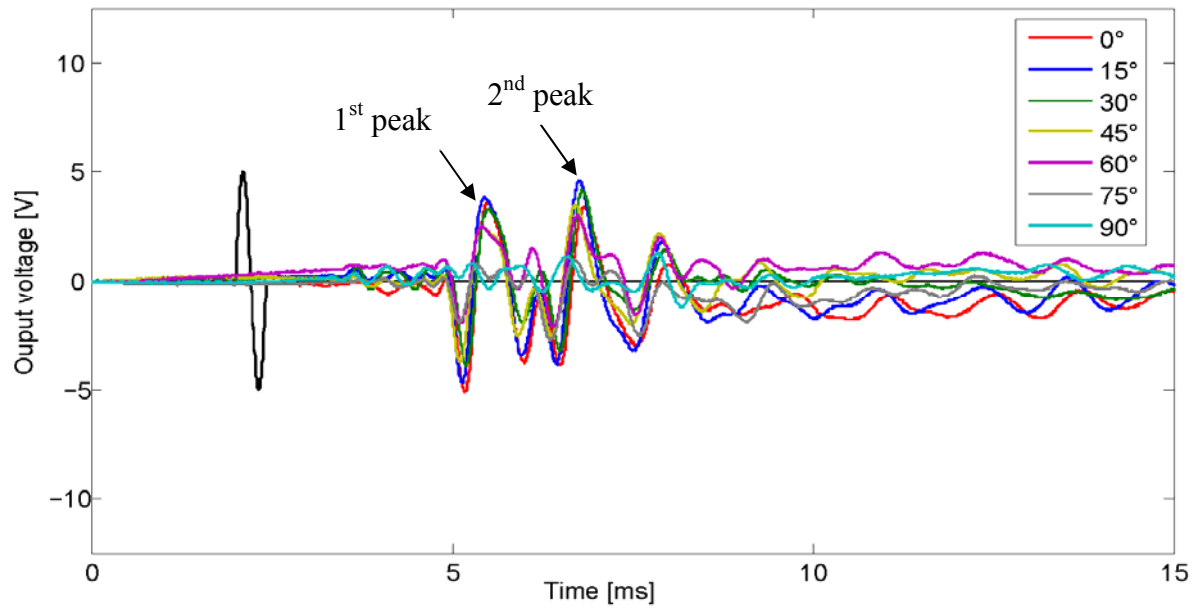


Figure 45. Input and output signals for different rotation angle θ

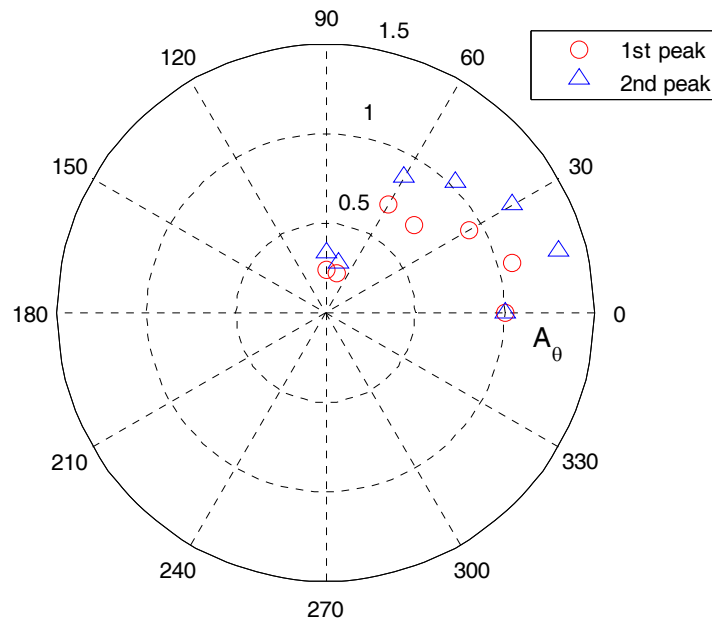


Figure 46. Amplitude of 1st and 2nd peak from Figure 45 versus θ . Amplitudes are normalized to amplitude at 0° of each peak

5.5 Waiting time

After applying confining pressure, sample takes some time to achieve balance. In the meanwhile, sample volume decreases which can be measured by the twin-burette. Sample reaches its balance when its volume change is zero. In order to investigate waiting time needed, a sample was tested by bender elements in a triaxial cell. Confining pressure was stable at 400 kPa for a long time to ensure stability of the sample, then, a 50-kPa-step was applied. Shear wave measurements were taken every 10 minutes as shown in Figure 47. Slight shift of peaks are observed in Figure 47 bottom, from which relative change in velocity could be calculated. In the meanwhile, volume was measured. Velocity and volume were normalized to their value after 60 minutes as shown in Figure 48. Volume change is stable after 10 min. The increase after that in volume is due to cell expansion. While velocity change continues to increase and is only stable after 20 min. The increase in velocity at the end is probably due to aging or creep. Therefore, for all tests in this study, waiting time of 30 minutes was completed to guarantee that sample has reached its balance and the correct shear wave velocity is measured.

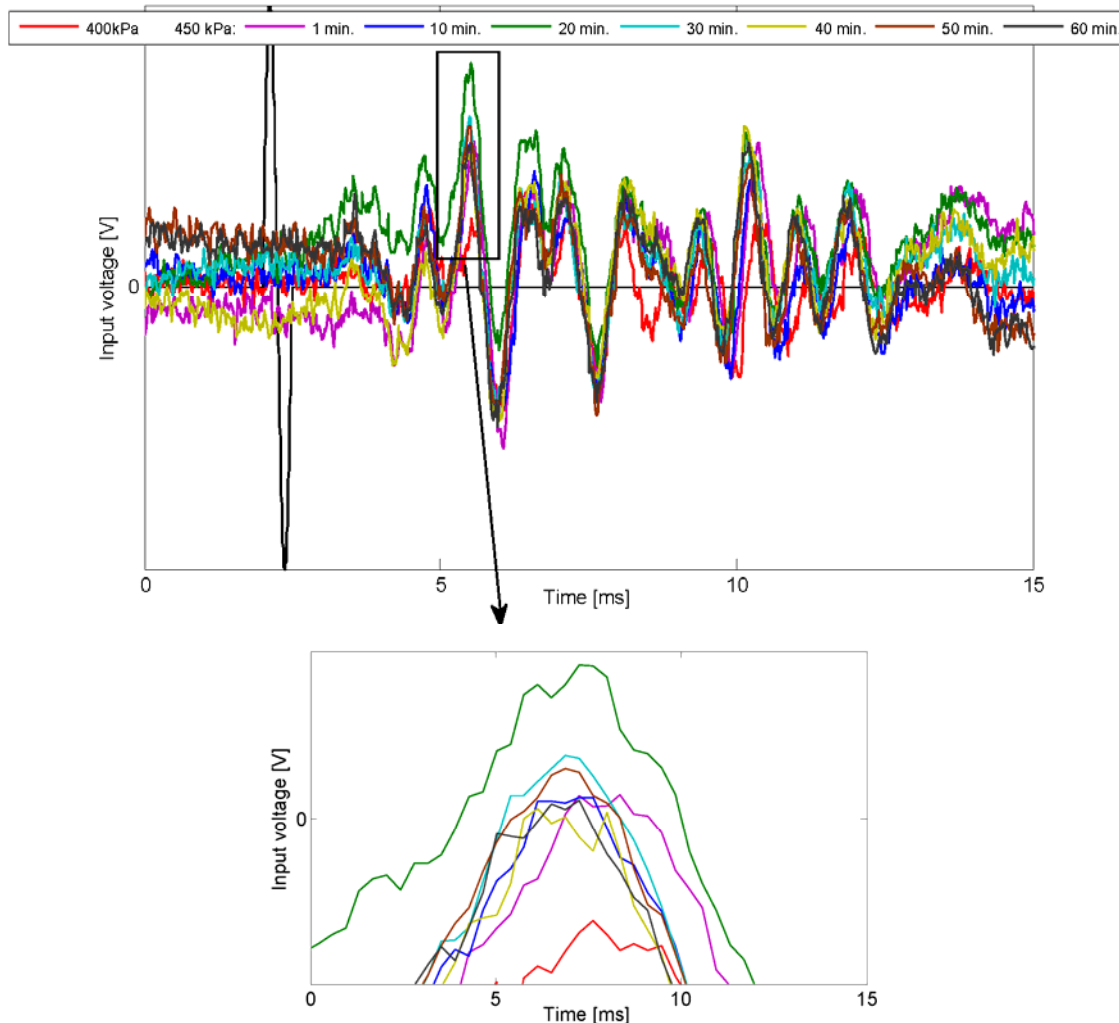


Figure 47. Input and output signals for different waiting times

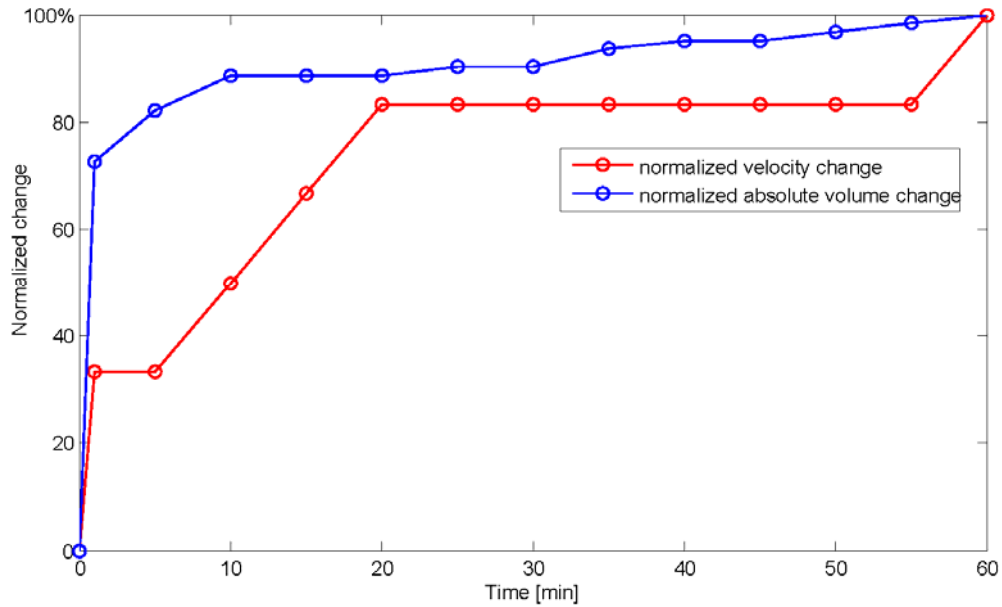


Figure 48. Normalized velocity and volume change with time

5.6 Waveforms

As shown in Table 5, many waveforms have been tried to excite bender elements. No specific one has won the agreement of all researchers. In this study, an attempt was carried out to find the optimal waveform for the bender elements test. Many waveforms were excited for the same dry sample of material S#1 at the same isotropic pressure, 100 kPa. These waveforms have the following properties:

- Sine, with frequency of 5 kHz and peak-to-peak voltage of 20 V.
- Rectangle, with frequency of 10 kHz and peak-to-peak voltage of 20 V.
- Rectangle, with frequency of 5 kHz and peak-to-peak voltage of 20 V.
- Triangle, with frequency of 3.3 kHz and peak-to-peak voltage of 20 V.
- Ricker of 0. order, with frequency of 5 kHz and peak-to-peak voltage of 10 V.
- Seidl Müller, with frequency of 14.2 kHz and peak-to-peak voltage of 10 V.

Figure 49 shows the input and output signals of these waveforms. The sinusoidal wave generates a clear first arrival and a smooth signal with large amplitude. A rectangular waveform with 10 kHz was also tried. It shows a very scattered output signal with ambiguous first arrival that makes it very difficult to determine the velocity by the first deflection method. This scatter is due to the wide range of frequencies this kind of waveform includes. When this waveform was tried with 5 kHz frequency, it gave a better result in the sense of amplitude and clearness. However, the output signal is still scattered and not enough smooth as the sine waveform offers. Additionally, the output signal does not resemble the input one. The sharp rise of the input signal cannot be found in the

output one. For the triangular input signal, the output looks acceptable, more smooth than the rectangular one. Nevertheless, when this waveform was compared with the sinusoidal wave with similar frequency, the later seemed less scattered and with larger amplitude. The second arrival was slightly clearer for the sinusoidal one. Furthermore, the triangular waveform includes wider range of frequency content than the sinusoidal one. This is also true for the Ricker wave. Both triangular and Ricker have outputs which do not resemble the input, for example, the sharp peaks are lost in the output signal. For the Seidl Müller waveform, it was extremely scattered. The first arrival could not be determined.

Based on the previous analysis, the sinusoidal waveform is optimal one in terms of clearness, amplitude and frequency content. Therefore, it was chosen to execute all signals in this study.

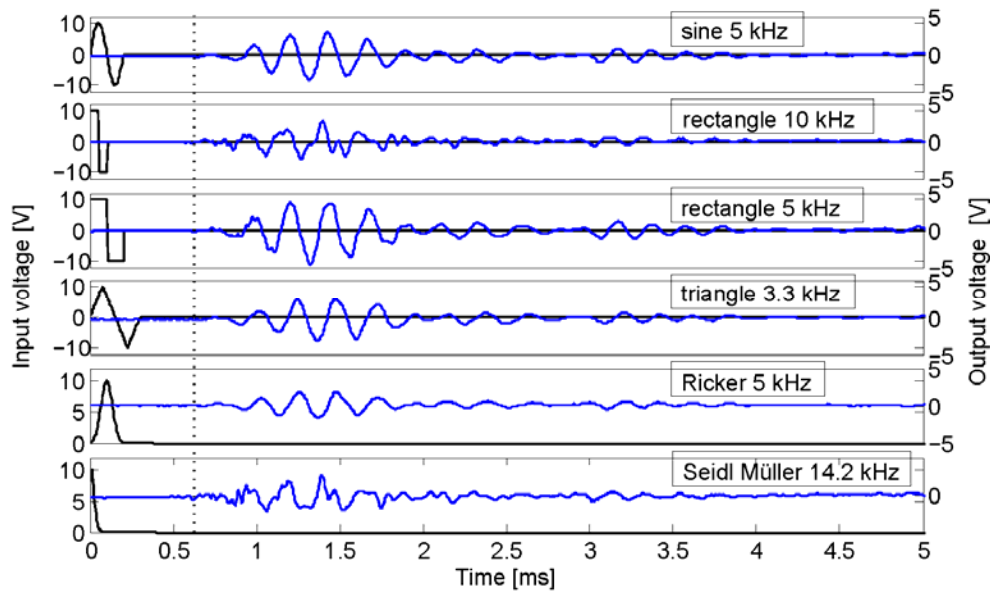


Figure 49. Different waveforms as input signals with their output signals.

5.7 Frequency

Many researchers (e.g. Jovičić et al., 1996; Brignoli et al., 1996) proposed using higher frequency to avoid the near-field effect. On the other hand, high frequencies correspond to low amplitudes, because the resonant frequency of the bender elements is usually low. The Technical committee, TC29 (Stress-strain and Strength Testing of Geomaterials) of International Society of Soil Mechanics and Geotechnical Engineering (ISSMGE) found that there is no clear effect of input frequency in case of the saturated samples but for dry specimens it seems that scatter is slightly on the higher side at lower frequencies. However, these findings have no agreement with many researchers such as (Brignoli et

al., 1996; Jovičić et al., 1996; Sanchez-Salinero et al., 1986; and Lee & Santamarina, 2005) among others. Table 5 demonstrates the frequency range and waveforms used by some researches in the literature. As shown, there is no trend to use a specific value for frequency.

In order to study the influence of frequency on shear wave velocity in the bender elements test, many time histories from all tests in this study were analyzed. Shear wave velocity was calculated in different methods and plotted versus frequency. In the next sections, velocity fluctuation with frequency is studied, and effects of interpretation method, saturation and isotropic pressure on this fluctuation are analyzed.

Table 5. State of the art for frequency and waveforms used in bender elements test.

Reference	Used frequency [kHz]	Waveform
Shirley, 1978	4	Sine
Dyvik & Madshus, 1985	0.005, 0.1	Square
Viggiani & Atkinson, 1995	0.05, 1-10	Sine, square
Arulnathan et al., 1998	15, 7.5, 3.7, 1.9	Sine
Fioravante & capoferri, 2001	3.2, 7.5, 10, 15, 18, 20, 30, 40	Sine, rectangle, harmonic
Lings & Greening 2001	10	Sine
Pennington et al., 2001	8-25	Sine wave with phase shift
Dano et al., 2003	5	Sine
Mohsin & Airey, 2003	1-30	Sine, 2- or 3-period-sine, triangle, chirp
Lee & Santamarina, 2005	0.5, 1, 4, 12, 40	Sine, step
Leong et al., 2005	0.5, 2, 4, 8, 16	Sine
Chen & Zhou, 2006	10, 12.5, 15, 17.5, 20, 55, 60	Sine
ISSMGE, 2007*	0.1-60	Sine, rectangle

*after 23 reference

In Figure 50, different signal arrivals are shown. The measurements were taken for sand S#1 in dry condition at 100kPa. The frequency range was 1 to 15 kHz. This figure shows the range of the first deflection of the output signal and the range of the signal arrival calculated by the first deflection, peak-to-peak and cross-correlation method for a frequency range of 1 to 15 kHz which is the range used in this study.

Figure 50 shows that the first deflection method demonstrates a wide range of first arrival. This range is as large as 0.25 ms. The fluctuation of shear wave velocity calculated by this method with frequency is demonstrated in Figure 51. The first deflection is strongly dependant on the near-field effect (Sanchez-Salinero et al., 1986; Jovičić et al., 1996). There are many evidences in the literature of the uncertainty of this method (e.g. Viggiani and Atkinson, 1995).

The range of the first peak is also shown in the figure. In some cases, some characteristics of the signal change with frequency. The first peak decays with frequency increase and another peak appears in different position. The obviousness of the first peak depends on the amplitude of the output signal, thus, on the frequency of the input signal and soil attenuation. Therefore, it is difficult to detect it in saturated sample or at high isotropic pressure where signal amplitude is small. In the peak-to-peak method, the first peak of the output signal is compared with the first peak of the input signal. The first peaks of the input signals are shifted due to frequency change in a wider range than the first peaks in the output signals. This is an extra reason for which the time delay in this method changes with frequency. However, detecting the first peak was difficult in many cases. For the previous reasons, the peak-to-peak method does not give reliable results.

Most of the arrivals of the cross-correlation concentrate at 3.37 ms, while the others distribute at a range of 0.22 ms. The early arrivals correspond to the low frequencies. Soil is dispersive medium, i.e. different frequencies have different phase velocities and their attenuation is also different. The cross-correlation method seeks the highest energy in the output signal and compares it with the highest energy in the input signal. Therefore, the cross-correlation detects the highest energy arrival (group velocity) and not necessary the first arrival of the signal. This is the reason of the scatter in its values in Figure 50. At high frequencies, it shows the same value. However, this scatter has smaller effect on the velocity than the first deflection method since its time delay is larger.

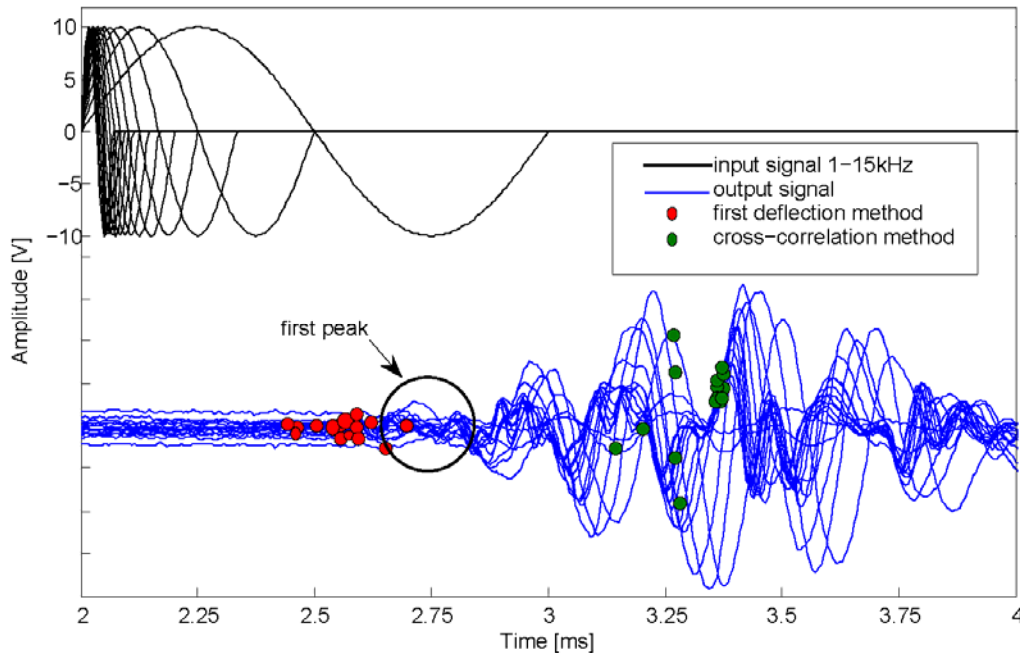


Figure 50. Different output signals for input signals with frequencies 1 to 15 kHz. Travel time is illustrated here with different interpretation methods

In Figure 51, shear wave velocities calculated by different methods are plotted versus frequency. The shear wave velocity was calculated in 4 different methods: first deflection; peak-to-peak; cross correlation and auto-correlation. The first deflection and the peak-to-peak methods show unstable values when frequency changes. The peak-to-peak method demonstrates extremely high value at 1 kHz. This is due to the length of the input signal, as it takes place even after the output signal starts to arrive. The auto-correlation curve seems more constant but it is hard to determine its velocity at some frequencies most of the time, since the second arrival could not be detected. In most tests, the second arrival was not detected at all, especially for saturated condition where attenuation is higher.

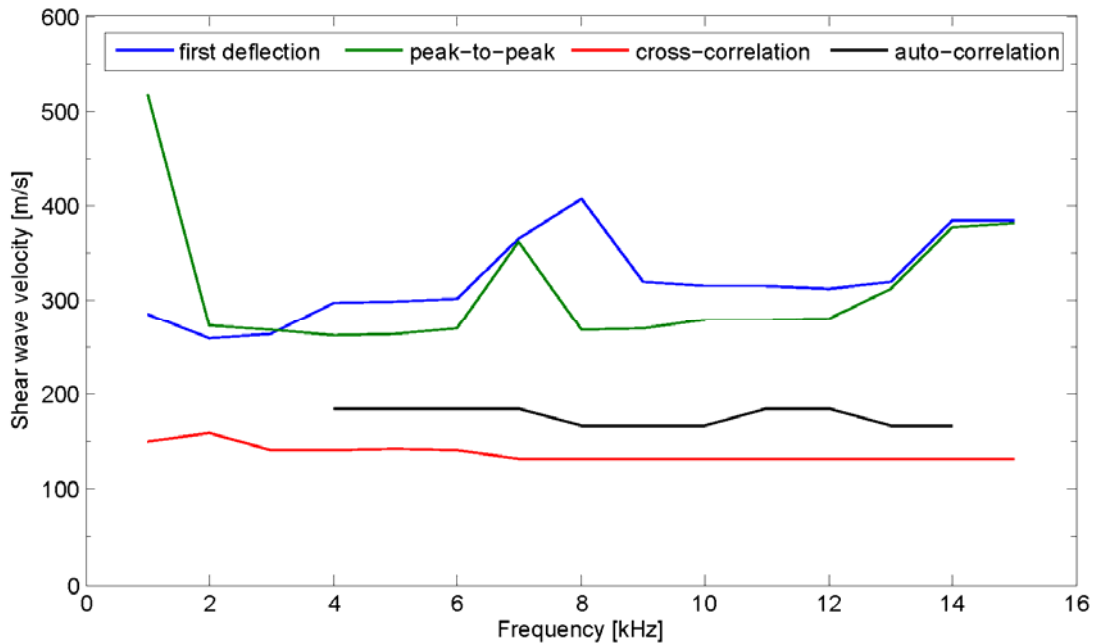


Figure 51. Shear wave velocity determined by different interpretation methods versus frequency

5.7.1 Effects on Fluctuation

Some factors affect the way velocity fluctuates with frequency. These factors were studied in order to better understand wave propagation and to choose the optimal input frequency for the bender elements test.

- *Saturated vs. dry*

In Figure 52, a comparison was made for velocity fluctuation with frequency between dry and saturated samples. The velocity was calculated by the first deflection method, and then normalized to the velocity at 1 kHz frequency. Calculating the velocity by the peak-

to-peak and cross-correlation methods showed similar results. The standard deviation of this fluctuation was calculated using the following formula:

$$s = \sqrt{\frac{\sum (x - \bar{x})^2}{n-1}}$$

where \bar{x} is the sample mean average and n is number of samples. The standard deviation of dry samples was slightly smaller than for saturated samples. It decreases from 12% in average for all saturated samples to 10% in average for all dry ones.

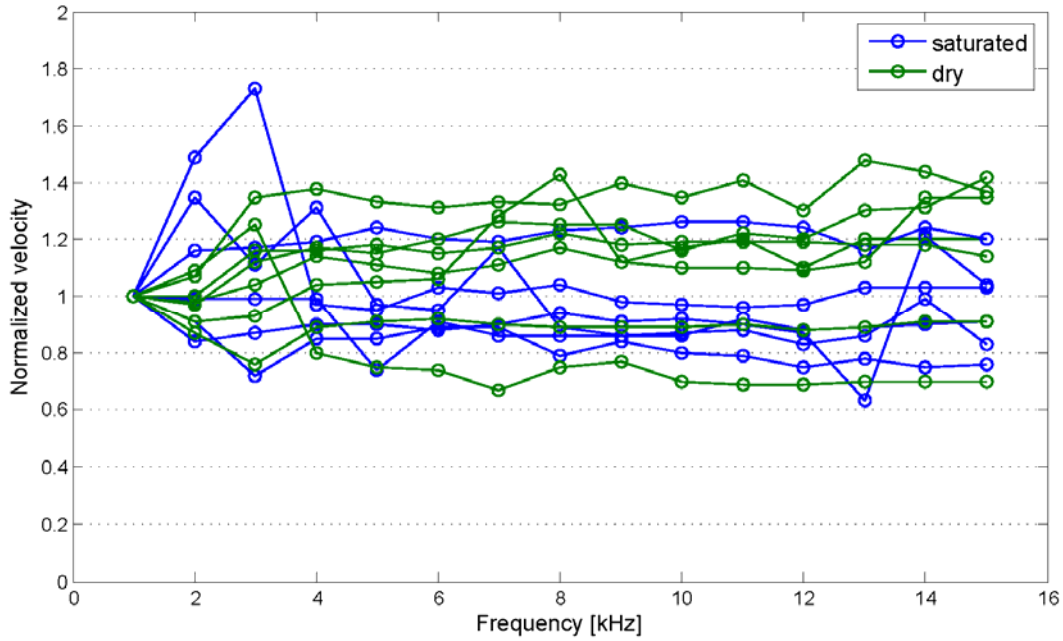


Figure 52. Normalized shear wave velocity versus frequency for saturated and dry samples. Velocity is normalized to velocity at frequency 1 kHz

- *Isotropic pressure*

Figure 53 illustrates fluctuation for the same sample at two isotropic pressures (100 and 400 kPa) for test# 15. There is no significant difference in frequency fluctuation between these two pressures. The standard deviation is 16% at 100 kPa while it is 14% at 400 kPa where attenuation is lower. Attenuation may filter some frequencies, which decreases the fluctuation. This might be the reason why velocity fluctuation with frequency is higher for low isotropic pressure and saturated samples.

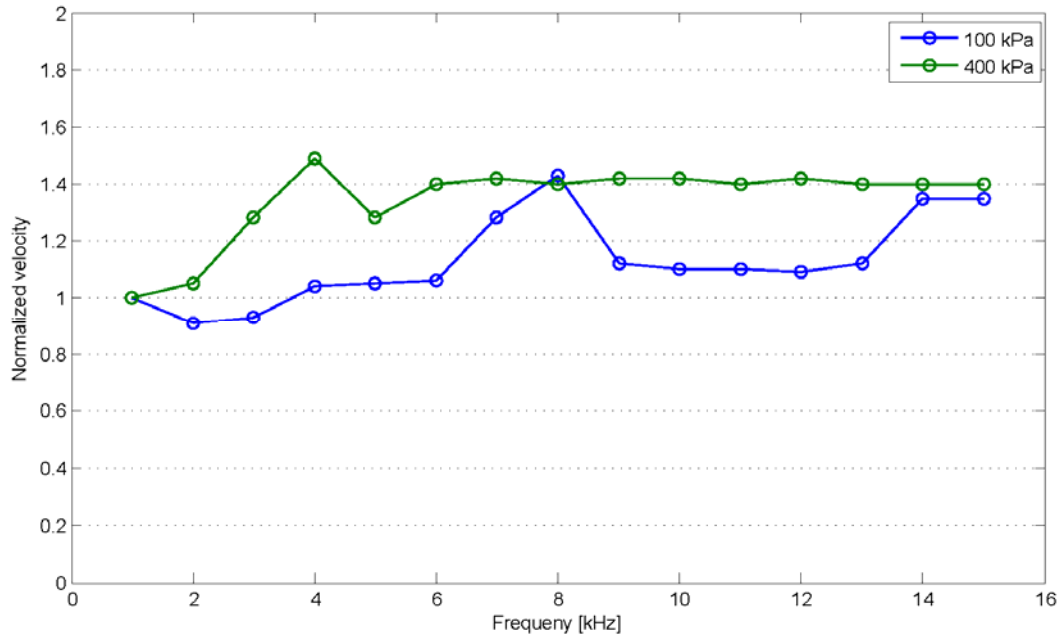


Figure 53. Normalized shear wave velocity versus frequency at different isotropic pressure. Velocity is normalized to velocity at frequency 1 kHz

- *Interpretation method*

In order to estimate the best interpretation method to derive the shear wave velocity, the later was calculated for all samples at isotropic pressure 100 kPa by three methods: first deflection, peak-to-peak and cross-correlation. For each sample, the velocity was calculated for frequencies 1 through 15 kHz for a one-period-sinusoidal input signal. Then, velocities of each method were normalized to velocity at 1 kHz. Figure 56 through 7 show fluctuation of velocity with frequency for all three methods. Each line in these figures represents one sample. The figures demonstrate that a clear trend for velocity change with frequency cannot be found, i.e. a relationship between velocity and frequency cannot be derived. The lines are almost equally distributed around horizontal line 1. That means, velocity increases with frequency in some cases and decreases in others. These figures indicate that scatter is especially large for low frequencies, and tend to decrease as frequency increases. Many researchers proposed exciting high input frequency to avoid the near-field effect. Using high frequencies did not ensure constant velocity when first deflection method is considered as shown in Figure 54. Because at high frequencies, amplitude is considerably smaller than low frequencies, thus, determining the first deflection in the output signal is more difficult.

Velocity calculated by cross-correlation in Figure 56 seems to be unstable at low frequencies, while it is less scattered at frequencies higher than 7 kHz. This observation is also clear in Figure 50. This makes the cross-correlation method the less effected method by input frequency if frequencies between 7 and 15 kHz are considered.

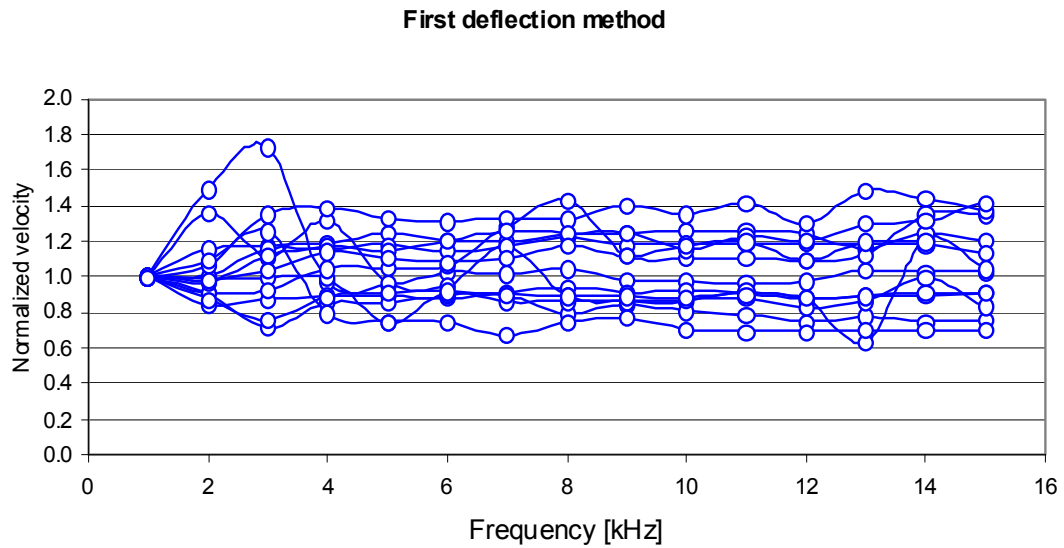


Figure 54. Normalized shear wave velocity determined by the first deflection method versus frequency for all natural samples. Velocity is normalized to velocity at frequency 1 kHz

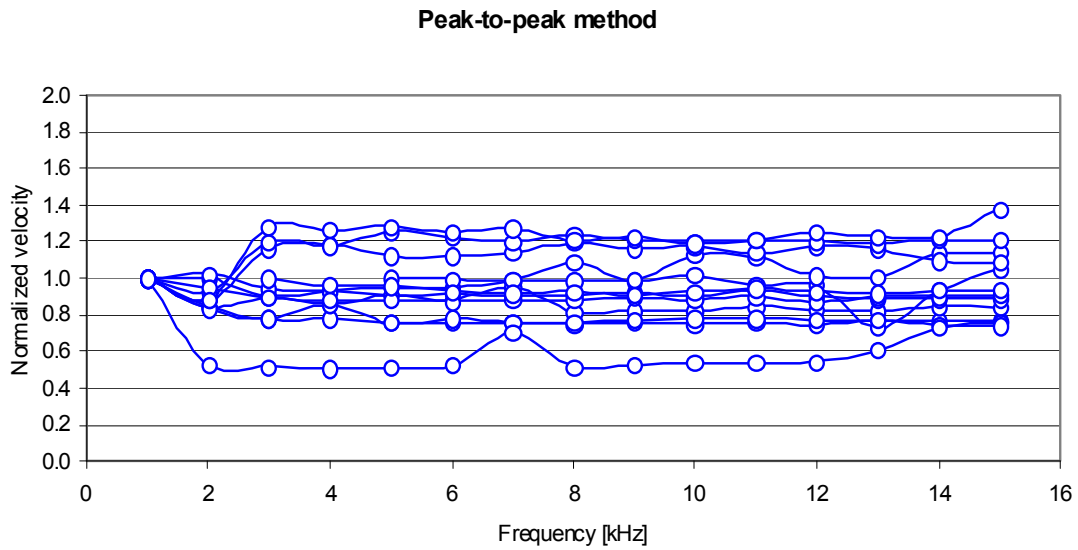


Figure 55. Normalized shear wave velocity determined by the peak-to-peak method versus frequency for all natural samples. Velocity is normalized to velocity at frequency 1 kHz

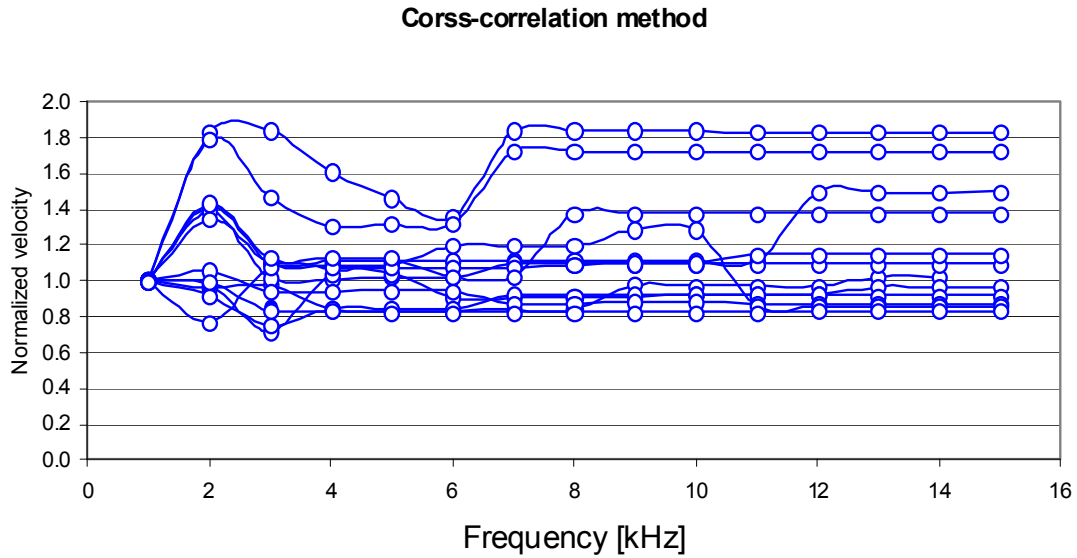


Figure 56. Normalized shear wave velocity determined by the cross-correlation method versus frequency for all natural samples. Velocity is normalized to velocity at frequency 1 kHz

5.8 Summary

Critical test parameters and important settings were examined in this chapter. Cell behavior was quantified by calibrating the cell. Pressure and time effects on cell volume were determined. Thus, error due to cell expansion is minimized. In this study, cell is grounded and bender elements are parallel to each other. After applying each pressure step, waiting time of 30 minutes was found to be enough so that sample is stable. Regarding input signal, it was proven that a sinusoidal waveform with 20-V amplitude gives clear, smooth and strong output signal. Frequency strongly affects results of shear velocity. This effect is slightly smaller for dry samples and high pressures. The cross-correlation method with frequencies between 7 and 15 kHz was proven to be the most reliable interpretation method and thus adapted for all signal processing in this study.

Chapter 6

Study of Natural Material

6.1 Introduction

In this chapter, test results of all 6 natural materials are presented. During these tests, measured time histories for all samples at confining pressures of 10, 50, 100, 150, 200, 250, 300, 350, 400 kPa were analyzed using the cross-correlation method in order to determine the shear wave velocity. At each pressure, volume change was measured and bender elements were excited by shear waves. Shear wave velocity was determined using the cross correlation method described in chapter 2, considering sinusoidal waveform. Influence of confining pressure p was studied and a relationship between shear modulus G_{\max} and confining pressure is determined. The dependence of this relationship on coefficient of uniformity $C_u=d_{60}/d_{10}$ is examined. Since volume change is measured, sample volume, density and void ratio at each pressure could be calculated, thus, dependence of shear wave velocity on void ratio is discussed. Data from this study were compared with most common empirical equations to predict G_{\max} in order to evaluate them. Furthermore, results from a series of resonant columns tests on materials #1, #3 and #4 were compared with data of same materials from bender elements tests analyzed in different interpretation methods. Finally, a comparison between experimental data from bender elements and resonant column and theoretical predictions was performed.

6.2 Methodology

Figure 57 shows input and output signal for saturated sample of sand #4 at 100 kPa for 11 kHz frequency. Cross-correlation was calculated for these signals and plotted in its absolute value as described in chapter 5. Then, the maximum peak of the cross-correlation curve is determined. This peak indicates travel time between input and output signal. Based on analyzing a lot of time histories in this study, no specific character in the output signal corresponds to this cross-correlation peak. As discussed previously in chapter 5, frequencies between 7 and 15 kHz and waveforms of sinus were used to excite the transmitter. From travel time, shear wave velocity can be calculated by dividing sample length by travel time. Effective sample length is considered the distance between bender elements tips. This is typically $200-2 \times 10 = 180$ mm. From measuring volume change during the test, volumetric strain for all samples was found to be around 1%. This makes axial strain negligible. Shear modulus G_{\max} was calculated from the elastic wave propagation theory:

$$G_{\max} = \rho V_s^2$$

where G_{\max} is in Pa, ρ is mass density in Kg/m^3 and V_s is shear wave velocity in m/s. In the saturated condition, shear modulus was calculated from shear wave velocity considering mass density not total density as discussed by (Youn, et al., 2008) based on Biot's theory. Table 6 shows exemplary calculation process and values for saturated sample #4 (The same sample of Figure 57). G_{\max} values are showed for all confining pressure values of one test. Such calculation process was done for all tests. Table 7 shows initial parameters for all tests on natural material.

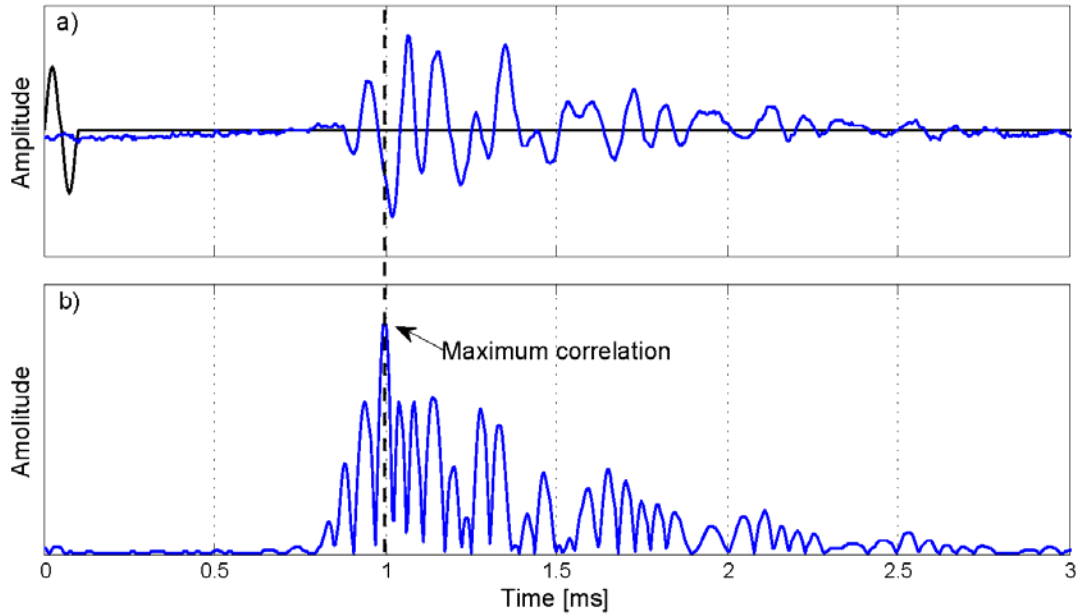


Figure 57. Determining travel time for saturated sample of sand #4 at 100 kPa. a) input signal for 11 kHz with its output; b) cross-correlation for input and output signal and determining the maximum value.

Table 6. Sample of calculating shear wave velocity and G_{\max} for saturated sample of sand #4.

Pressure [kPa]	Travel time [ms]	Velocity [m/s]	Volume [cm ³]	Void ratio e	Mass density, ρ [g/cm ³]	Relative density, D_r [%]	G_{\max} [MPa]
10	1.68	105.54	1587.55	0.756	1.509	27.84	16.81
50	1.21	146.53	1581.30	0.749	1.515	30.37	32.53
100	1.00	178.19	1573.20	0.740	1.523	33.66	48.35
150	0.90	197.00	1570.45	0.737	1.526	34.77	59.21
200	0.84	211.07	1568.35	0.735	1.528	35.62	68.06
250	0.79	225.86	1565.92	0.732	1.530	36.61	78.05
300	0.75	236.40	1564.70	0.731	1.531	37.10	85.57
350	0.72	247.97	1563.50	0.729	1.532	37.59	94.22
400	0.68	262.67	1561.05	0.727	1.535	38.58	105.89

Table 7. Initial parameters for all tests on natural material.

Material	Condition	$\rho_{d,i}$ [g/cm ³]	e_i [-]	$D_{r,i}$ [%]
S#1	dry	1.435	0.812	16.90
	saturated	1.472	0.766	32.63
S#2	dry	1.425	0.860	28.99
	saturated	1.393	0.902	14.95
S#3	dry	1.657	0.589	13.60
	saturated	1.731	0.521	40.97
S#4	dry	1.497	0.770	22.62
	saturated	1.509	0.756	27.84
S#5	dry	1.526	0.733	39.88
	saturated	1.522	0.737	32.86
S#6	dry	1.576	0.682	0.18
	saturated	1.627	0.627	26.99

6.3 Influence of confining pressure

After calculating G_{\max} values at different confining pressures, variation of G_{\max} with confining pressure p could be examined. Figure 58 and Figure 59 show G_{\max} versus p for all natural material. As one can see, G_{\max} increases considerably with pressure increase. These curves are nearly linear in the double-logarithmic scale, which suggests a relation of $G_{\max} \sim p^n$. In order to determine the exponent n and compare all tests with each other, shear modulus was normalized in each test with its initial value at 10 kPa. Figure 60 and Figure 61 demonstrate the increase of shear modulus G_{\max} with confining pressure p for all dry and saturated natural samples respectively.

Dry samples

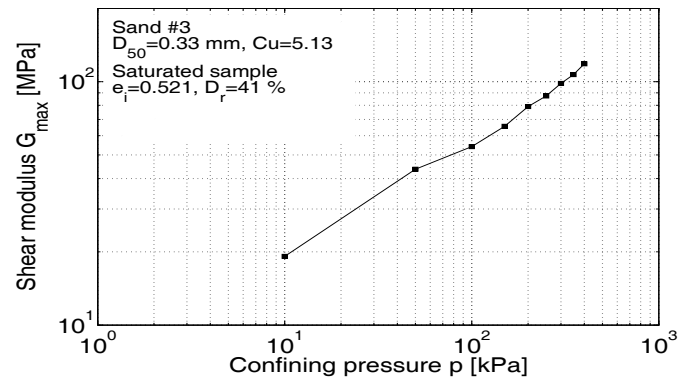
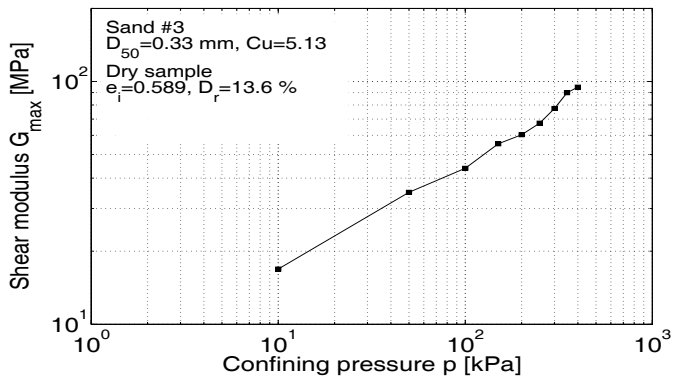
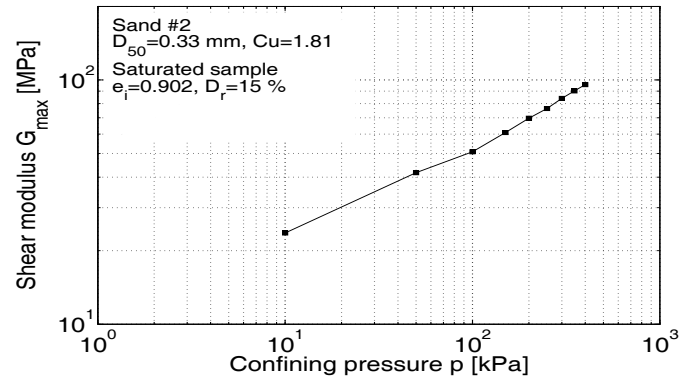
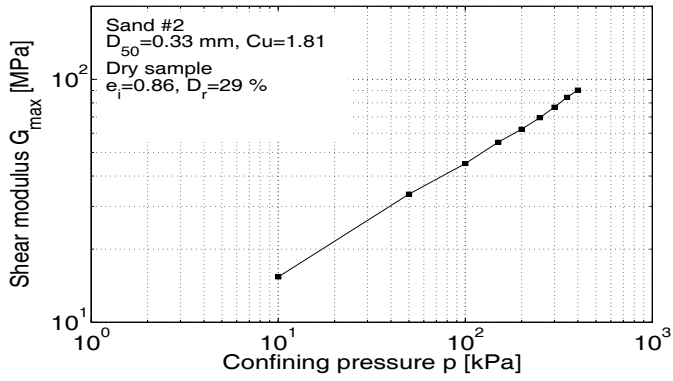
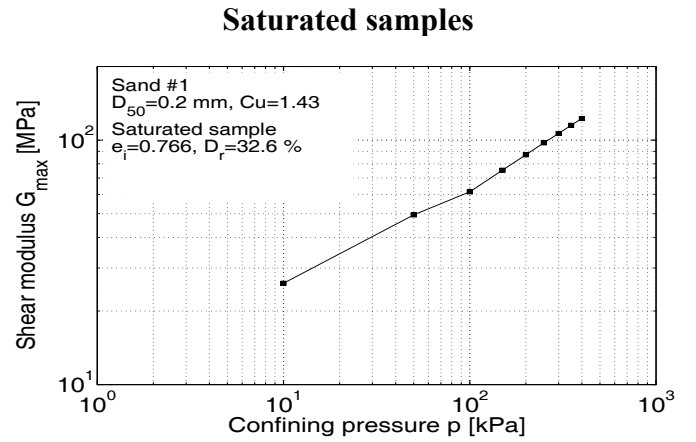
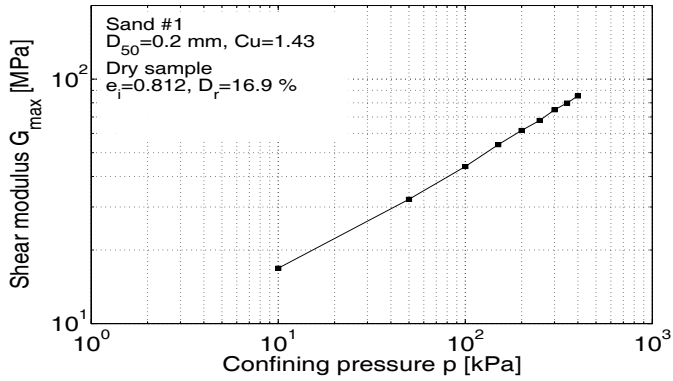
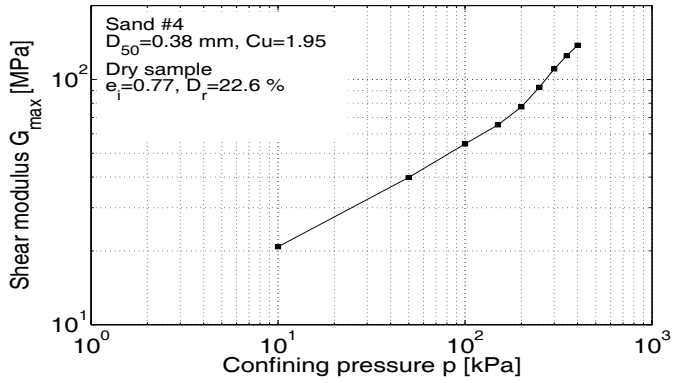


Figure 58. Increase of shear modulus G_{max} with confining pressure p for natural materials #1, #2 and #3.

Dry samples



Saturated samples

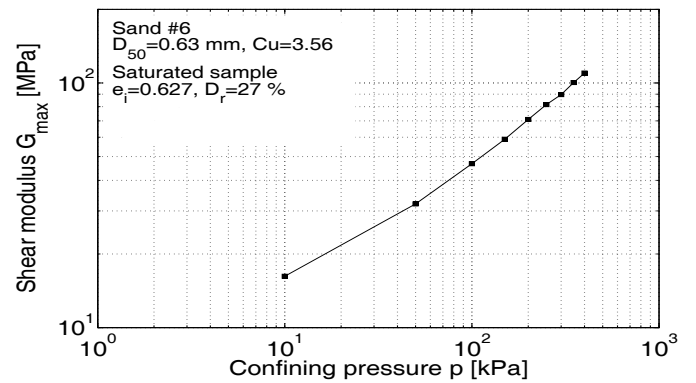
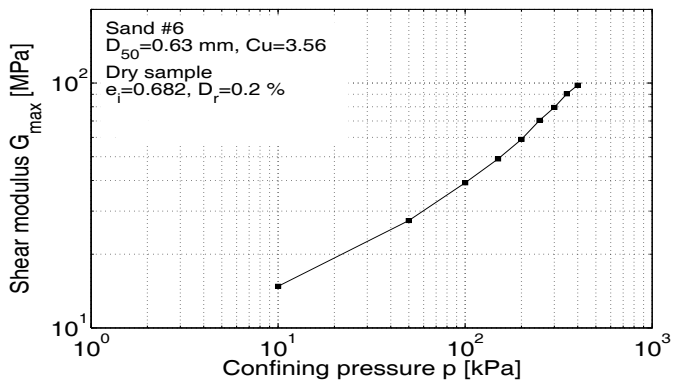
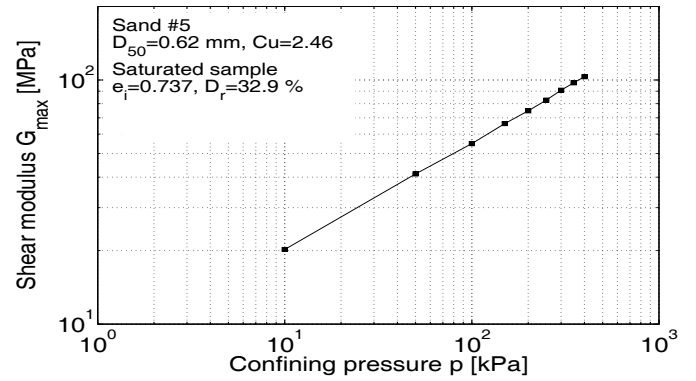
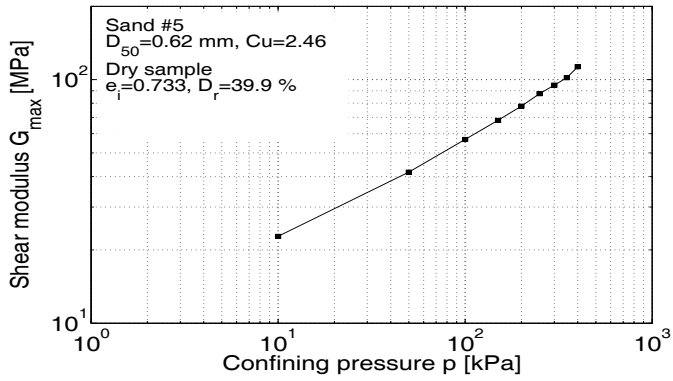
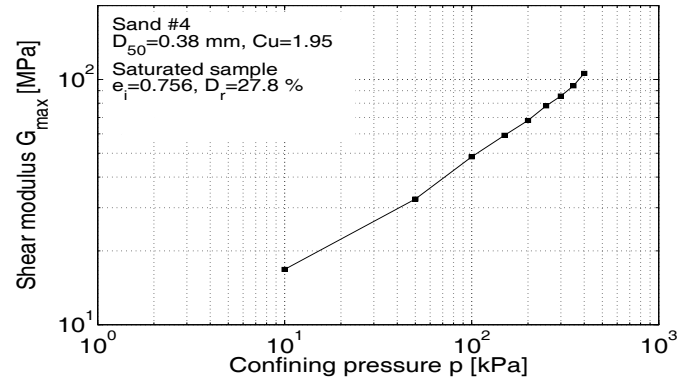


Figure 59. Increase of shear modulus G_{max} with confining pressure p for natural materials #4, #5 and #6.

In Figure 60, dry samples seem to have a similar behavior with nearly linear curves. These curves were least-square fitted to estimate the exponent n . Table 8 shows values of exponent n for all dry and saturated samples. The mean value of n for all dry samples was found to be 0.54. Figure 61 shows G_{\max} increase with confining pressure p for all saturated samples. Value on n is 0.5 in average for saturated samples. The curves lay in a wider range than those for dry samples. That means, the exponent n is more scattered for saturated case. This scatter might be due to signal lower amplitude in saturation condition than dry one, which makes signal analyzing and shear wave velocity determining more difficult and less accurate. These n values are in good agreement with value from literatures. Exponent n is typically around 0.5 as proposed by (Hardin & Richart, 1963). Many recent studies use n -value in the range of 0.40 to 0.55 (Hoque & Tatsuoka, 2004; Kallioglou & Papadopoulou, 2003; Kuwano & Jardine, 2002). Thus, values of exponent n from 12 samples in this study are in good agreement with values from literature.

Usually in literature, void ratio change during a given test is neglected. Shear modulus increase is ascribed only to confining pressure increase. In this study, volume change of the sample was measured, thus void ratio could be calculated at each pressure step. Figure 62 shows the decrease of void ratio e due to pressure increase. Since initial void ratios of different samples were different, e was normalized to its initial value e_i at confining pressure 10 kPa. As indicated in Figure 62, the decrease of void ratio in all 12 samples is not the same. This is because initial void ratio of samples is not equal, even relative density is similar but not identical. At low relative densities, volume change is expected to change quicker, while at high relative densities, volume change slows down till the sample reaches its maximum density. The void ratio decrease in Figure 62 is about 5% in average and can be up to 9%. That means, a part of the shear modulus increase is a result of void ratio decrease not only confining pressure increase. In order to estimate G_{\max} and thus exponent n accurately, change in G_{\max} due to void ratio change can be calculated using the most common void ratio function, which was proposed by (Hardin & Richart, 1963) and since then, has been extensively used:

$$f(e) = \frac{(2.17 - e)^2}{1 + e}$$

$f(e)$ was calculated at 10 kPa and 400 kPa for each test. $\Delta f(e)/f(e)$ indicates $\Delta G_{\max}/G_{\max}$ which represents shear modulus change due to only void ratio decrease. Then, G_{\max} change due to void ratio change was excluded and decrease in exponent n was computed. Table 8 shows values of n with their corrected value. Decrease of n due to this correction was 4% in average and its highest value was as high as 9%. Thus, Table 8 expresses values of n that controls G_{\max} increase with pressure. Value of n is in average 0.52 for dry samples and 0.48 for saturated samples. Thus, exponent n that controls confining pressure p influence on shear modulus G_{\max} is determined.

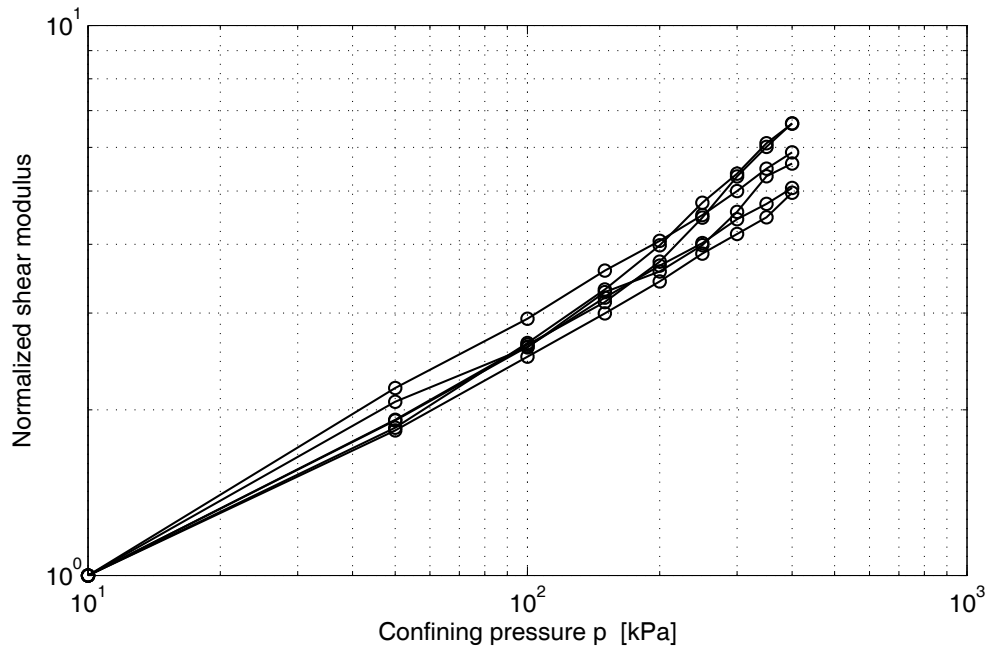


Figure 60. Increase of normalized shear modulus G_{\max} with confining pressure p for all dry natural samples.

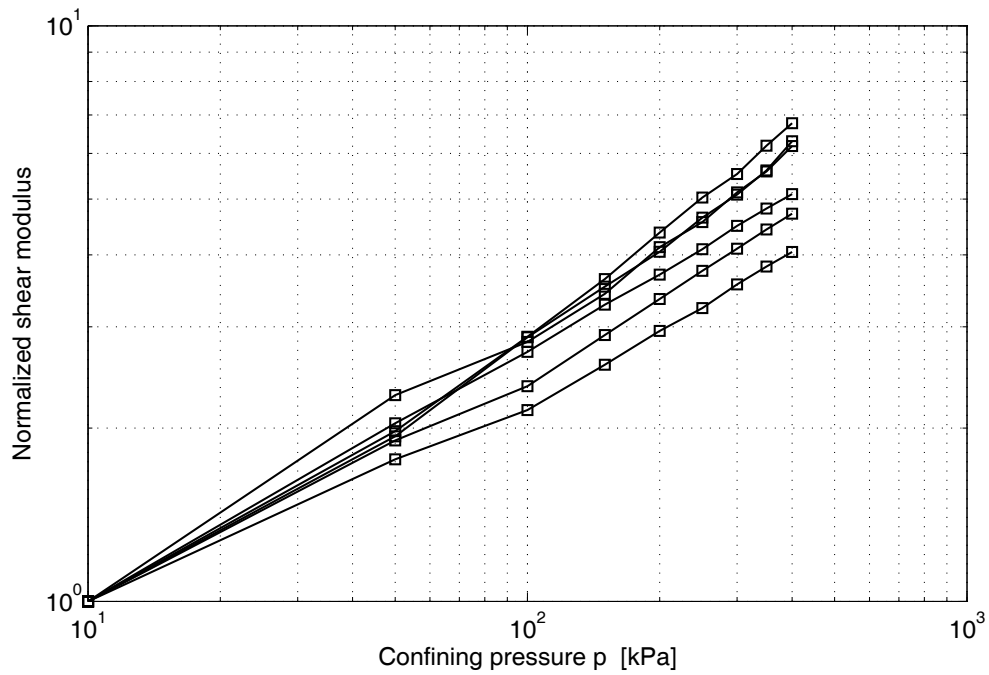


Figure 61. Increase of normalized shear modulus G_{\max} with confining pressure p for all saturated natural samples.

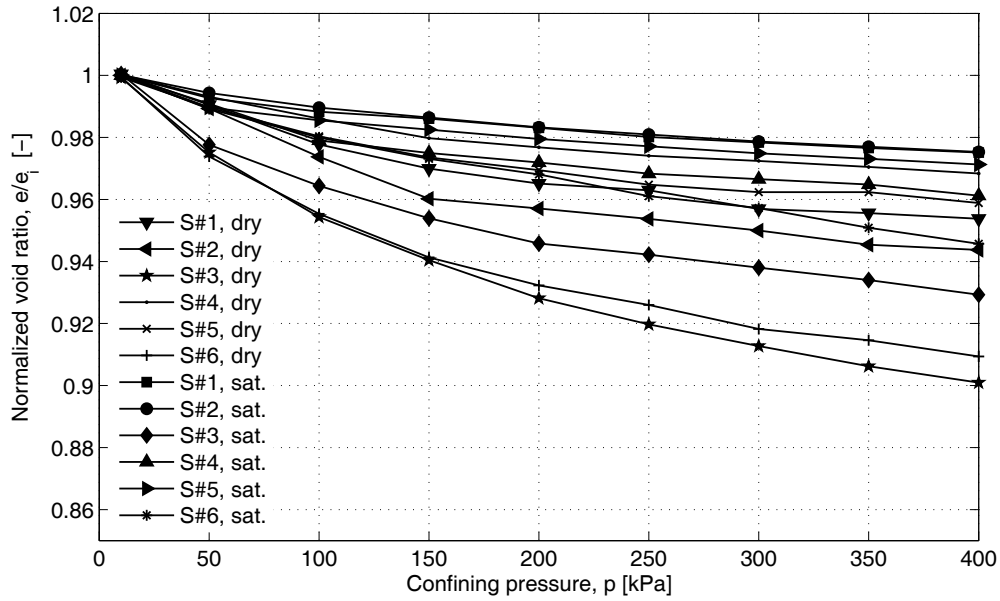


Figure 62. Void ratio change with confining pressure, p , for all tests. Void ratio is normalized to its initial value at 10 kPa for each test.

Table 8. Values of exponent n for all dry and saturated tests.

Material	n value		Corrected n value		d_{50}	C_u
	Dry	Saturated	Dry	Saturated		
S#1	0.462	0.454	0.448	0.449	0.20	1.43
S#2	0.488	0.411	0.468	0.407	0.33	1.81
S#3	0.516	0.519	0.490	0.503	0.33	5.13
S#4	0.658	0.549	0.645	0.538	0.38	1.95
S#5	0.467	0.447	0.453	0.407	0.62	2.46
S#6	0.640	0.592	0.608	0.574	0.63	3.56
Mean value	0.539	0.495	0.519	0.480		

Figure 63 demonstrates the relative change of shear wave velocity with confining pressure. After each pressure step, velocity change is calculated and divided by the average velocity at that step, then plotted versus confining pressure. Each point in Figure 63 represents shear wave velocity gradient at the previous pressure step, for example, the point at 50 kPa for instance, represents velocity gradient due to increasing pressure from 10 to 50 kPa. This figure demonstrates remarkable change in velocity gradient with confining pressure. The velocity gradient decreases from about 30-40% to only 4%. This is 8 to 10 times decrease. Most of this change happens at low confining pressure, especially at the first step (10-50 kPa). On the other hand, the velocity gradient is hardly changing at high confining pressure. The curve tends to be horizontal, i.e. shear wave velocity gradient is constant. In other words, the relationship between shear wave

velocity and confining pressure is linear at such high pressure. All samples have a similar behavior that makes it easier to establish a relationship between G_{\max} and p .

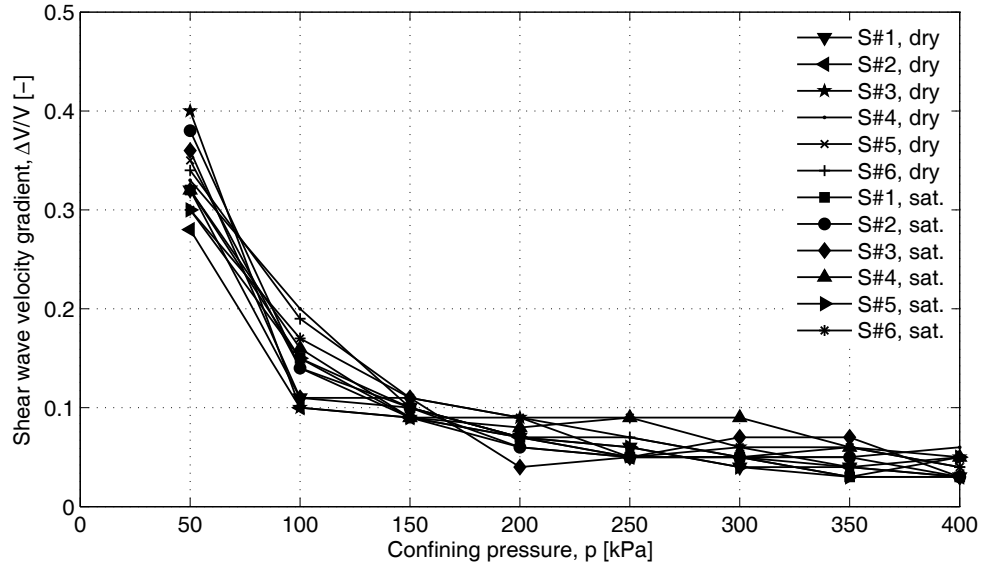


Figure 63. Shear wave velocity gradient with confining pressure p .

6.4 Influence of uniformity coefficient

Parameters of grain size distribution affect the influence of confining pressure on G_{\max} represented as exponent n . In this study, natural material with different uniformity coefficient was used in order to examine this effect. (Menq & Stokoe, 2003) found dependence of exponent n on coefficient of uniformity C_u . Based on an extensive study of 163 test, (Wichtmann & Triantafyllidis, 2009) confirmed this and reported an increase of exponent n with increasing C_u with no influence of d_{50} . In this study, the influence of C_u is detected. Table 8 shows Values of exponent n for all dry and saturated tests with d_{50} and C_u for each material. Materials S#2 and S#3 have the same d_{50} but different C_u . n value is larger for S3 that has higher value of C_u . This observation is also noticed for materials S5 and S6. This suggests dependence of n on C_u . (Wichtmann & Triantafyllidis, 2009) proposed the following formulation to determine n as a function of only C_u :

$$n = a C_u^b$$

with constants $a=0.40$ and $b=0.18$. In order to determine values of a and b in this function, n values were plotted versus C_u for all dry and saturated tests in Figure 64. This figure shows also the best curve fit for the given previous function. For saturated tests, a and b values were 0.42 and 0.16 respectively, which is similar to those proposed by (Wichtmann & Triantafyllidis, 2009). However, for dry tests, b was found to be as small as 0.09 which is significantly smaller than for saturated tests, while a was 0.49. This suggests that exponent n in dry samples is less affected by variation of coefficient of

uniformity C_u than in saturated samples. For a constant coefficient of uniformity C_u , exponent n is higher for a dry sample than for a saturated one. That means, variation of small strain shear modulus G_{\max} with confining pressure p is larger for dry sample than for a saturated one. This difference decreases as C_u increases. Scatter in data is probably due to different d_{50} of samples.

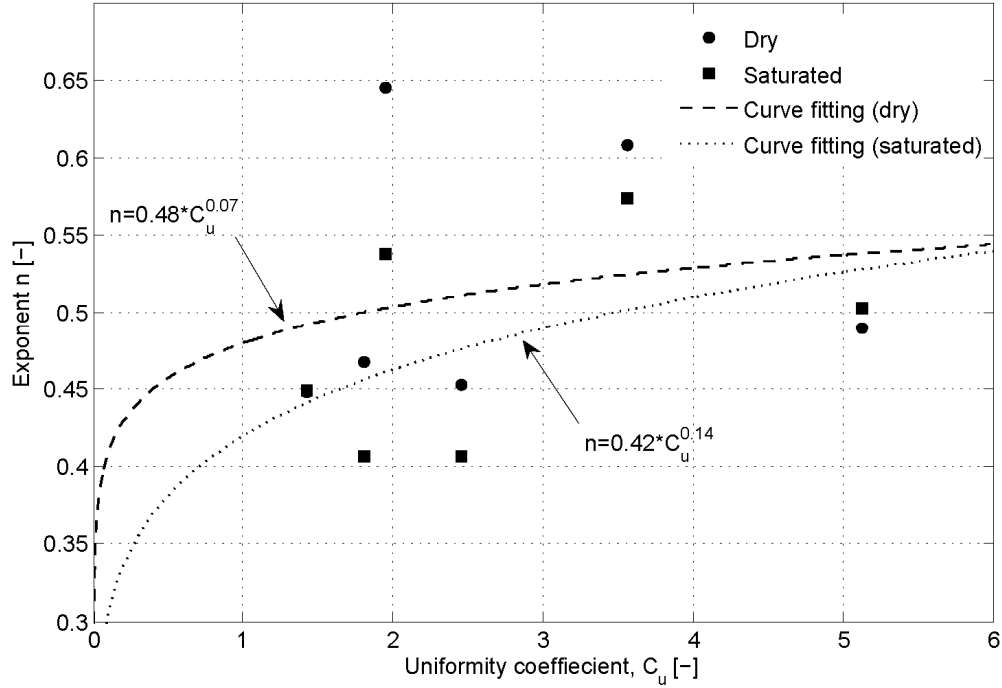


Figure 64. Dependence of n on C_u for all tests.

6.5 Influence of relative density and void ratio

Shear modulus G_{\max} was also represented in the literature as a function of relative density, $D_r = (\rho_d - \rho_{d,\min}) / (\rho_{d,\max} - \rho_{d,\min})$ and confining pressure. (Wichtmann & Triantafyllidis, 2009) proposed the following function to determine G_{\max} :

$$G_{\max} = A_D \frac{1 + D_r / 100}{(a_D - D_r / 100)^2} p_{atm}^{1-n_D} p^{n_D}$$

with constants: $A_D = 177000$, $a_D = 17.3$ and $n_D = 0.48$. In this study, volume change was measured through all tests, thus, sample volume is determined at each pressure. Consequently, void ratio and relative density can also be calculated. This offers a possibility to assign G_{\max} to relative density. The shear modulus in this study is plotted versus relative density for each confining pressure step in Figure 65. Scatter of data is

significant. An attempt to fit the curves to this previous function was done. No stable constants could satisfy this function. Scatter at high confining pressures is larger. Although initial relative densities for all sample were similar, G_{\max} increase with confining pressure varied considerably. This finding is in agreement with (Wichtmann & Triantafyllidis, 2009) and (Iwasaki & Tatsuoka, 1977). For a given confining pressure in Figure 65, G_{\max} should increase with increasing D_r . This behavior is not clear for all confining pressures, especially for high pressure.

Figure 66 demonstrates data in Figure 65 categorized into tests instead of pressures. Data indicate that for different tests, shear modulus G_{\max} shows different behavior for increasing with relative density D_r .

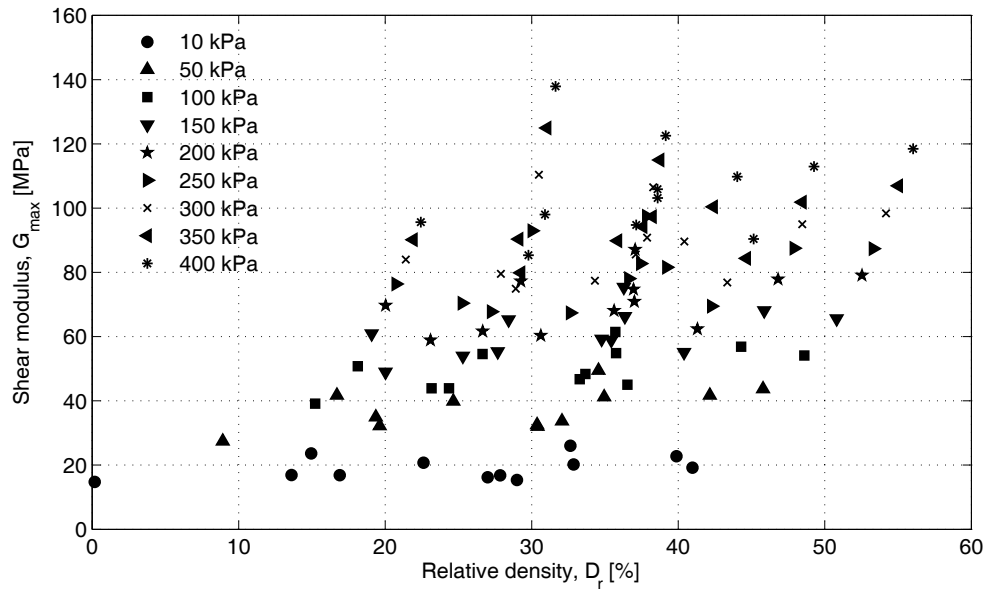


Figure 65. Shear modulus G_{\max} versus relative density D_r for each confining pressure step.

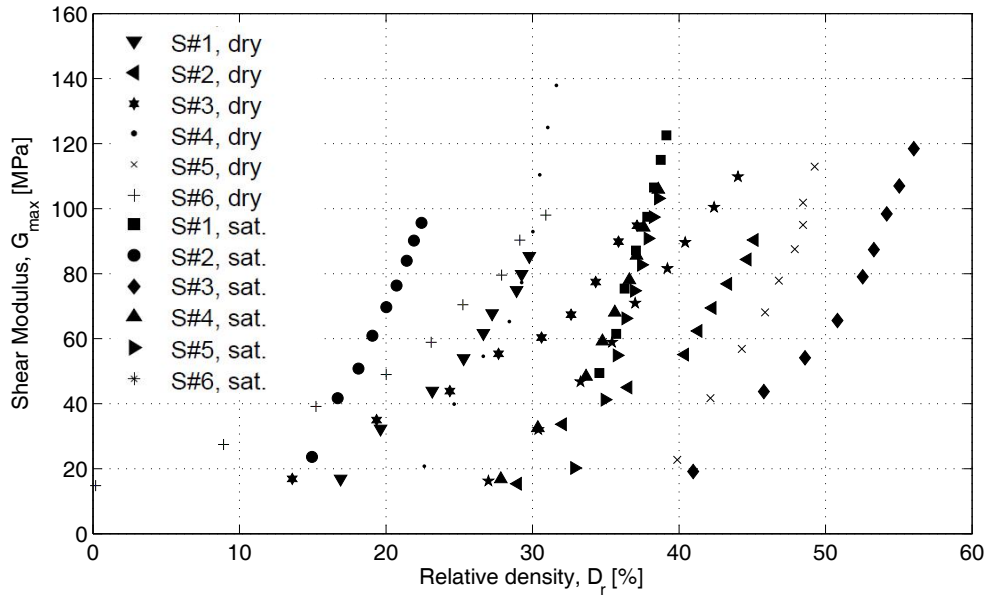


Figure 66. Shear modulus G_{\max} versus relative density D_r for each test (Same data of Figure 65 but categorized into tests instead of pressures).

Most common representation of shear modulus G_{\max} is as a function of void ratio, e and confining pressure, p (Hardin & Richart, 1963; Pestana and Salvati, 1995). In order to isolate the effect of void ratio on G_{\max} , values of G_{\max} were plotted versus e at each confining pressure step in Figure 67. For a specific confining pressure, G_{\max} should increase with decreasing void ratio. This behavior is not clear for all confining pressures, especially for high pressure. Dependence of G_{\max} on e for different pressures should be parallel, which is not the case in Figure 67. Figure 68 shows shear wave velocity gradient for each test with changing void ratio. Since initial void ratios for different tests are not equal, the void ratio is normalized to its initial ratio. After each pressure step, velocity change is calculated and divided by the average velocity at that step, then plotted versus normalized void ratio. Each point in Figure 68 represents shear wave velocity gradient at the previous pressure step. This figure demonstrates remarkable change in velocity gradient with void ratio. The velocity gradient decreases from about 30-40% to only 4% for 3 to 10 % change in void ratio. This shows the great sensitivity of velocity gradient to void ratio that in some cases 3% change in void ratio causes 10 times decrease in velocity gradient. Unfortunately, these samples have no uniform behavior. Scatter of data in Figure 65, Figure 66 and Figure 67 and various behaviors in Figure 68 is due to uniformity coefficient of samples. Grain size distribution may affect signal propagation in soil since each grain size filters specific frequencies that alters output signal and makes detecting shear wave velocity more difficult. Therefore, predicting G_{\max} as a function of confining pressure p and void ratio e or relative density D_r was not possible in this study. In order to establish such relationship, many samples of a given C_u are needed.

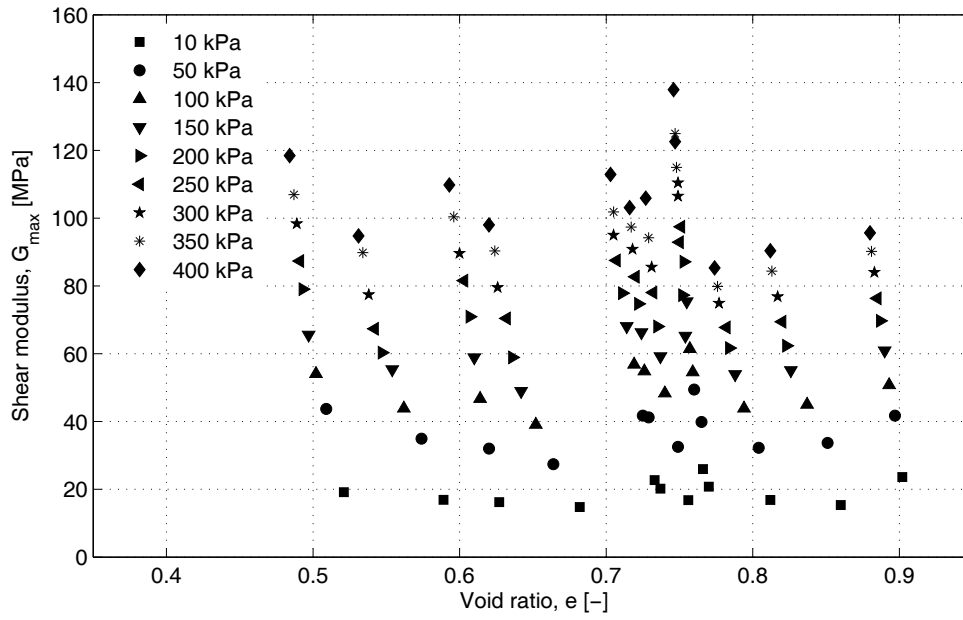


Figure 67. Shear modulus G_{\max} versus void ratio e at each confining pressure for all tests.

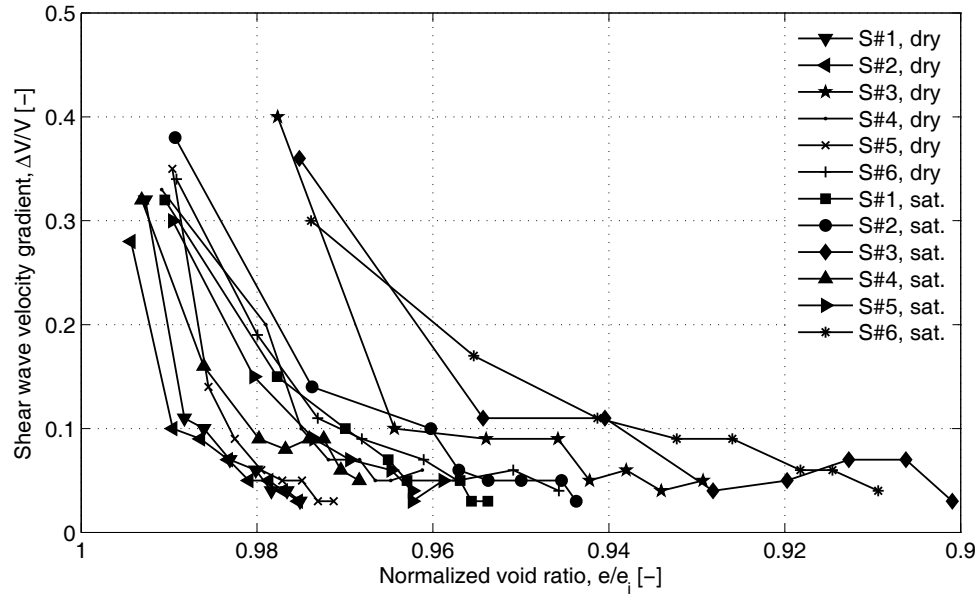


Figure 68. Shear wave velocity gradient with void ratio e .

6.6 Comparing with predicted G_{\max} and resonant column

A series of comparisons between measured G_{\max} by bender elements from this study with predicted G_{\max} and measured G_{\max} by resonant column was carried out. In Figure 69, Figure 70 and Figure 71, shear modulus was calculated for all dry and saturated tests at all pressure steps from 10 kPa to 400 kPa. This produces 108 G_{\max} -value to compare with bender elements values. Figure 69 shows measured G_{\max} by bender elements, BE, and predicted G_{\max} by Hardin's equation:

$$G_{\max} = 900 \frac{(2.17 - e)^2}{1 + e} p^{0.4}$$

where G_{\max} is the shear modulus in kg/cm^2 , p is the confining pressure in kg/cm^2 and e is the void ratio. The figure indicates higher predicted values by Hardin's equation than measured one. The ratio between predicted and measured was found to be 218% in average. Figure 70 shows a comparison between predicted G_{\max} as a function of relative density D_r as described in (section 6.4) with measured G_{\max} by bender elements tests from this study. This figure indicates that predicted G_{\max} -values are 59% higher than measured G_{\max} -values by bender elements. Prediction of G_{\max} as a function of D_r seems to be less scattered than prediction by Hardin's equation in Figure 69. (Wichtmann & Triantafyllidis, 2009) modified Hardin's equation based on resonant column tests to include the influence of uniformity coefficient C_u as:

$$G_{\max} = A \frac{(a - e)^2}{1 + e} p_{atm}^{1-n} p^n$$

where

$$A = 1563 + 3.13 * C_u^{2.98}$$

$$a = 1.94 * e^{-0.066 * C_u}$$

$$n = 0.40 * C_u^{0.18}$$

these constants were calculated for each material in this study, then, the resulting G_{\max} -values predicted by this equations was plotted versus measured G_{\max} from this study in Figure 71. This figure shows that this predicted G_{\max} -values are higher than measured G_{\max} -values. The ratio between both was found to be 58%, which is similar to the predicted G_{\max} as a D_r -function. However, this is significantly lower than prediction by Hardin's equation.

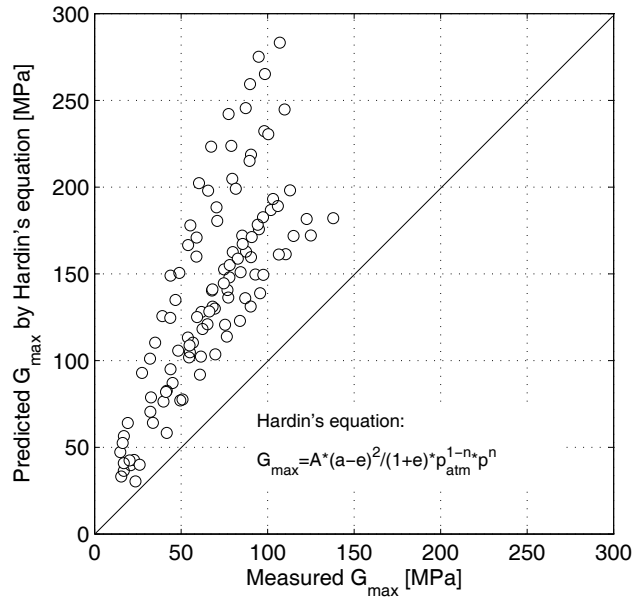


Figure 69. Comparison between measured G_{\max} by BE and predicted G_{\max} with Hardin's equation.

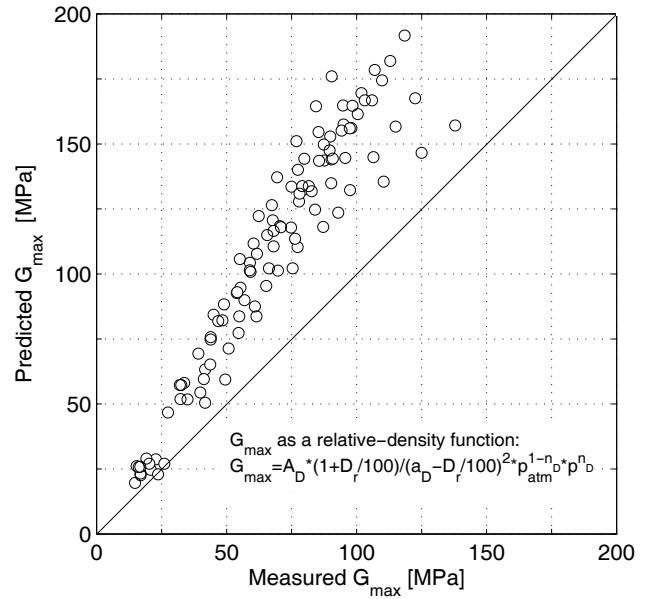


Figure 70. Comparison between measured G_{\max} by BE and predicted G_{\max} with a D_r correlation.

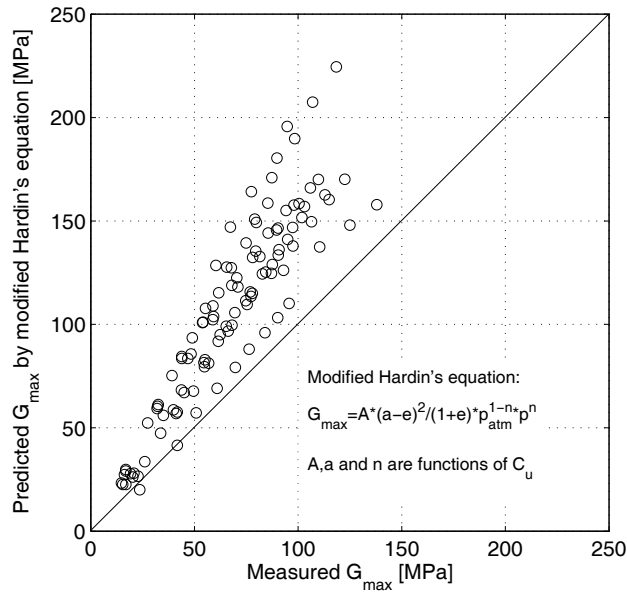


Figure 71. Comparison between measured G_{\max} by BE and predicted G_{\max} with modified Hardin's equation.

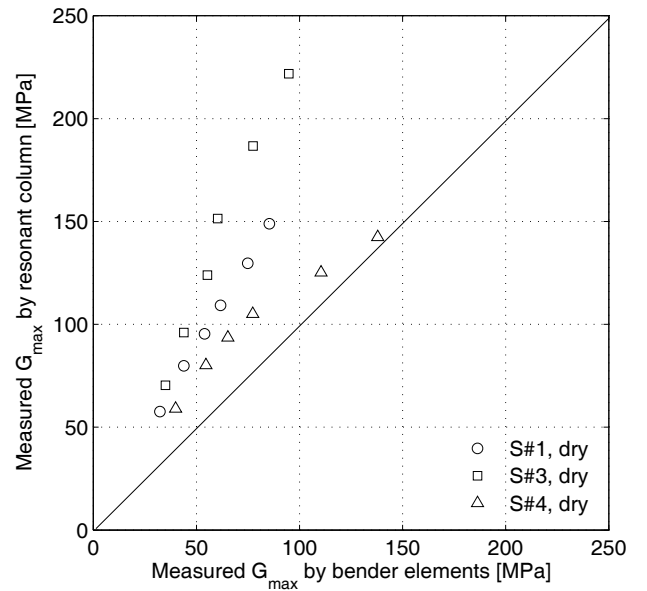


Figure 72. Comparison between measured G_{\max} by BE and measured G_{\max} by RC for materials #1, #3 and #4.

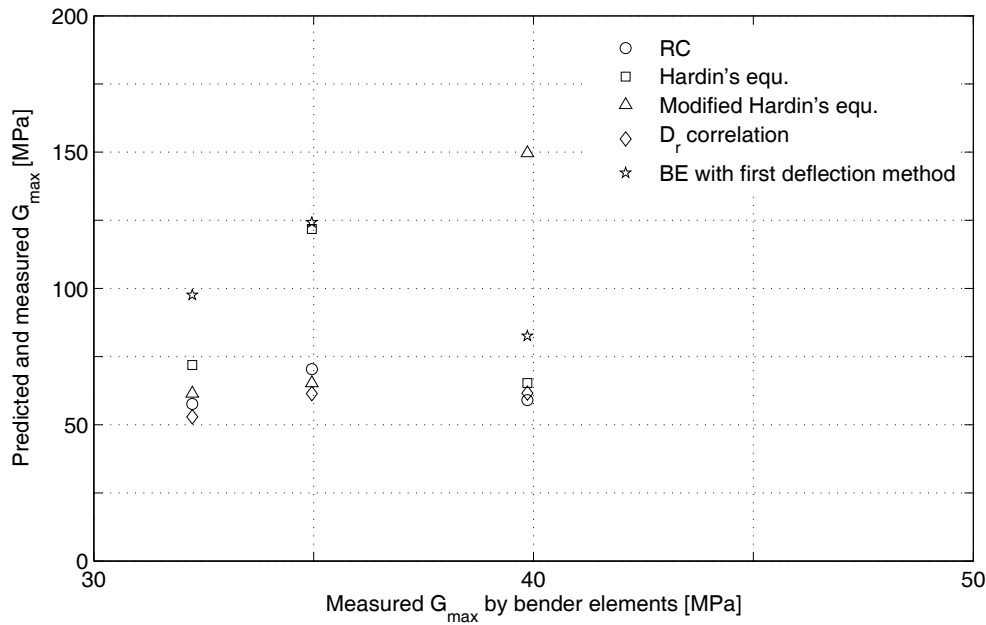


Figure 73. Comparison between measured G_{max} by BE with cc method and predictions, RC data and BE with fd method.

The differences between measured G_{max} from bender elements test and empirical equations from literature is for the reason that these equations are based typically on resonant column tests. The frequency used in resonant column test lies in a range between 30 and 300 Hz, which is different from the frequency range of bender elements test which is 1000-15000 Hz. Furthermore, the fundamental frequency in the resonant column is a function of certain characteristics of the resonant column apparatus. That makes determining shear wave velocity more complicated than in bender elements test and affected by other factors. Besides, in the resonant column technique, driving apparatus and motion monitoring instruments must be fixed to the soil specimen, this changes the boundary conditions since attachments are lumped into a mass that oscillates with the soil specimen. Furthermore, the bender element excites a point-source-wave that is not the case in resonant column. Thus, assumptions in resonant column test are different from bender elements test. This explains differences between measured G_{max} by bender elements test and predicted G_{max} by empirical equations based on resonant column test.

In order to make a direct comparison between bender elements and resonant column tests, samples S#1, S#3 and S#4 were tested by resonant column test (RC) in dry condition. Results were compared with bender elements data for same material and very similar void ratios. Comparison is illustrated in Figure 72. It is shown that RC data are about 79% higher than BE data. Shear wave velocity in bender elements test strongly depends on interpretation method as described in chapter 2. In order to investigate that, a comparison was made at 50 kPa between measured G_{max} by bender elements from this study interpreted by cross-correlation, cc, from one side, and corresponding predicted G_{max} from equations (Hardin's, modified Hardin's and D_r correlation), beside resonant

column result for materials S#1, S#3 and S#4 and bender elements results from this study interpreted by first deflection method from the other side. One can notice that measured G_{\max} by resonant column test is very similar to those from D_r -correlation.

First deflection method that has been very common to compare bender elements data with resonant column data in literature does not show good agreement with any other set of data. It tends to overestimate predictions, RC data and BE with cross-correlation method. The reason of the good agreement in literature of RC and BE results is that, first deflection method is typically used to detect shear wave velocity in BE test, which is very subjective and strongly dependent on input frequency used as described in details in chapter 5. In Figure 73, interpretation by cross-correlation and first deflection used the same frequency. This shows that resonant column test or empirical equations based on it do not compare well with bender elements test, due to differences in test procedures, assumptions and interpretation. As shown in Figure 73, cross-correlation underestimates resonant column results while first deflection overestimates them. This demonstrates the strong influence of signal interpretation method on results and shows the need of a robust and stable method to interpret data in bender elements tests. Moreover, although resonant column test has been known for a long time, it cannot be simply a reference for bender elements result, due to the reasons discussed previously. Rather, a deeper understanding of wave propagation in soil will help to evaluate both tests. Such understanding includes wave propagation analyzing and numerical simulation. This might help realizing the influence of frequency difference and type of wave between bender elements and resonant column tests.

6.7 Summary

A series of 12 samples at confining pressure range between 10 kPa and 400 kPa were tested. Measurements of shear waves were taken at each step, and then analyzed by the cross-correlation method. A relationship between G_{\max} and p was established. The exponent n that controls this relationship was found to be in average 0.52 for dry samples and 0.48 for saturated ones. That means, shear stiffness G_{\max} tends to increase quicker with confining pressure for dry samples than for saturated ones. Exponent n was found to be a function of uniformity coefficient C_u and constants for this function is proposed. Although exponent n is higher for a dry sample than for a saturated one for a given C_u , it is less affected by variation in C_u values. An attempt was made to predict G_{\max} as a function of void ratio e or relative density D_r . This was not possible in this study due to lack of samples for a given C_u . A series of comparisons between measured G_{\max} by bender elements from this study with predicted G_{\max} and measured G_{\max} by resonant column was carried out. It was found that predictions of G_{\max} by modified Hardin's equation or a function of relative density overestimates BE-values by a ratio of 58%. While Hardin's function extremely overestimates BE-value by a ratio of 218%. Resonant column results showed no agreement with bender elements results even when first deflection method is applied. Reasons for this disagreement were discussed, such as differences in frequency, procedures, assumptions and interpretation.

Chapter 7

Study of Artificial Material

7.1 Introduction

In order to specify and isolate the influence of confining pressure on shear modulus G_{\max} , an artificial material was used to study this effect with bender elements. This material is uniform glass beads with mean diameter 8 mm and 3.5 mm and specific gravity 2.5, which is very similar to sand. Figure 74 shows the glass material. The advantage of using this material is that no volume change is allowed to occur during the test due to pressure increase, because the beads are uniform, thus, no redistribution can take place while pressure increases. In this manner, shear stiffness G_{\max} increases during the test only due to confining pressure p increase. Therefore, influence of p on G_{\max} represented as exponent n is isolated. Subsequently, the influence of saturation on G_{\max} and n can be examined.

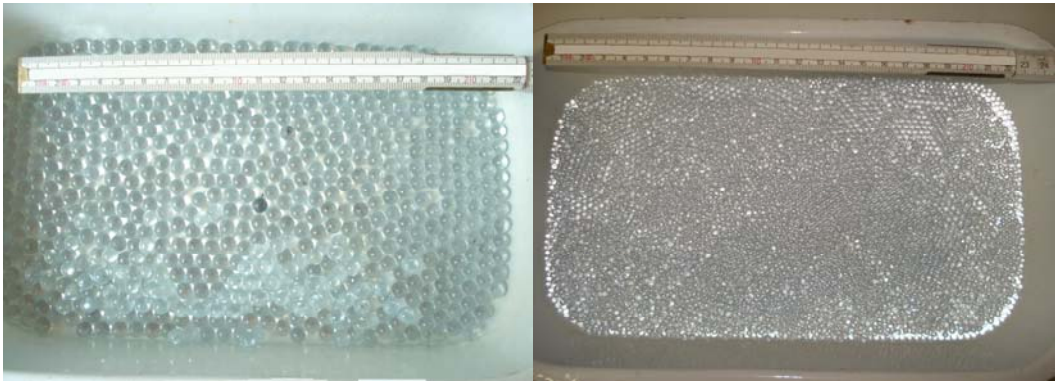


Figure 74. Artificial material of uniform glass beads. Left 8 mm; and right 3.5 mm.

7.2 Experimental data

Figure 75 shows the sample of glass beads prepared in the triaxial cell. The membrane is not smooth as it is typically for sand.

The dry and saturated samples were prepared in the same method of the natural material. Shear wave velocity was measured for each confining pressure step. As the pressure increases, the penetration of the membrane becomes greater, given that the particle size is large. This causes tension stress at some local points in the membrane, which it may not stand. For the test of large particles 8 mm, this stage was reached at 300 kPa. At this moment, the membrane ruptured and cell water ran into the sample, consequently, no confining pressure was holding the sample any more, and the test was forced to stop. Therefore, only for this diameter, shear wave velocity was examined until confining pressure 300 kPa instead of 400 kPa for 3.5 mm material, which did not have such problem since their particle size is smaller.



Figure 75. Sample of glass beads in a triaxial cell.

Table 9 through Table 12 show the experimental data for the glass beads of 8 mm and 3.5 mm in dry and saturated conditions. For each confining pressure step, travel time was determined by the cross-correlation method, then, shear modulus was calculated, assuming that density is constant during the test. In the saturated condition, shear modulus was calculated from shear wave velocity considering mass density not total density as discussed by (Youn, et al., 2008) based on Biot's theory.

A power law was proposed by (Hardin & Richart, 1963) to determine the relationship between small-strain modulus G_{\max} and effective mean stress p' :

$$G_{\max} \propto (p')^n$$

(Hardin & Richart, 1963) themselves used the value $n = 0.5$ for cohesive and non-cohesive soils. Their value for non-cohesive soils is widely confirmed, since all recent studies use the exponent $n = 0.40-0.55$ (Hoque & Tatsuoka, 2004; Kallioglou & Papadopoulou, 2003; Kuwano & Jardine, 2002). The effect of p on G_{\max} can be expressed as a normalized confining pressure to the power n as:

$$G_{\max} = G_b \left(\frac{p}{p_{\text{atm}}} \right)^n$$

where p_{atm} is the atmospheric pressure and G_b is the value of G_{\max} at confining pressure of 1 atm. In these four tests, variation of shear modulus G_{\max} with confining pressure was examined.

Table 9. Experimental data for dry sample of glass beads of 8 mm.

Confining Pressure [kPa]	Travel time [ms]	Velocity [m/s]	G_{\max} [MPa]
10	1.05	176	45.87
50	0.77	240	85.30
100	0.69	269	107.78
150	0.63	295	129.46
200	0.60	308	140.48
250	0.58	321	152.96
300	0.56	333	164.18

Table 10. Experimental data for saturated sample of glass beads of 8 mm.

Confining Pressure [kPa]	Travel time [ms]	Velocity [m/s]	G_{\max} [MPa]
10	1.24	152	34.16
50	0.84	224	74.44
100	0.72	263	102.74
150	0.66	285	120.58
200	0.63	301	134.46
250	0.61	311	143.50
300	0.58	324	156.14

Table 11. Experimental data for dry sample of glass beads of 3.5 mm.

Confining Pressure [kPa]	Travel time [ms]	Velocity [m/s]	G_{\max} [MPa]
10	1.21	150.50	33.64
50	0.91	200.12	59.47
100	0.78	233.47	80.95
150	0.71	256.49	97.70
200	0.68	267.81	106.51
250	0.63	289.06	124.08
300	0.58	313.98	146.40
350	0.57	319.49	151.58
400	0.53	343.60	175.32

Table 12. Experimental data for saturated sample of glass beads of 3.5 mm.

Confining Pressure [kPa]	Travel time [ms]	Velocity [m/s]	G_{\max} [MPa]
10	1.46	124.73	23.10
50	0.94	193.73	55.74
100	0.79	230.52	78.91
150	0.73	251.19	93.70
200	0.69	265.85	104.96
250	0.65	280.17	116.56
300	0.62	293.73	128.12
350	0.60	303.52	136.80
400	0.57	319.49	151.58

Figure 76 shows shear modulus variation with confining pressure in a double-logarithmic scale. As expected, shear modulus increases with confining pressure. For the dry specimen of 8 mm, the value of n was found to be 0.37, while the curve of saturated sample is better fitted with exponent $n=0.42$. One can notice that for pressure values larger than 100 kPa both curves of dry and saturated condition have similar n value, i.e. variation of shear modulus with confining pressure is almost the same for both cases. The relationship of G_{\max} with confining pressure can be represented as in Table 13.

Table 13. G_{\max} as a function of p for two particle sizes in dry and saturated condition.		
Particle size [mm]	Dry	Saturated
8	$G_{\max} = 109 * (\frac{P}{P_{atm}})^{0.37}$	$G_{\max} = 100 * (\frac{P}{P_{atm}})^{0.42}$
3.5	$G_{\max} = 81 * (\frac{P}{P_{atm}})^{0.52}$	$G_{\max} = 76 * (\frac{P}{P_{atm}})^{0.48}$

Firstly, if one compares dry with saturated condition for each material in Table 9 through Table 12, it is noticeable that G_{\max} -values in dry condition is larger than for saturated one. The raise is 11% for 8-mm-material and 12% for 3.5-mm-material. This observation is very difficult to detect in the case of soil since samples must have exactly the same void ratio. This difference can be ascribed to dispersion and attenuation of the elastic wave propagation through fluid-saturated material. Water viscosity may affect relative movement between particles and thus, resist wave propagation.

Secondly, if one compares 8 mm with 3.5 mm for dry or for saturated condition, it is obvious that G_{\max} -values for the 8-mm-material is considerably higher than for the 3.5-mm-material. Only a slight increase of G_{\max} with increase d_{50} was reported by (Iwasaki & Tatsuoaka, 1977). In this study, the raise is as high as 27% and 31% for dry and saturated condition respectively. In a porous medium, only waves with wavelength greater than particle diameter can propagate. Other waves with wavelength smaller than particle diameter cannot cause relative movement between medium particles and thus, can not propagate. That means that medium filters waves with such high frequencies that their wavelength is smaller than particles diameter. In our case, the 8-mm-particles filter lower frequencies than the 3.5-mm-particles. Therefore, the frequency content is different for different particle sizes. This may alter output signal and wave velocity.

Figure 77 demonstrates the relative change of shear wave velocity with confining pressure. After each pressure step, velocity change is calculated and divided by the average velocity at that step, then plotted versus confining pressure. Each point in Figure 77 represents shear wave velocity gradient at the previous pressure step, for example, the point at 50 kPa for instance, represents velocity gradient due to increasing pressure from 10 to 50 kPa. This figure demonstrates remarkable change in velocity gradient with confining pressure. The velocity gradient decreases from about 40% to only 5% for the 8-mm- sample and from about 30% to 4% for the 3.5-mm-sample. This is 8 to 10 times

decrease. Most of this change happens at low confining pressure, especially at the first step (10-50 kPa). On the other hand, the velocity gradient is hardly changing at high confining pressure. The curve tends to be horizontal, i.e. shear wave velocity gradient is constant. In other words, the relationship between shear wave velocity and confining pressure is linear at such high pressure. For natural material, similar behavior is detected.

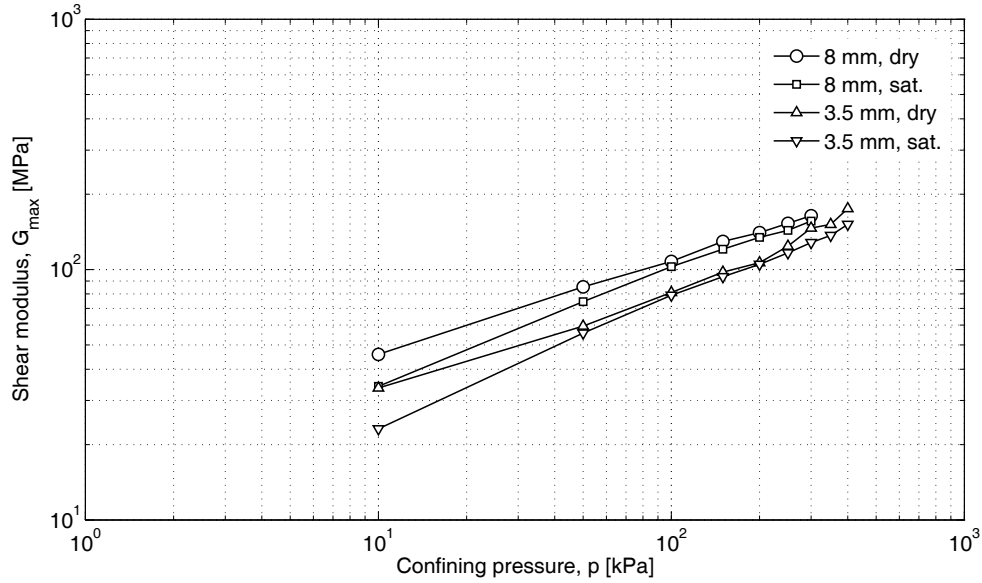


Figure 76. Shear small-strain modulus G_{\max} variation with confining pressure in a logarithmic scale.

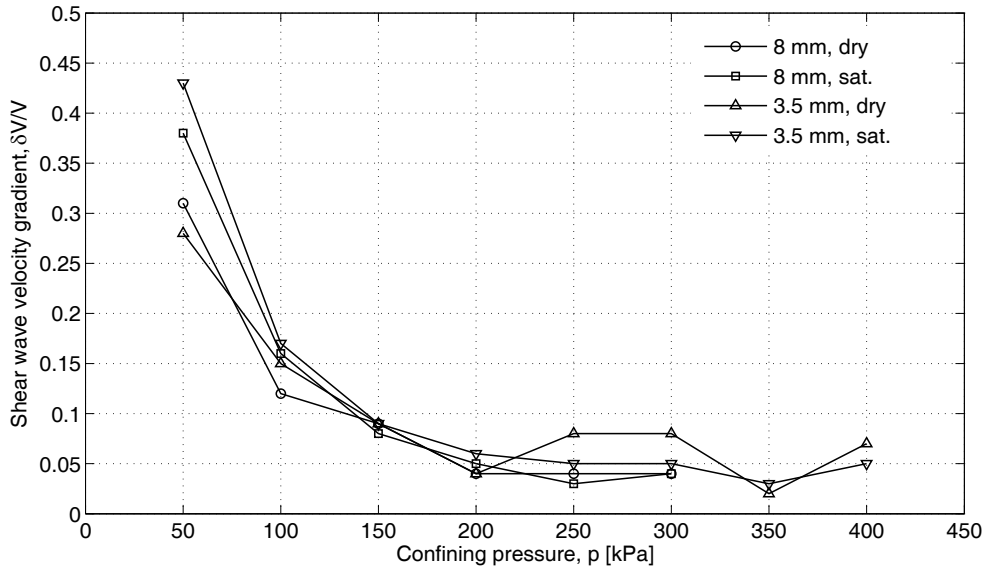


Figure 77. Shear wave velocity gradient with confining pressure. Each point represents velocity gradient for the previous pressure step.

7.3 Summary

Two samples of uniform glass beads were studied in the dry and saturated condition. The influence of confining pressure on shear modulus G_{\max} was specified and isolated. G_{\max} variation with confining pressure was examined for both cases. A relationship of G_{\max} with confining pressure and a value for the exponent n was proposed for both cases, dry and saturated. An interesting decrease of about 11% in shear modulus occurred when saturating the sample. This observation was confirmed by both samples. An apparent increase in G_{\max} took place when using larger particles. For an increase from 3.5 mm to 8 mm in particle diameter, G_{\max} increased about 29%. Similar increase happened for both dry and saturated conditions.

The relative change of shear wave velocity with confining pressure was demonstrated. The velocity gradient decreases 8 to 10 times in the pressure range of the test. Most of this change happens at low confining pressure. While it is hardly changing at high confining pressure showing a linear behavior between shear wave velocity and confining pressure.

Chapter 8

Conclusions and Recommendations

The initial shear modulus G_{\max} of soil is a critical parameter for a variety of geotechnical design applications. The critical role of soil stiffness at small-strains in the design and analysis of geotechnical infrastructure is now widely accepted. Although there are a variety of in-situ tests to determine G_{\max} these tests do not show the effects of other conditions than the current in-situ condition, and they require specialized costly equipment and experienced operator, besides, some of these tests are limited or with error sources. Bender elements give a good alternative test to measure G_{\max} . Unfortunately, there is no standard for this test. Many issues are still ambiguous. Different waveforms were analyzed in this study with a wide range of frequencies and their influence on shear wave velocity. Most common interpretation methods were analyzed. Subsequently, a waveform of sinus with frequency range of 7 to 15 kHz was found to give finest output signal. The cross-correlation method was proven to be the most stable method to analyze data.

A series of 12 samples at confining pressure range between 10 kPa and 400 kPa were tested. A relationship between G_{\max} and confining pressure p was established represented as exponent n . Dependence of n on saturation condition and uniformity coefficient is proven and evaluated. Results from bender elements tests with different interpretation methods were compared with prediction formulations and resonant column tests. Bender elements results were not in agreement with prediction formulations and resonant column tests. Reasons for this difference, such as differences in frequency, procedures, assumptions and interpretation, were discussed in chapter 6.

Another series of 4 tests were carried out on artificial material. As a result, the influence of confining pressure p on shear modulus G_{\max} was specified and isolated. The advantage of using this material is that no volume change is allowed to occur during the test due to pressure increase since glass beads are uniform. By saturation, a decrease of about 11% in shear modulus occurred. This observation was confirmed by both samples. The particles diameter has a clear effect on G_{\max} . An apparent increase in G_{\max} took place when using larger particles. For an increase from 3.5 mm to 8 mm in particle diameter, G_{\max} increased about 29%. Similar increase happened for both dry and saturated conditions.

Generally, in this study, right properties for input signal were chosen and interpretation methods were evaluated in order to make bender elements results reliable. This was applied in testing 16 sample of 6 natural material and 2 artificial in dry and saturated conditions. Thousands of time histories were acquired and analyzed. Subsequently, influences of confining pressure, uniformity coefficient and particle size were studied. However, many points are still ambiguous. Bender elements test has not been standardized and many effects are not clear. More studies should be done on wave propagation in porous media to better analyze interpretation methods of bender elements tests. A numerical simulation may help understanding how different frequencies propagate in a different way in a particular medium. As a result of that, optimal waveform and input frequency can be determined. Regarding influences on G_{\max} , tests on artificial material such as glass beads used in this study can be continued to investigate grain size, confining pressure, anisotropy, partial saturation and full saturation effect on G_{\max} .

References

- [1] Arulnathan, R., Boulanger R.W. and Riemer, M.F. Analysis of Bender Element Tests. ASTM Geotechnical Testing Journal, Vol. 21, No. 2, pp. 120-131, 1998.
- [2] Asslan, M. Factors Influencing Small-Strain Stiffness of soils and its Determination. Term paper. Bauhaus university, 2008.
- [3] Atkinson, J.H. and Salfors, G. Experimental determination of soil properties. Proc. 10th Eur. Conf. Soil Mech., Florence 3, 915-956, 1991.
- [4] Brignoli, E.G.M., Gotti, M. and Stokoe, K.H. Measurement of shear waves in laboratory specimens by means of piezoelectric transducers. ASTM Geotechnical Testing Journal, Vol. 19, No. 4, pp. 384–397, 1996.
- [5] Burland, J.B. Small is beautiful - The stiffness of soils at small strains. Canadian Geotechnical Journal, 9th Laurits Bjerrum memorial lecture, 1989.
- [6] Chen, Y., Zhou, A. Technique standardization of bender elements and international parallel test. Soil and rock behavior and modeling: proceeding of sessions of GeoShanghai. ASCE Conf. Proc. 194, 11, pp. 90-97, 2006.
- [7] Clayton, C. R. I. and Heymann, G. Stiffness of geomaterials at very small strains. Géotechnique 51, No. 3, pp. 245–255, 2001.
- [8] Dano, C., Hareb, H., and Hicher, P. Characterization of Loire river sand in the small strain Domain using new bender-extender elements. 16th ASCE Engineering Mechanics Conference, University of Washington, Seattle, 2003.
- [9] Dyvik, R. and Madshus, C. Laboratory measurements of G_{\max} using bender elements. Proceeding ASCE Annual Convention: Advances in the art of testing soils under cyclic conditions, pp. 186–196, 1985.
- [10] EPRI. Guidelines for determination design basis ground motion. Electric Power Research Institute, Palo Alto, California, Vol. 1, pp. 8-1 through 8-69, 1993.
- [11] Fioravante, V. & capoferri, R. on the use of multi-directional piezoelectric transducers in triaxial testing. ASTM Geotechnical Testing Journal, Vol. 24, No. 3, pp. 243-255, 2001.

- [12] Hardin, B.O. and Richart, F.E. Elastic wave velocities in granular soils. *Journal of Soil Mechanics and Foundations Division*, 89(SM1), pp. 33-65, 1963.
- [13] Head, K.H. *Manual of Soil Laboratory Testing*. Vol. 3. Effective stress tests. London, 1986.
- [14] Hoque, E. and Tatsuoka, F. Effects of stress ratio on small-strain stiffness during triaxial shearing. *Géotechnique* 54, No. 7, pp. 429-439, 2004.
- [15] Hynes-Griffin, M. E. Pore pressure generation characteristics of gravel under undrained cyclic loading. PhD thesis, University of California, Berkeley, 1988.
- [16] International Society of Soil Mechanics and Geotechnical Engineering (ISSMGE). International parallel test on the measurement of G_{\max} using bender elements organized by TC-29, 2007.
- [17] Iwasaki, T. and Tatsuoka, F. Effects on grain size and grading on dynamics shear moduli of sands. *Soils and Foundations*, Vol. 17, No. 3, pp. 19-35, 1977.
- [18] Jovičić, V., Coop, M.R. and Simić, M. Objective criteria determining G_{\max} from bender elements tests. *Géotechnique* 46, No. 2, pp. 357-362, 1996.
- [19] Kalliouglou, T.T. and Papadopoulou, A. and Pitilakis, K. Shear modulus and damping of natural sands. *Third International Symposium on Deformation Characteristics of Geomaterials*, pp. 401-408, 2003.
- [20] Karl, L. Dynamic Soil Properties out of SCPT and Bender Element Tests with Emphasis on Material Damping. PhD thesis, Ghent University, 2005.
- [21] Krumb, A. and Wuttke, F. SeismicCone und MagCone – neue Entwicklungen in der Drucksondiertechnik und ihre Anwendungsgebiete. 5. Hans Lorenz Symposium, Baugrunddynamik und Spezialtiefbau. Technische Universität Berlin, 2009.
- [22] Kurup, P.U. Innovations in cone penetration testing. *Proc. of Sessions of GeoShanghai 2006*. ASCE Conf. Proc. 193, 6, pp. 48-55, 2006.
- [23] Kramer, S. L. *Geotechnical Earthquake Engineering*. Prentice-Hall, 1996.
- [24] Kuwano, R. and Jardine, R.J. On the application of cross-anisotropy elasticity to granular materials at very small strains. *Géotechnique* 52, No. 10, pp. 727-749, 2002.
- [25] Lai, C.G., Rix, G.J., Foti, S. and Roma, V. Simultaneous measurement and inversion of surface wave dispersion and attenuation curves. *Soil Dynamics and Earthquake Engineering*, Vol. 22, No. 9-12, pp. 923-930, 2002.

- [26] Lee, J.-S. and Santamarina, J. C. Bender Elements: Performance and Signal Interpretation. *ASCE Journal of Geotechnical and Geoenvironmental Engineering*, Vol. 131, No. 9, pp. 1063-1070, 2005.
- [27] Leong, E., Yeo, S., Raharadjo, H. Measuring shear wave velocity using bender elements. *ASTM Geotechnical Testing Journal*, Vol. 28, No. 5, pp. 488-498, 2005.
- [28] Lings, M. & Greening, P. A novel bender/extender element for soil testing. *Géotechnique* 51, No. 8, pp. 713-717, 2001.
- [29] Mair, R.J. Developments in geotechnical engineering research: application to tunnels and deep excavations. *Proceedings of institution of Civil Engineering, Civil Engineering*, pp. 27-41, 1993. Unwin Memorial Lecture, 1992.
- [30] Marosi, K.T. and Hiltunen, D.R. Characterization of spectral analysis of surface waves shear wave velocity measurement uncertainty. *ASCE Journal of Geotechnical Engineering*, 130 (10), pp. 1034-1041, 2004.
- [31] Menq, F.-Y. and Stokoe, K.H. Linear dynamic properties of sandy and gravelly soils from large-scale resonant column. *Third International Symposium on Deformation Characteristics of Geomaterials*, pp. 63-71, 2003.
- [32] Mohsin, A., Airey, D. Automating G_{\max} measurement in triaxial tests. *Third International Symposium on Deformation Characteristics of Geomaterials*, pp. 73-80, 2003.
- [33] Narazian, S. and Stokoe, K.H. Use of spectral analysis of surface waves for determination of moduli and thickness of pavement systems. *Transportation Research Record 954*, Transportation Research board, Washington, D.C., 1983.
- [34] Pennington, D., Nash, D., and Lings, M. Horizontal mounted bender elements for measuring anisotropic shear moduli in triaxial clay specimens. *ASTM Geotechnical Testing Journal*, Vol. 24, No. 2, pp. 133-144, 2001.
- [35] Pestana, J. and Salvati, L. Small-strain behavior of granular soils. I: Model for semented and uncemented sands and gravels. *ASCE Journal of Geotechnical and Geoenvironmental Engineering*, Vol. 132, No. 8, pp. 1071-1081, 2006.
- [36] Pihl, J., Hammarstroem, M., Ivansson, S. and Moren, P. Crosshole Investigations - Results from Seismic Borehole Tomography. *Stripa Project Internal Report*, 1986.

- [37] Robertson, P.K., Campanella, R.G., Gillespie, D. and Rice, A. Seismic CPT to measure in situ shear wave velocity. ASCE Journal of the Geotechnical Division, Vol. 112, No. 8, pp. 791-803, 1986.
- [38] Sanchez-Salinero, I., Roesset, J.M., Stokoe, K.H. Analytical studies of body wave propagation and attenuation. Report GR 86-15. University of Texas at Austin, 1986.
- [39] Santamarina J. C. and Fratta, D. Discrete Signals and Inverse Problems, An Introduction for Engineers and Scientists. John Wiley & Sons, Ltd., 2005
- [40] Santos, J.A. and Gomes Correia, A. Reference threshold shear strain of soil. Its application to obtain an unique strain-dependent shear modulus curve for soil. Proc. 15th International Conference on Soil Mechanics and Geotechnical Engineering, Istanbul, Turkey, Vol. 1, pp. 267-270, 2001.
- [41] Schultheiss, P.J. Simultaneous measurement of P & S wave velocities during conventional laboratory testing procedures. Marine Geotechnology, Vol. 4, No. 4, pp. 343-367, 1981.
- [42] Seed, H.B. and Idriss, I.M. Soil moduli and damping factors for dynamic response analysis. Report 70-10, EERC, Berkeley, CA, 1970.
- [43] Sheriff, R.E. and Geldart, L.P. Exploration Seismology. Second edition, Cambridge university press, 1995.
- [44] Shibuya, S., Tatsuoka, F., Teachavorasinskun, S., Kong X.J., Abe, F., Kim Y.S. and Park, C.S. Elastic deformation properties of Geomaterials. Soils and Foundations, Vol.32, No.3, pp. 26-46, 1992.
- [45] Shirley, D.J. and Hampton, L.D. Shear-wave measurements in laboratory sediments. Journal of Acoustical Society of America, 63(2), pp. 607-613, 1978.
- [46] Stokoe, K.H., Wright, S.G., Bay, J.A. and Roesset, J.M. Characterization of geotechnical sites by SASW method. Geophysical Characterization of Sites, eds. Woods, R.D., Balkema, Netherlands, pp. 15-25, 1994.
- [47] Tatsuoka, F. Impacts on geotechnical engineering of several recent findings from laboratory stress-strain tests on geomaterials. Department of Civil Engineering Mechanics, Columbia University, 2000.
- [48] Tatsuoka, F., Lo Presti, D.C.F. and Kohata, Y. Deformation characteristics of soils and soft rocks under monotonic and cyclic loads and their relationships. SOA Report, Proc. Of the third international conference on recent advanced in Geotechnical earthquake engineering and soil dynamics, St Louis (Prakash eds.) Vol.2 pp. 851-879, 1995.

- [49] Tatsuoka, F. and Shibuya, S. Deformation characteristics of soil and rocks from field and laboratory tests. Keynote Lecture (Session No.1). Proc. of the 9th Asian Regional Conference on Soil Mechanics and Foundation Engineering, Bangkok, Vol. 2, pp. 101–170, 1991.
- [50] Viggiani, G. and Atkinson, J.H. Interpretation of bender element tests. *Géotechnique* 45, No. 1, pp. 149-154, 1995a.
- [51] Vucetic, M. Cyclic threshold shear strains in soils. *ASCE Journal of Geotechnical Engineering*, 120(12), pp. 2208-2228, 1994.
- [52] Yamashita, S., Kohata, Y., Kawaguchi, T. and Shibuya, S. International round-robin test organized by TC-29. Advanced laboratory stress-strain testing of Geomaterials, Tatsuoka, Shibuya and Kuwano (eds.). Balkema, 2001.
- [53] Wichtmann, T. and Triantafyllidis, Th. On the influence of the grain size distribution curve of quartz sand on small strain shear modulus G_{\max} . *ASCE Journal of Geotechnical and Geoenvironmental Engineering*, Vol. 135, No. 10, pp. 1-15, 2009.
- [54] Woods, R.D. Field and laboratory determination of soil properties at low and high strains. Proc. of second international conference on recent advances in geotechnical earthquake engineering and soil dynamics. St. Louis, MO, Vol. II, pp. 1727-1741, 1991.
- [55] Wuttke, F. In situ soil characterization using surface waves. Presentation at the Bulgarian Academy of Science. Bauhaus-University Weimar, 2005.
- [56] Youn, J.-U., Choo, Y.-W. and Kim, D.-S. Measurement of small-strain shear modulus G_{\max} of dry and saturated sands by bender element, resonant column, and torsional shear tests. *Canadian Geotechnical Journal*, Vol. 45, pp. 1426–1438, 2008.

Erklärung

Ich erkläre, dass ich die vorliegende Arbeit selbständig und nur unter Verwendung der angegebenen Quellen und Hilfsmittel angefertigt habe.

Weimar, 19. 10. 2009